Fourier optics for wavefront engineering and wavelength control of lasers

Fourier optics for wavefront engineering and wavelength control of lasers

A dissertation presented

by

Romain Blanchard

to

The School of Engineering and Applied Sciences

in partial fulfillment of the requirements

for the degree of

Doctor of Philosophy

in the subject of

Applied Physics

Harvard University
Cambridge, Massachusetts

October 2013

Professor Federico Capasso Romain Blanchard

Fourier optics for wavefront engineering and wavelength control of lasers

Abstract

Since their initial demonstration in 1994, quantum cascade lasers (QCLs) have become prominent sources of mid-infrared radiation. Over the years, a large scientific and engineering effort has led to a dramatic improvement in their efficiency and power output, with continuous wave operation at room temperature and Watt-level output power now standard. However, beyond this progress, new functionalities and capabilities need to be added to this compact source to enable its integration into consumer-ready systems. Two main areas of development are particularly relevant from an application standpoint and were pursued during the course of this thesis: wavelength control and wavefront engineering of QCLs. The first research direction, wavelength control, is mainly driven by spectroscopic applications of QCLs, such as trace gas sensing, process monitoring or explosive detection. We demonstrated three different capabilities, corresponding to different potential spectroscopic measurement techniques: widely tunable single longitudinal mode lasing, simultaneous lasing on multiple well-defined longitudinal modes,

and simultaneous lasing over a broad and continuous range of the spectrum. The second research direction, wavefront engineering of QCLs, i.e. the improvement of their beam quality, is relevant for applications necessitating transmission of the QCL output over a large distance, for example for remote sensing or military countermeasures. To address this issue, we developed plasmonic lenses directly integrated on the facets of QCLs. The plasmonic structures designed are analogous to antenna arrays imparting directionality to the QCLs, as well as providing means for polarization control. Finally, a research interest in plasmonics led us to design passive flat optical elements using plasmonic antennas. All these projects are tied together by the involvement of Fourier analysis as an essential design tool to predict the interaction of light with various gratings and periodic arrays of grooves and scatterers.

Contents

List of Figures

"Il y avait, c'était sous le règne de Louis XVIII, à l'Académie des Sciences un Fourier célèbre que la postérité a oublié."

There was, under the reign of Louis XVIII, a celebrated Fourier at the Academy of Science, whom posterity has forgotten.

Victor Hugo, *Les Misérables*

"Derrière la série de Fourier, d'autres séries analogues sont entrées dans le domaine de l'analyse; elles y sont entrées par la même porte; elles ont été imaginées en vue des applications."

After the Fourier series, other series have entered the domain of analysis; they entered by the same door; they have been imagined in view of applications.

Henri Poincaré, *La Valeur de la Science*

Acknowledgements

I would like to thank my advisor, Prof. Federico Capasso, who warmly welcomed me in his group which he crafted into a very rich work environment from which I greatly benefited. Always enthusiastic, always deeply open to questioning, always welcoming and fostering discussion, he taught me that ideas are cheap and only acquire value when transformed by scientific debate and experimental validation.

I was privileged to work with wonderful fellow group members from whom I learned so much. I will always be indebted to Nanfang Yu, who welcomed me into the group and was my first mentor, teaching me many of the scientific skills I now have. He is a great role model, as a rigorous and incredibly productive scientist, but also for his reserve and humility: never an inaccurate word, never a bragging remark, never an undeserved critism against anyone. To Mikhail Kats, with whom I had the great pleasure to share most of this long adventure and who made an American out of me. To all of the characters I met in the Capasso group – Patrice Genevet, David Woolf, Tobias Mansuripur, Yu Yao, Steven Byrnes... just to name the loudest – who made my five and a half years here a rich, fun, and exciting experience. To the QCL team: Tobias Mansuripur, Patrick Rauter, Guy-Maël de Naurois, Burc Gokden, Stefan Menzel. To Christian Pflügl and Laurent Diehl who taught me so much about quantum cascade lasers. To Jenny Smythe, who guided my first steps in the cleanroom. To the collaborators I had the privilege to work with, Dr. Svetlana Boriskina and Prof. Luca Dal Negro at Boston University, Prof. Russ Dupuis at Georgia Tech, Drs. Masamichi Yamanishi and Kazuue

Fujita at Hamamatsu Photonics K.K., Drs. Christine Wang, Anish Goyal and George Turner at MIT Lincoln Laboratories. To Prof. Alexey Belyanin at Texas A&M for all the insightful discussions. I learned (and am still learning) a lot from him and it has always been a great pleasure interacting with him. To the students who allowed me to advise them over the years, Antoine Moulet, Jean-Philippe Tetienne, Cecile Grezes, Guillaume Aoust, Meinrad Sidler, Pauline Metivier, from whom I likely learned more from the experience than they did. To Chris and Xiomara, for their endless patience and skill in bureaucratic navigation. They are the engine of the group that keeps us moving forward. To the CNS staff who do such a great job at maintaining the tools and making processing possible. To all of my friends, both here and in France.

I would like to thank my family for their everlasting support. They guided me all my life and always supported my choices. And finally, to my wife, Joy, for her presence by my side, her encouragement and her constant love.

For Firmin and Albert,

my grandfathers

Introduction

Chapter 1

Introduction

1.1 Quantum cascade lasers

Quantum cascade lasers (QCLs) were first demonstrated in 1994 at Bell Laboratories [1] and have since seen rapid development from laboratory masterpiece to commercial product. A few milestones along the way were the first single mode device at room temperature in 1997 [2], followed by the first continuous wave operation at room temperature in 2002 [3], and the progressive development of spectroscopic applications [4]. QCLs now routinely reach Watt-level peak power and have been demonstrated over a large spectral range, from about 3 μm to 14 μm in the mid-infrared, and further in the terahertz range. Several application domains have sprung up, from military counter-measure, to remote chemical sensing and free-space communications.

Beyond their unsurpassed performance in covering the mid-infrared spectral range, QCLs feature a series of characteristics that make them truly unique laser sources:

- The complexity and size of the layer sequence composing the heterostructure of a QCL represent an immense step up from virtually all other semiconductor devices. Such development would have been impossible without dramatic improvements to epitaxial deposition techniques, from molecular beam epitaxy (MBE), developed by Alfred Cho at Bell Laboratories, to metal-organic vapor phase epitaxy (MOVPE), pioneered by Russell Dupuis, now at Georgia Institute of Technology. A typical mid-infrared QCL active region has about 40 heterostructure periods, each composed of about 25 layers of alternating InGaAs and InAlAs, for a total thickness between 2 and 3 μm.

- In opposition to laser diodes which rely on an interband transition, QCLs are remarkable in their reliance on an intersubband (IS) transition (see Fig. 1.1). The heterostructure itself quantizes the energy states of the electrons and create atomic-like energy levels (subbands), over which population inversion and optical gain can be achieved.

- The gain spectrum in diode lasers is set by the bandgap of the materials used. The materials need to be changed to significantly affect the emitted frequency of a laser. Most gas, dye, and solid-state lasers suffer from the same limitation since the optical transitions occur between material-given energy levels that are difficult to modify. QCLs free themselves from this "bandgap slavery", in the words of Prof.

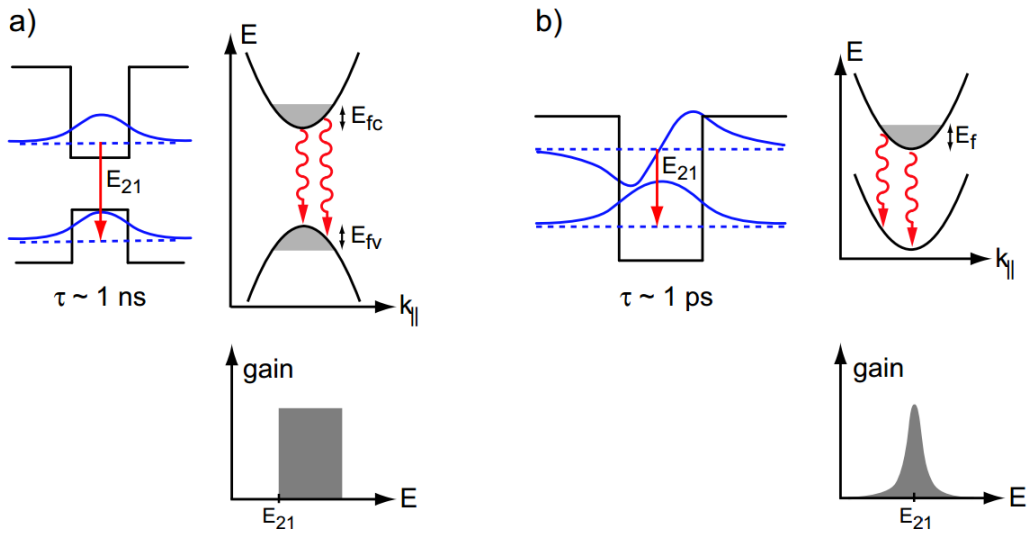

FIGURE 1.1: Principal characteristics of a) an interband transition and b) an intersubband transition in a quantum well. Reprinted from [5].

Capasso, since the transition energy between conduction subbands are set by the heterostructure, i.e. by the width of the quantum wells and barriers. This offers a tremendous design flexibility: developing a QCL at any wavelength between 3 μm and 14 μm is essentially possible by changing the geometric parameters of the heterostructure (layer sequence and thicknesses), with minor adjustments to the material alloy composition. Bandstructure engineering, i.e. the design of the heterostructure to achieve a certain subband landscape, becomes the most central component of QCL design.

- Beyond the engineering of the transition energy, the strength of the transition, i.e. the optical dipole matrix element, and the energy states lifetimes can also be tailored to meet specific requirements and achieve population inversion.

- The energy distribution of the light absorbed or emitted by this structure is peaked

at the energy difference between the subbands, and has a lorentzian shape with a width of typically a few percent of the peak energy. This is due to the fact that the parabolic dispersion curves (in k-space) of the subbands are mostly parallel to one another, resulting in an atomic-like joint density of states. One important consequence of this is that QCLs are mostly transparent for frequencies outside of their gain spectrum. Another consequence is that resonant phonon transitions (with a large in plane momentum) are far more probable. While this decreases the upper-state lifetime down to a few picoseconds, it also provides a convenient way to deplete the lower state and achieve population inversion.

- The width of the gain spectrum can be tailored via bandstructure engineering. In QCL designs known as "bound-to-continuum", multiple IS transitions can occur from a single upper state to several closely spaced lower states forming a miniband. A large composite gain spectrum can thus be obtained by superposition of the individual lorentzian gain curves from each IS transition. This is a mechanism for homogeneous gain broadening.

- QCLs are unipolar devices: electrons remain in the conduction band throughout the structure, and can thus undergo multiple successive IS transitions in a cascading scheme. As one photon goes through the active region, it can generate multiple photons. This effect is responsible for the high power that QCLs achieve.

- The fact that QCLs are mostly transparent for frequencies outside of their gain spectrum, added to the fact that they are unipolar devices, can be used to stack

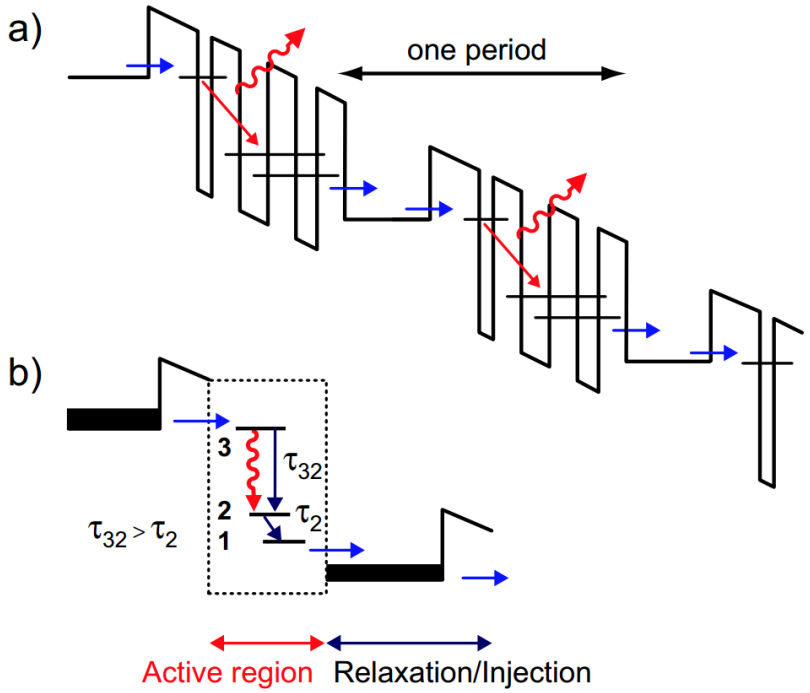

FIGURE 1.2: a) Schematic conduction band diagram of a quantum cascade laser. Each stage of the structure consists of an active region and a relaxation/injection region. Electrons can emit up to one photon per stage. b) General philosophy of the design. The active region is a three-level system. The lifetime of the $3 \rightarrow 2$ transition has to be longer than the lifetime of level 2 to obtain population inversion. Reprinted from [5].

different structures in series to form an heterocascade having a very large composite gain. This is a mechanism for inhomogeneous gain broadening.

- QCLs are TM polarized (i.e. linearly polarized perpendicularly to the epitaxial layers plane). This is the result of selection rules for an IS transition.

- Population dynamics in quantum cascade lasers are very fast, with most characteristic times (upper state lifetimes, recovery time, etc...) on the scale of the picosecond. In particular, the recovery time for the population inversion (via tunneling through the superlattice) is faster than the carrier diffusion times. The

standing wave pattern of the optical field intensity in a Fabry-Perot resonator will thus burn a gain grating that will not be washed away by diffusion. This leads to an inhomogeneous gain saturation along the laser cavity and leaves gain available for new modes to reach threshold after the initial mode starts lasing. As a result, QCLs in a Fabry-Perot cavity are often very multimode, lasing on as much as several hundred modes simultaneously, covering a spectral range up to ≈ 350 cm^{-1} wide (but more often around 50 cm^{-1}).

1.2 Adding functionalities to quantum cascade lasers

More could be added to this long list of exceptional characteristics of QCLs and an interested reader will find more details in [6]. Since their first demonstration in 1994, a large research effort was made to use these characteristics to improve the performance and functionalities of QCLs. However, a lot remains to be done. While bandstructure engineering is now reaching a fairly steady state, optical waveguide design of QCLs and their integration into complex photonic circuits can improve significantly to reach the level of development seen in silicon photonics. Spectroscopic applications are pushing the development of wavelength-control techniques in QCLs towards ultra-broadband tuning or the emission of mid-infrared frequency combs. Mode-locking of QCLs also remains elusive and the study of their nonlinear dynamics is still in its infancy. Another frontier for the development of QCLs is the improvement of their beam quality, which is critical

for applications requiring long distance propagation, such as remote sensing, military countermeasures, or free-space communication.

1.3 Overview of thesis work

During my thesis, I pursued two main areas of development for QCLs: wavelength control and beam engineering.

1.3.1 Wavelength control of quantum cascade lasers

I developed new solutions for the wavelength control of QCLs, through the use of novel waveguide designs and distributed feedback grating structures. Three different functionalities were pursued:

- Widely tunable single longitudinal mode lasing
- Simultaneous lasing on multiple well-defined longitudinal modes
- Simultaneous lasing over a broad and continuous range of the spectrum

Applications of such capabilities are discussed in Chapter 2.

Together with my colleagues in the group of Prof. Capasso, we proposed a new class of gratings having multiple spatial frequencies [7]. Their design relies on the use of small aperiodic grating sequences as unit cells whose repetition forms a superlattice. The superlattice provides well defined Fourier components, while the choice of the unit cell

structure enables the selection, modulation, or suppression of certain Fourier components. Using these gratings to provide distributed feedback in mid-infrared quantum cascade lasers, we demonstrated simultaneous lasing on multiple well-defined and isolated longitudinal modes, each one having a sidemode suppression ratio of about 20 dB. This work is presented in Chapter 3.

Using these lasers, we demonstrated a multi-wavelength distributed feedback (DFB) quantum cascade laser (QCL) operating in a lensless external micro-cavity and achieved switchable single-mode emission at three distinct wavelengths selected by the DFB grating, each with a side-mode suppression ratio larger than 30 dB. Discrete wavelength tuning is achieved by modulating the feedback experienced by each mode of the multi-wavelength DFB QCL through a variation of the external cavity length. This method also provides a post-fabrication control of the lasing modes to correct for fabrication inhomogeneities, in particular related to the cleaved facets position. This work is presented in Chapter 4.

In parallel, efforts in the group led to the development of sampled gratings for broadband tuning of a single-mode [8]. Details on this work can be found in section 3.2.

Additionally, we demonstrated 1.1 W peak power at room-temperature from a double-waveguide quantum cascade laser (QCL) grown by metal-organic chemical vapor deposition [9]. Two full broadband QCL active regions were grown on top of each other separated by thick cladding layers to reduce gain competition. Simultaneous lasing on Fabry-Perot modes separated by as much as 360 cm^{-1} was obtained. This design paves

the way for high-brightness broadband mid-infrared sources, as well as more complex three-terminal devices. It is presented in Chapter 5.

1.3.2 Wavefront control of quantum cascade lasers

I also worked on wavefront engineering of QCLs, i.e. the control of their output beam shape and polarization state, mainly through the use of plasmonic lenses directly integrated on the laser facet.

After an initial work with Nanfang Yu on the development of plasmonic collimators (for a review, see [10]), I designed with my colleagues a new class of plasmonic gratings that generate multiple free-space beams in arbitrary directions from a point source of surface waves, using a phenomenological model we developed which accurately predicts their far-field, in amplitude, phase and polarization [11]. The model, introduced in Chapter 7, can be used for the design of general two-dimensional plasmonic gratings. We fabricated such gratings on the facets of quantum cascade lasers, as a proof of principle and a stepping stone toward the development of integrated dynamic beam steering solutions. The experimental work is presented in Chapter 8.

In order to prove the applicability of plasmonic collimators to high power lasers, we fabricated them on the facet of tapered quantum cascade laser with sloped side-walls emitting a high-brightness single-lobe beam at 8.1 μm with a peak power of 4 W at room temperature [12]. The collimated lasers emit a beam with a more cylindrical cross-section which is more amenable to high-efficiency coupling into mid-infrared optical

fibers. Further optimization of the lasers through the use of facet coatings yielded a power output as high as 6.2 W (without plasmonic collimator) while the high beam quality was maintained. This work is presented in Chapter 9.

1.3.3 Design of passive flat optical elements using plasmonic antennas

Since the study of surface plasmons and plasmonic structures was an important part of these projects, I was able to develop a side interest in the design of passive flat optical elements using plasmonic antennas.

We proposed and demonstrated with my colleagues a novel photonic-plasmonic antenna capable of confining electromagnetic radiation at several mid-infrared wavelengths to a single sub-wavelength spot [13]. The structure relies on the coupling between the localized surface plasmon resonance of a bow-tie nanoantenna with the photonic modes of surrounding multi-periodic particle arrays. Far-field measurements of the transmission through the central bowtie demonstrated the presence of Fano-like interference effects resulting from the interaction of the bow-tie antenna with the surrounding nanoparticle arrays. The near-field of the multi-wavelength antenna was imaged using an aperture-less near-field scanning optical microscope. This antenna design is relevant for the development of near-field probes for nanoimaging, spectroscopy, and biosensing. This work is presented in Chapter 10.

Finally, we presented a simplified numerical method to solve for the current distribution in a V-shaped antenna excited by an electric field with arbitrary polarization [14]. The

scattered far-field amplitude, phase, and polarization of the antennas are extracted. The calculation technique, presented in Chapter 11, is an efficient method for probing the large design parameter-space of such antennas, which have been proposed as basic building blocks for the design of ultrathin plasmonic metasurfaces. Our calculation is based on the Integral Equation Method of Moments and was validated by comparison to the results of finite-difference time-domain (FDTD) simulations. The computation time is approximately five orders of magnitude less than for FDTD simulations.

1.4 Fourier optics

Almost all these projects are tied together by the involvement of gratings and periodic arrays of grooves and scatterers, placing Fourier analysis at the forefront of my thesis.

When Fourier analysis and Fourier transforms are taught in school, the context is often that of finding the spectrum of a one dimensional signal, i.e. the different periodicities composing the signal. Fourier analysis is often presented as a technique to obtain information on a signal, but practical and physical aspects are often neglected. Optics, however, is a field where Fourier analysis finds very striking physical expressions, due to the wave-like nature of light, and the resulting interference phenomena that can be observed. Analyzing the geometrical periodicities of a structure, one can understand the different paths taken by light as it interacts with this object: in a word, Fourier analysis provides a very efficient tool to predict how complex objects will scatter light.

During the course of my thesis work, I had the opportunity to explore several such practical applications of Fourier analysis, in both active and passive photonic devices, from the design of complex multi-wavelength distributed feedback gratings for wavelength selection in lasers to the arrangement of periodic arrays of plasmonic antennas into hierarchical metallic patterns to create nano-scale high intensity spots of light, or the fabrication of plasmonic antenna array on the facet of quantum cascade lasers to shape their output beam.

Part I

Wavelength control of QCLs

Chapter 2

Introduction to broadband quantum cascade lasers

2.1 Quantum cascade lasers with broadband gain

Most atmospheric trace gases, including CO_2, NO, CH_4, and NH_3, have rotational-vibrational resonances in the mid-infrared (mid-IR) portion of the spectrum, typically between 3 and 16 μm. These resonances provide a unique "fingerprint" for each molecule, which can be identified by an absorption spectroscopy experiment. While a broadband illumination source, such as a Globar (TM), together with a Fourier transform infrared (FTIR) spectrometer can be used for this purpose, the resulting set-up is bulky and contains moving parts. Better portability and sensitivity can be achieved with a narrow linewidth, broadly tunable, high power laser source in the mid-IR, which eliminates

the need for a spectrometer. Quantum cascade lasers (QCLs) are uniquely positioned to satisfy these requirements since they are near-ideal mid-infrared semiconductor light sources, combining wavelength agility [15] and operation at room temperature with continuous-wave Watt-level output power [16]. They enable coverage of the mid-infrared region of the electromagnetic spectrum which is of great importance for many applications beyond chemical sensing [4], from free space communication to countermeasures.

It was realized early in the development of QCLs [17] that these lasers have several particularities that make them attractive for broad-band or multi-band operation. As they rely on intersubband (IS) transitions, their gain spectrum is not set by the bandgap of the materials used but can be selected by bandstructure engineering. Furthermore, as the IS transitions give rise to Lorentzian lineshapes, the energy distribution of the light that is emitted or absorbed is peaked at the energy difference between the sub-bands which makes the heterostructure mostly transparent to light with frequencies outside the gain spectrum. Many different active regions can thus be stacked on top of each other in the same waveguide, helped by the fact that electrons keep cascading from one active region to the other as they remain in the conduction band while traversing this unipolar device. These characteristics of QCLs can be used to generate very wide composite gain spectra and achieve simultaneous broadband lasing [17]. Broad-gain QCLs can also be realized using a homogeneous active region composed of the repetition of a unique cascade design, as in the so-called bound-to-continuum QCLs [18], or as impressively demonstrated with more recent developments in bandstructure engineering [19, 20].

2.2 Tunable single-mode operation

Single mode emission is usually achieved by etching gratings into the waveguide to create a distributed feedback QCL (QC-DFB) [2], or by etching the grating into a section directly adjacent to the Fabry-Perot (FP) cavity to form a distributed Bragg reflector (DBR) [21]. Wavelength tuning is achieved by exploiting the temperature dependence of the refractive index [22], either by varying the heat sink temperature or by applying a small dc bias current to cause Joule heating of the active region. In both DFB and DBR devices, the maximum fractional wavenumber tunability $\Delta k/k$ is given by the relative modal refractive index change $\Gamma \Delta n/n$, where Γ is the mode overlap factor. Typically, this results in a tuning range of no more than 5 cm^{-1} for current-induced temperature tuning. This spectral coverage is sufficient to detect a molecular absorption line of a gas species, but the large gain bandwidth of QCLs allows for more ambitious detection schemes.

A wider tuning range allows for multi-line detection, which facilitates calibration and unambiguous identification of chemicals. One such scheme with broad tuning capability is the laser array [23, 24], a single chip that monolithically integrates thirty-two QC-DFBs, each spaced apart spectrally by 9.5 cm^{-1} for a total spectral coverage of about 220 cm^{-1}. Very high peak output power has recently been achieved by an array of DFB QCLs integrated with optical amplifiers [25, 26]. However, emitter arrays require high fabrication yield and beam combining optics. Overlapping the beams in the far field has been successfully demonstrated using wavelength beam combining with a suitable

grating [27, 28].

The widest spectral coverage to date has been achieved by placing a single multi-stack QCL with a bound-to-continuum active region design within an external cavity in the Littrow configuration [29], and using a rotating grating to provide wavelength-specific feedback to the QCL. The device lases in single mode over a range of 432 cm^{-1} from 7.6 to 11.4 μm. Truly continuous and mode-hop free tuning in the external cavity configuration requires broadband anti-reflection (AR) coatings with very low reflectivity and precise and active control of both the grating angle and cavity length, which constrain device portability, reliability and ruggedness.

Ideally, the full bandwidth of the QCL gain medium could be accessed continuously, one single mode at a time, in a monolithic device with a single output. This would eliminate the need for beam combining and minimize the amount of driving electronics, thereby providing a cheap, compact, robust platform for trace gas detection. We have made significant progress [8] towards this goal through the use of a three-section QCL that consists of a standard FP gain section placed between two "sampled grating" distributed Bragg reflector (SGR) sections, a strategy that was first pursued at telecom wavelengths [30]. Sampled gratings will be further described in section 3.2.

2.3 Simultaneous multi-band lasing

Some applications, especially in the field of spectroscopy and ranging, would benefit from simultaneous lasing at several well-defined wavelengths. In particular, a multi-wavelength QCL could be used to implement multicomponent gas analysis and differential spectroscopic techniques such as differential absorption LIDAR (light detection and ranging), a very sensitive technique for trace gas sensing [31]. In addition, multi-wavelength QCLs could be useful as multichannel sources in wavelength-division multiplexing (WDM) free-space optical communication or for room-temperature difference-frequency generation of terahertz light [32].

We demonstrated a multi-wavelength QCL operating on a few well-defined wavelengths, each of these being "single-mode" in the sense that their sidebands are strongly suppressed [7]. In order to achieve this result, we devised a new class of gratings having multiple interleaved spatial frequencies. Details are presented in Chapter 3. Additionally, we demonstrated a multi-wavelength distributed feedback (DFB) quantum cascade laser (QCL) operating in a lensless external micro-cavity and achieved switchable single-mode emission at three distinct wavelengths selected by the DFB grating, each with a side-mode suppression ratio larger than 30 dB [33]. Details are presented in Chapter 4.

2.4 Simultaneous broadband lasing

Some applications would require *simultaneous broadband* lasing. In particular, Fourier-transform infrared (FTIR) spectrometers, which are widely used chemical analysis tools, still rely on thermal radiation sources. The low infrared power from these sources restricts the use of FTIR spectrometers to low-absorptivity samples. Developing broadband QCLs as high-brightness sources for FTIR spectrometers would enable new applications, such as solvent-based process monitoring. Mid-infrared optical coherence tomography systems [34] could also be envisioned with such sources. Finally, assuming proper control over the comb of frequencies emitted, advanced infrared comb spectroscopy techniques could be developed [35].

Lasing mode proliferation across the gain spectrum [17] is enabled by a low threshold for the spatial hole burning instability in QCLs [36]. Simultaneous lasing over a range as wide as 360 cm^{-1} with a small gap of 36 cm^{-1} has been reported [29]. However, broadband simultaneous lasing remains very challenging because of the need to achieve a flat net gain spectrum in order to ensure that all lasing wavelengths have the same threshold. We developed a new double-waveguide QCL whose design provides flexibility to distribute multiple QCL stages over two weakly-coupled optical waveguides, in order to obtain broadband emission while dealing with common issues of heterocascade QCLs, such as cross-absorption and gain competition [9]. Details are presented in Chapter 5.

Chapter 3

Multi-wavelength quantum cascade lasers

3.1 Introduction to distributed feedback gratings for singlemode lasing

A common method to obtain single-mode emission of a semiconductor laser is to use a grating defined directly in the laser waveguide to provide distributed feedback (DFB) [37]. In such DFB lasers, the periodic modulation of the refractive index introduced by the grating opens a gap at the Brillouin zone boundary in the waveguide dispersion relation. At the edges of the gap, the group velocity goes toward zero, which corresponds to a very high density of optical states. The laser will thus likely operate on one of these two gain-favored band-edge modes. Note that in the case where the two modes

experience approximately the same amount of gain and loss, true single mode operation may be prevented. A common solution is then to introduce a $\lambda/4$ spacer in the middle of the grating. The laser will now operate at the wavelength corresponding to the defect state that is created within the photonic bandgap. It corresponds to fields localized at the defect and exponentially decaying on both sides into what now amounts to two sets of Bragg reflectors. This simple picture is valid in the case of *index*-coupled DFB lasers, i.e. when the real part of the refractive index is periodically modulated. *Gain*-coupled DFB lasers have also been demonstrated and they present a different behavior, with in particular the absence of a bandgap in frequency [37]. We focus here on *index*-coupled DFB lasers.

3.2 Sampled gratings

3.2.1 Fourier analysis of sampled gratings

We are interested in obtaining a multi-wavelength QCL operating on a few well-defined wavelengths, each of these being 'single-mode' in the sense that their sidebands are strongly suppressed. In order to achieve this result, we devise a new class of gratings having multiple interleaved spatial frequencies.

An early demonstration of a two-color QCL used two DFB gratings defined side-by-side on top of a laser waveguide [22]. This simple multi-section design is however impractical for lasing on a larger number of wavelengths. More generally, multi-wavelength lasing can be achieved by using a grating whose Fourier spectrum contains several discrete

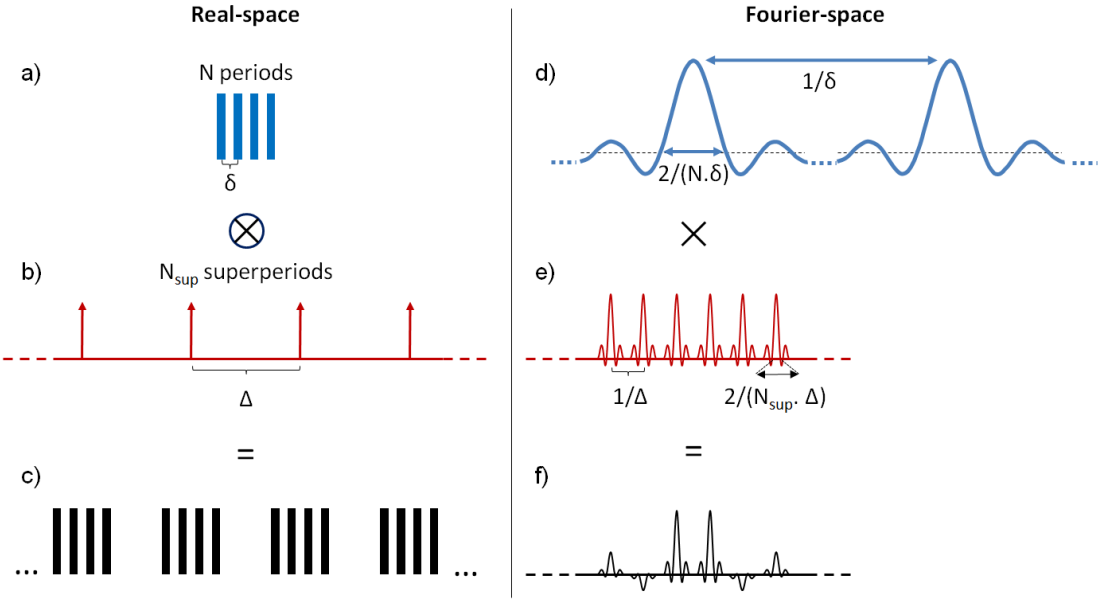

FIGURE 3.1: Schematic of a sampled grating in real-space and Fourier space. The sampled grating (c) is formed as the convolution of a short N-element section of a δ-periodic grating (a) and an N_{sup}-element Δ-periodic comb of delta functions (b). The thick vertical bars represent the spatial refractive index profile (succession of low and high index layers) that constitute the physical grating. We assume that $N.\delta < \Delta$ and $N_{sup} >> 1$. Not represented on the schematic is the fact that the short N-element section itself can be seen as the multiplication of a boxcar function of width $N.\delta$ and an infinite δ-periodic grating. The Fourier transform of the short N-element section is thus the convolution of the Fourier transform of a boxcar function, i.e. a *sinc* function of width $2/(N.\delta)$, with the Fourier transform of an infinite δ-periodic grating. It is thus an infinite series of *sinc* functions spaced by $1/\delta$, with a large-scale amplitude modulation (not represented on the schematic), corresponding to the Fourier transform of the δ-periodic grating unit cell (d). We are only interested in the first *sinc*-shaped peak, corresponding to the first order of the grating. The Fourier transform of the full sampled grating (f) is obtained as the multiplication of that *sinc*-function with the Fourier transform of an N_{sup}-element Δ-periodic comb of delta functions (e), i.e. an infinite $1/\Delta$-periodic comb of *sinc*-functions of width $2/(N_{sup}.\Delta)$.

peaks, each corresponding to the opening of a gap in the waveguide dispersion relation. An example of such grating is given by a sampled grating, developed initially as a mean to obtain wide tuning range in distributed Bragg reflector (DBR) semiconductor lasers [30]. It can be described as a standard first-order periodic grating with period $\delta \simeq \lambda/2$ (a Bragg grating) in which a number of grating elements are removed periodically to

create a 'superlattice' with period $\Delta > \delta$. In other words, the structure of the grating is that of a standard periodic grating multiplied by a sampling square function imposing a superperiodicity. The corresponding Fourier spectrum is obtained as the convolution of the Fourier transform of the grating and that of the sampling function and it features a set of narrow peaks.

We prefer an alternative description of sampled gratings as represented in figure 3.1, where the structure is seen as the convolution of a short grating with a long lattice of delta functions. The Fourier transform of such a structure is thus obtained by multiplying the Fourier transform of the finite-length lattice, an infinite array of narrow *sinc*-shaped peaks, with the Fourier transform of the short grating that forms a broad envelop. This is reminiscent of the picture crystallographers use when describing crystal lattices with a basis [38]. Indeed, some crystals can be described as a Bravais lattice where each unit cell is itself composed of several atoms. When studying X-ray diffraction patterns of these crystals, considering only the Bravais lattice is not sufficient and one needs to add a structure factor to include the interference of scattered fields coming from different atoms within a unit cell. This structure factor is a Fourier transform of the unit cell. The total scattering amplitude can be calculated by multiplying the Bravais lattice scattering amplitude with the structure factor.

3.2.2 Single-mode lasing using sampled grating reflectors

As a side interest, we present here in more details how sampled gratings can be used for single-mode selection.

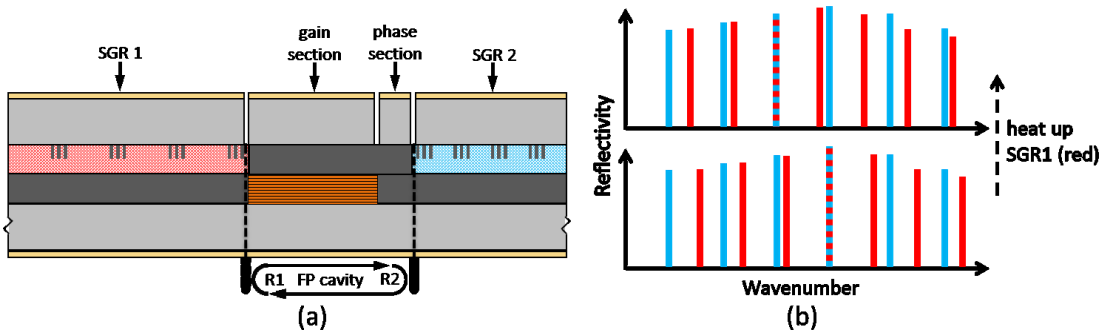

FIGURE 3.2: (a) Schematic of a typical sampled grating DBR laser, consisting of two sampled grating reflectors (SGR) with slightly different superperiods on each side of a Fabry-Perot (FP) cavity. The phase section controls the round-trip phase accumulation, which is critical for continuous tuning, but is not included in our device. Traditionally, the gain medium (orange) is restricted to the gain section and the facets are AR-coated, but in our device the SGRs also have gain and the facets are left uncoated. (b) Reflectivities of the SGRs and basic tuning mechanism. Light traveling in the FP cavity experiences a reflection at both SGRs whose magnitude depends on the frequency of the light. The reflectivities of the two SGRs are depicted as frequency combs (SGR1=red, SGR2=blue) with slightly different spacings due to the difference in the superperiods. When peaks from the two SGRs overlap at a particular frequency, the neighboring peaks do not. Therefore, light at the overlap frequency will experience a large reflection at both SGRs and have a lower lasing threshold compared to other modes. To tune the laser frequency, SGR1 is heated so that its refractive index increases and the reflectivity spectrum correspondingly shifts towards smaller wavenumbers, while SGR2 is not index tuned. The resulting alignment of the two combs is seen to cause a discrete mode hop to a mode with smaller wavenumber. (Not shown: heating SGR2 will instead cause the mode to hop to a larger wavenumber.)

Single mode emission and tuning using sampled-gratings reflectors (SGR) was first demonstrated in [30]. A schematic of the device geometry is shown in Fig. 3.2(a). Very recently the concept was demonstrated in QCLs using a two-section device operating as two SG-DFB coupled cavities [39]. The two SGRs are chosen to have slightly different comb spacings so that when two of the peaks are aligned, the neighboring peaks are not. In this way, light which travels one roundtrip in the FP cavity sees the largest feedback at the wavelength for which the reflectivity peaks from the two mirrors overlap, and this condition determines the mode with the lowest lasing threshold. Discrete

tuning is achieved by heating one SGR section so that its reflectivity spectrum shifts in frequency; for a small shift, two new peaks from each comb will come into alignment as shown in Fig. 3.2(b), causing a discrete jump in the lasing mode. This is known as Vernier tuning by analogy with the Vernier scale, which also utilizes mismatched combs [30]. This strategy overcomes the tuning limitation imposed by the maximum refractive index tuning acheivable. To achieve quasi-continuous tuning, the two SGR sections must be heated at the same time so that both reflectivity spectra translate together in k-space. To prevent mode hops and achieve truly continuous tuning, a tunable phase section inside the FP cavity is needed to ensure that the wavelength selected by the two SGRs also corresponds to a cavity mode satisfying the roundtrip 2π phase accumulation condition; this section is not, however, critical for demonstrating discrete tuning. Continuous tuning is still limited by the maximum tuning of the waveguide effective refractive index, and so by setting the comb spacing close to one half of the maximum amount of continuous tuning, it is in principle possible to achieve wide spectral coverage through a combination of discrete jumps and continuous tuning.

In order to illustrate the mode selection and tuning mechanism, we show in Fig. 3.3 the simulated reflectivity spectra of both SGRs, along with the product of the two reflectivities, for a realistic grating geometry. From Fig. 3.3(a), we see the mismatch $k_1 - k_2 = 0.65$ cm^{-1} was chosen to be slightly larger than the linewidth of the reflectivity peaks, so that when two peaks overlap strongly their nearest neighbors do not. There is a 'repeat period' $k_{\text{rep}} \approx k_1 k_2/(k_1 - k_2) = 26$ cm^{-1} after which two additional peaks overlap, as seen in Figs. 3.3 (b) and (c), but the reflectivity product is larger for the

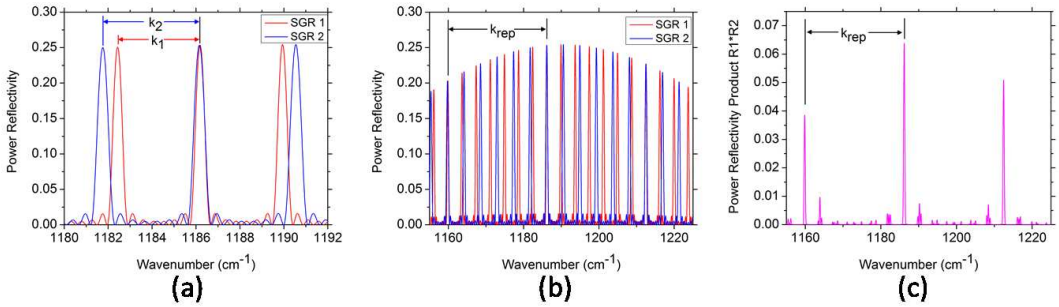

FIGURE 3.3: (a) Simulated reflectivity spectra of the two SGRs using the experimental device parameters (with AR coatings assumed on the device facets), showing the two different comb spacing values $k_1 = 3.75$ cm^{-1} and $k_2 = 4.40$ cm^{-1}. (b) Zoomed-out view which shows the repeat spacing at $k_{\text{rep}} = 26$ cm^{-1} as well as the envelope modulation of the spectra. (c) Product of the two reflectivities which shows the modes with the largest feedback.

primary peaks due to the decaying envelope. In the simple Vernier tuning picture, the total amount of tuning cannot exceed k_{rep} because the peak with the largest reflectivity product will always be within $k_{\text{rep}}/2$ of the center of the envelope. One can increase k_{rep}, and thus the tuning range, by reducing the mismatch $k_1 - k_2$, but at a cost of reducing the SMSR because the nearest neighbors of the overlapping peaks will overlap more strongly. An excellent discussion of these tradeoffs is given in [30].

In the simulations shown in Fig. 3.3, AR-coated facets are assumed in order to more easily identify the relevant comb peaks. In the experimental device, the lack of coatings will lead to a baseline reflectivity of $|(n-1)/(n+1)|^2 = 0.27$, where n is the effective index of the laser waveguide. The contribution of the grating to the reflectivity (between 0.20 and 0.25 at the comb peaks) is comparable to the facet reflectivity, and therefore crucial in determining the lasing mode. The simulation also assumes that the SGRs are transparent. Because the SGRs contain the same active region as the FP section, this

assumption is only strictly valid when each SGR is pumped at the transparency current, when the gain equals the waveguide loss. For smaller (larger) currents, the reflectivity will be smaller (larger) in magnitude. (If the threshold current is exceeded, however, the SGR can act as a DFB laser rather than as a reflector for the FP cavity, which is a separate matter.) In diode SG-DBR lasers, the mirror sections are regrown with passive material, and the index tuning is accomplished by electron plasma and band filling effects which result from current injection [40]. The refractive index of the QCL is much less sensitive to such effects due to the intersubband nature of the transition. Instead, we rely on thermal index tuning resulting from current-induced Joule heating. Including the active region in the SGR sections allows us to take advantage of the QCL material's ability to generate heat very efficiently.

Discrete mode hopping is achieved by tuning the refractive index of one of the mirror sections, say SGR1, while the other remains unchanged, which translates the reflectivity spectrum of SGR1 in k-space and brings the neighboring peaks into alignment. To see why an index change results in a translation, consider a small index change from n to $\Delta n + n$ in SGR1 which results from a temperature increase in the InAlAs/InGaAs materials. This causes a small shift in the peak of the reflectivity envelope. The more significant effect is the change in the optical path length of the superperiod which affects the comb spacing ($k_1 \rightarrow k_1 + \Delta k_1$): the entire comb contracts when the SGR is heated with the center of contraction at $k = 0$. The Nth peak (where N is an integer which counts each peak beginning at k=0) shifts by an amount $N\Delta k_1$. In our particular design, we are interested only in the peaks with N between 314 and 320, which corresponds

to the small spectral window of 26 cm^{-1} near k=1190 cm^{-1}. These few peaks shift by almost the same amount, and so the contraction manifests itself as a translation towards smaller wavenumbers. However, if one were to design a device with tuning range greater than 200 cm^{-1} then the comb contraction would be relevant and the Vernier tuning mechanism not so straightforwardly applicable. The index dispersion would also need to be accounted for, resulting in unevenly spaced comb lines.

Using the sampled-grating reflector design presented here, a three-section sampled grating QCL was fabricated in our group and provided a clear demonstration of discrete mode hopping across the entire repeat period of 26 cm^{-1} with no missing modes [8]. Furthermore, we have demonstrated that the device is capable of lasing at additional modes not predicted by the conventional sampled grating theory, yielding a tuning range of 63 cm^{-1}, from 8.32 to 8.78 μm.

3.3 Gratings with an aperiodic basis

3.3.1 Description

Our understanding of sampled gratings as being the convolution of a periodic array with a short first-order grating section opens interesting perspectives for the design of more general multi-wavelength gratings. Let us consider a grating composed of the periodic repetition of a small aperiodic grating element, i.e. whose layers are arranged following an arbitrary sequence (Fig. 3.4 (a)). Its real-space structure is formed as the convolution of the short aperiodic sequence with a finite comb of delta functions. As described above,

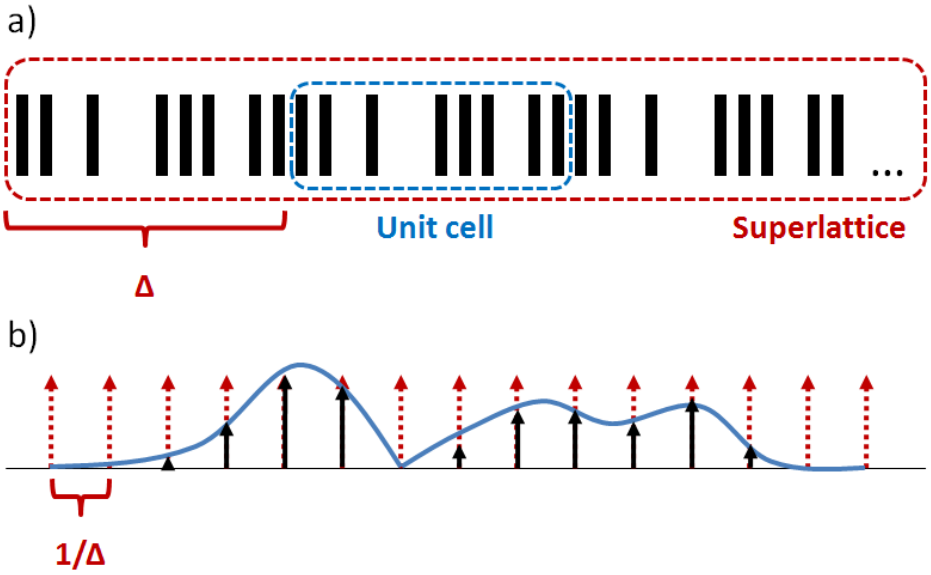

FIGURE 3.4: Schematic of a grating with an aperiodic basis. (a) Real-space structure, with a unit cell of length Δ repeated periodically to form a superlattice. The thick vertical bars represent the spatial refractive index profile that constitutes the physical grating. (b) Fourier-space. The Fourier transform of the grating (black) is obtained by multiplying the Fourier transform of the superlattice (red) with the Fourier transform of the unit cell (blue). For simplicity, narrow *sinc* functions are represented as arrows in the Fourier spectra.

the Fourier transform is obtained as the multiplication of the Fourier transform of the comb of delta functions by the envelope function formed by the Fourier transform of the short grating sequence (Fig. 3.4 (b)). By proper design of this short element, we can shape an envelope to select, modulate or suppress specific teeth of the underlying comb of frequencies. If such a grating is integrated into a laser waveguide, we expect lasing to occur at the edges of the bandgaps corresponding to the different Fourier transform peaks. We emphasize that these peaks are due to the superperiodicity of the grating, and their amplitude is modulated by the interference between the different scattering paths within each unit cell. We will refer to these gratings as *gratings with an aperiodic basis* (GABs).

GABs are a generalization of sampled gratings where instead of a short periodic array we use an aperiodic array as the unit cell. Another particular implementation of this general concept is given by periodically chirped or superstructure gratings [41]. These gratings rely on a periodic modulation of the grating periodicity or of the grating phase. By opening the range of possible unit cells to aperiodic sequences, GABs enable to use an entire new range of properties in the gratings design, in particular the properties of deterministic aperiodic sequences rooted in number theory [42].

3.3.2 Alternative multi-wavelength gratings

While the gratings discussed here are based on a comb of modes stemming from a superperiodicity, there exists a more direct approach to obtain a small number of discrete peaks in the Fourier spectrum of a grating. It consists of superimposing *sine* gratings with different periodicities. The Fourier transform being a linear operation, the Fourier spectrum of the resulting grating will be the sum of the different Fourier spectrums of the underlying gratings. As an analog superposition of *sine* gratings presents many fabrication challenges, the concept was best implemented after binary digitization of the multi-component grating, forming a sequence of low and high refractive index layers (hence the term *binary*) [43]. The digitization represents only an approximation of the analog grating and introduces higher harmonics. A fine sampling frequency is necessary to obtain good performances. These binary superimposed gratings (BSG) offer the advantage of having built-in degrees of freedom to set the individual positions and amplitudes of the reflection peaks.

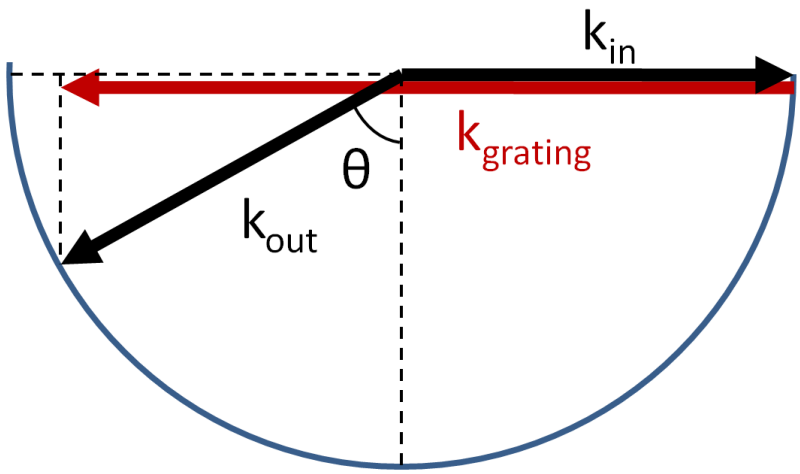

FIGURE 3.5: Schematic of grating scattering. Light impinges on the grating with wavevector k_{in}. The grating provides the momentum $k_{grating}$. The outgoing wavevector k_{out} must lie on the blue circle representing conservation of energy. Conservation of in-plane momentum then sets the out-going direction.

Multi-wavelength operation has also been reported by Mahler *et al.* [44] using quasi-periodic DFB lasers based on a Fibonacci sequence. The particularity of this sequence lies in its pure-point measure with discrete Fourier peaks at irrational ratios [42, 45]. As discussed before, each peak corresponds to the opening of a bandgap at the edges of which a lasing mode can be selected. However, this design presents only limited flexibility in term of peak position and amplitude. In the context of GABs, one could imagine using a Fibonacci sequence within the unit cell to obtain an envelope selecting several spectral regions.

We have presented so far different strategies to design a grating having several well defined spatial frequencies. For the rest of this work, we will focus on GABs because we consider that the great flexibility offered by the design of the unit cell offers interesting perspectives, both from a technological and a fundamental point of view. While it is

true that the Fourier components are weaker for GABs than for BSGs, high coupling coefficients are not always desirable for QCLs. It is usually assumed that the optimal coupling coefficient κ of a DFB grating is such that $\kappa.L = 1$, where L is the length of the laser cavity [37]. This ensures a good balance between the outcoupling efficiency and the overlap between the optical mode and the gain medium. Since typical lengths L for QCLs are on the order of a few millimeters, a low coupling coefficient is often preferred. In the limit of lasing on several narrowly-spaced wavelengths, a low coupling coefficient would also be necessary as it results in spectrally narrow bandgaps and thus avoids their overlap. GAB lasers could also present advantages in term of fabrication yields for applications requiring precise wavelengths of operation. Since their unit cell may feature long uniform sequences of successive similar index layers for which overexposure has practically no impact, the optical length of the unit cell (i.e. the superperiod) should be robust to such fabrication errors and thus the relative error on the lasing wavelength is likely to be lower than for DFB or BSG lasers.

3.3.3 Scattering losses

Scattering losses might impact device performance for multi-wavelength grating lasers. So far in our analysis of the gratings, we considered a purely one-dimensional problem. However, as represented in figure 3.5, when $k_{grating} < 2k_{in}$, there is a scattering path for an outgoing wave whose direction is not parallel to the laser waveguide. If the angle θ formed between the normal to the waveguide layers and the outgoing wavevector is smaller than the total internal reflection angle at the waveguide walls, light will leak out

of the laser waveguide and will be absorbed in the laser substrate. Because the gratings we study here are based on a comb of modes, this seems to be a particularly strong concern. Indeed, the gratings have many Fourier components such that $k_{grating} < 2k_{in}$, each corresponding to an additional scattering path. From Parseval's theorem applied to a numerical sequence with a flat Fourier spectrum over a compact bandwidth, the amplitude of the peaks in the Fourier spectrum can be considered inversely proportional to the number of peaks. The sum of the GABs Fourier peak amplitudes should thus be comparable to the amplitude of the single Fourier peak of a second-order grating (i.e. a grating such that $k_{grating} = k_{in}$), used successfully in the past to demonstrate high performance surface emitting lasers [46, 47]. We can thus expect the threshold to be comparable for GAB lasers and surface emitting lasers, since the scattering losses are comparable.

3.3.4 Design and fabrication

It may seem at first uncertain whether single mode operation, desired in each lasing wavelength region, would be preserved with GAB lasers, as the lasing mode corresponds to a high scattering order, and thus to a relatively low amplitude Fourier component. Furthermore, one could wonder if introducing disorder within the unit cell, for example by using a unit cell with a random sequence (the same random sequence being repeated to form the superlattice), would have a negative impact on the laser behavior, since it corresponds to more complex scattering paths. In order to verify these points, we fabricated lasers with relatively large unit cells and 'reduced' short-scale order. We

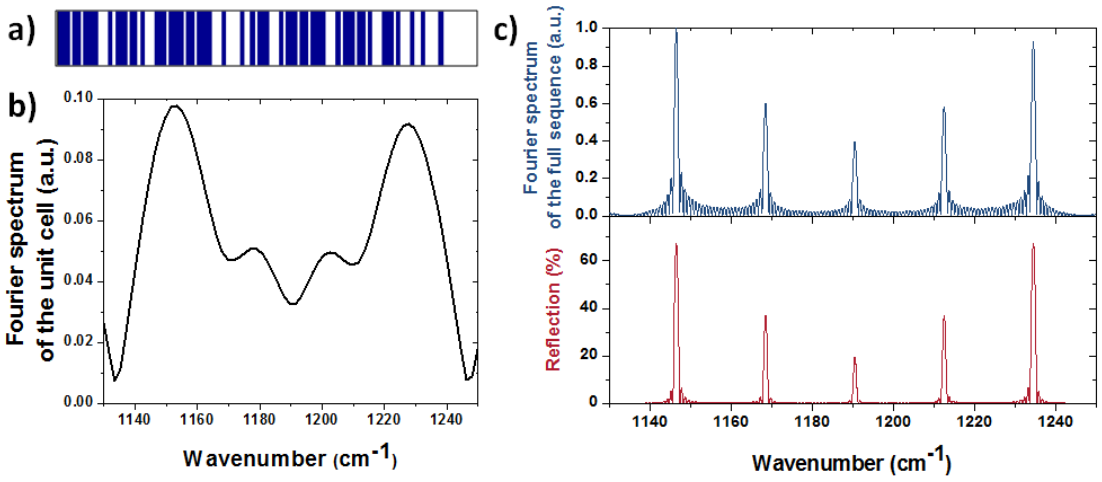

FIGURE 3.6: (a) Schematic of the spatial refractive index profile of the unit cell. Blue bars represent low index layers. (b) Fourier transform of the unit cell. (c) Fourier transform (blue), and reflection spectrum (red) computed with a transfer matrix code for a one dimensional stack of low (3.16) and high (3.18) index layers, for the full GAB sequence consisting of 25 repetition of the unit cell shown in (a). The x-axis for the Fourier spectra are scaled by 2 to take into account the fact that lasing occur at the wavelengths such that $1/\lambda = k_{grating}/2$, where $k_{grating}$ are the wavenumbers of the Fourier spectra peaks.

chose a unit cell based on a Rudin-Shapiro (RS) aperiodic sequence. The RS sequence is notable because its Fourier spectra is absolutely continuous, which makes it akin to purely random series. The RS sequence is a deterministic aperiodic sequence that can be generated in a two-letter alphabet by iteration of this inflation rule [48–51]: AA $\rightarrow$ AAAB, AB $\rightarrow$ AABA, BA $\rightarrow$ BBAB, BB $\rightarrow$ BBBA. In the case of gratings, this two letter alphabet can be transcribed into a sequence of low and high refractive index layers (e.g. A for low index, B for high index). A two-dimensional RS array was used in [52] to demonstrate laser action in a pseudo-random medium.

We designed a grating for operation on five distinct wavelengths. The unit cell is composed of 108 quarter-wave layers in a sequence given by the sixth generation RS sequence

(128 elements) where we removed the last 20 elements. This truncation shortened the superperiod and increased accordingly the spacing between the Fourier peaks, so as to fit exactly five peaks within the gain spectrum of the laser. The unit cell is repeated 25 times to form the superlattice. The number of repetitions of the unit cell was chosen so that the total length of the grating is about 2.5 mm. The quarter-wave layers are defined with respect to a central wavelength $\lambda = 8.4\mu$m. The precise sequence of the unit cell is given below and is also represented in figure 3.6 (a):

H=high index, L=low index; 25 repetitions of (HHHLHHLHHHH-
LLLHLHHHLHHLHLLLHHHLHHHHLHHLHHHHLLLHLLLLHLLHLHHH-
LLLHLHHHLHHLHHHHLLHLHHHLHHLHLLLHHHLHLLLHLLHLLLLH)

Figure 3.6 (b) and (c) show the Fourier transforms of respectively the unit cell and the full grating, together with a transfer-matrix (T-matrix) calculation of the reflection spectrum (red), computed using a commercial T-matrix code (Film Wizard), of a one dimensional dielectric stack of quarter-wavelength layers with refractive index 3.16 and 3.18, arranged in the same sequence as the grating we designed. We estimated the effective index of the etched and not-etched layers using finite-element simulations (COMSOL Multiphysics). At the positions of high amplitude Fourier components, we observe sharp peaks in reflectivity marking the opening of a bandgap.

The amplitude of the five Fourier peaks was designed to compensate for the finite linewidth of the gain, in order to obtain a flat net gain. In other words, we compensated

for the higher gain experienced by the central wavelength by reducing the amplitude of the corresponding Fourier component and thus the reflectivity.

The grating was fabricated as a buried grating on bound-to-continuum QCLs designed for operation at $\lambda = 8.4\mu$m. The QCL wafer used in this work was grown by MOCVD on conducting InP:S substrate [53]. The lower cladding structure consists of a thick InP layer (InP:Si, $n = 1\text{x}10^{17}\text{cm}^{-1}$, $d = 3.5\mu$m), a grading layer (InGaAsP:Si, $n = 1\text{x}10^{17}\text{cm}^{-1}$, $d = 300\mathring{A}$) and an InGaAs layer (InGaAs:Si, $n = 3\text{x}10^{16}\text{cm}^{-1}$, $d = 5200\mathring{A}$). The active region grown on top of the lower cladding is similar in design to the one described in [54]. It is composed of 35 repetitions of the following sequence:

13/47/**12**/52/**11**/53/**9**/17/**44**/25/**36**/27/**32**/<u>27</u>/<u>**25**</u>/<u>28</u> /**21**/31/**18**/34/**16**/39/**15**/42,

where the AlInAs barriers are in bold and the n-doped ($4.9\text{x}10^{16}\text{cm}^{-1}$) layers are underlined. The thicknesses are given in Angströms. The upper cladding grown on the active region is symmetric to the lower cladding with respect to the active region. The structure is finally capped with a highly doped InP layer (InP:Si, $n = 5\text{x}10^{18}\text{cm}^{-1}$, $d = 0.5\mu$m). Electroluminescence from very low quality factor (practically no feedback) mesa structures was measured, with a peak at 1190cm^{-1} and a full width at half maximum of about 250cm^{-1}. We used these values to adjust the design of the gratings.

Fabrication of the buried gratings is initiated by removal of the upper cladding down to the 520-nm-thick InGaAs layer by wet etching in an $\text{HCl} : \text{H}_2\text{O}$ (1:1) solution. Electron beam lithography and reactive ion etching to a depth of 300 nm were then used to define the gratings into the InGaAs layer. The same upper cladding as the original one was

then regrown on the structure to bury the grating. Laser ridges 20, 23 and 26-μm-wide were subsequently defined using reactive ion etching. Electrical passivation was achieved by depositing 450 nm of SiN using plasma-enhanced chemical vapor deposition. Top and bottom metallization consisted of Ti (15nm)/Au (450nm). The fabricated devices were cleaved to $\simeq$2.5 mm length, indium mounted on copper heat sinks and characterized in pulsed operation, with a pulse length of 100ns and a repetition rate of 20kHz.

In order to eliminate Fabry-Perot longitudinal modes, we deposited on the front facet of the lasers an anti-reflection (AR) coating composed of a bilayer of YF_3 and ZnSe [29]. After deposition, lasing was suppressed for Fabry-Perot lasers processed on the same chip as the devices with gratings.

3.3.5 Experimental results

The laser spectra at different bias of a typical device with a five-wavelength grating is presented in figure 3.7 (a). The spectra feature up to three simulatenous lasing peaks at room temperature. A blue-shift of the gain with increasing bias results in the suppression of the reddest peaks and the apparition of a third peak on the blue side for large bias (see figure 3.7 (a). We observe that the position of the lasing peaks is systematically red-shifted by about 0.5% compared to the calculated reflection peaks. This error can be attributed to our imperfect knowledge of the effective refractive indices of the layers. As explained above, the relative amplitude of the Fourier components of this grating was designed to compensate for the gain lineshape in order to obtain a flatter net gain.

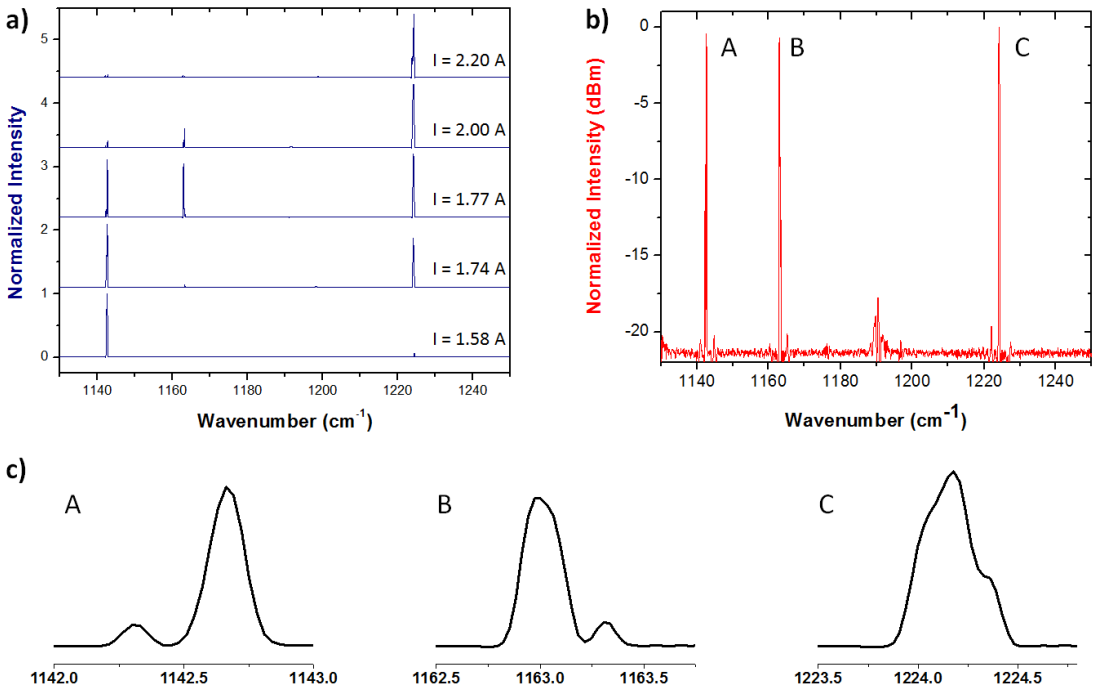

FIGURE 3.7: Experimental results for the five-wavelength grating design. (a) Lasing spectrum of a typical device with AR coating, 2.5-mm-long and 23-μm-wide, operated at room temperature in pulsed mode, with a repetition rate of 20kHz and pulse length of 100ns, at different currents. (b) Log scale plot of the central spectrum represented in (a) (I = 1.77 A). (c) Zoom-in spectra of the peaks A, B and C referenced in (b), in linear scale.

The fact that two of the central wavelengths never lase indicate that we under-estimated the gain linewidth in our calculations and overly favored the side wavelengths.

So far, we have left aside the question of why multi-mode lasing can be expected at all in QCLs. If the grating does provide five narrow regions with higher net gain, that does not necessarily mean that lasing has to occur in all five regions. On the contrary, basic laser theory suggests that once a first mode starts lasing, gain should be clamped, which in turn prevents any further mode to reach the lasing threshold. Multimode operation is possible in QCLs, because of their low threshold for spatial hole burning

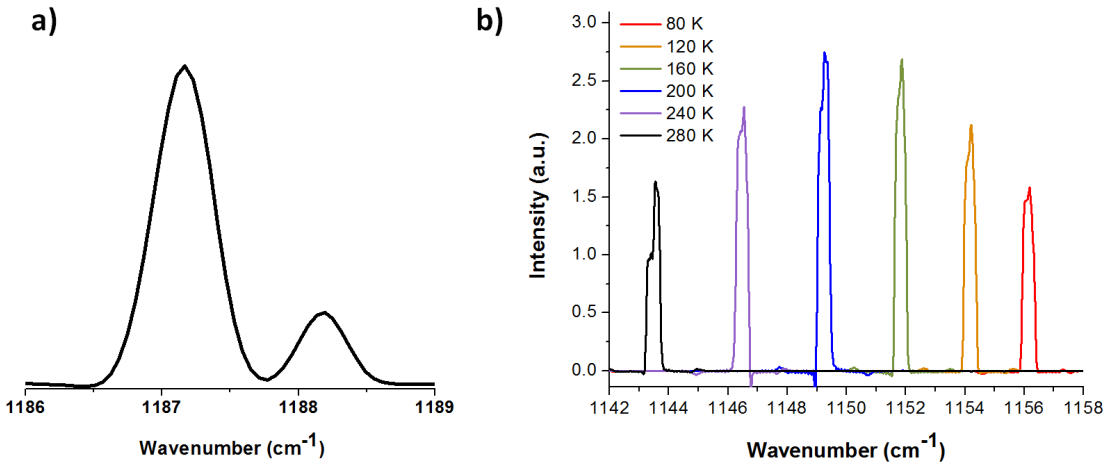

FIGURE 3.8: (a) Lasing spectrum of a DFB laser processed on the same chip as the GAB gratings studied here, operated in similar conditions. (b) Zoom-in on the peak A in figure 3.7 (b) at different temperatures, from 80K to 280K.

(SHB) instability [36]. This instability comes into play when the gain recovery time becomes comparable to or smaller than the carrier diffusion time, so that the gain grating created by the lasing mode longitudinal pattern is not washed out but persists, leaving regions of the waveguide where gain is available for other modes to start lasing. It is thus because of SHB that our devices feature several lasing modes. However, further study beyond the scope of this paper would be needed to quantify the role of the SHB instability in multi-wavelength QCLs and the impact of an AR coating on its threshold.

Figure 3.7 (b) shows a log scale plot of the central spectrum in figure 3.7 (a), on which a sidemode suppression ratio (SMSR) of 20dB is obtained for the three lasing modes. A central island of Fabry-Perot modes is observed, indicating a residual reflectivity of the AR coating and a relatively high net gain region stemming from the two other Fourier peaks that were expected to select two other single-mode wavelengths.

A closer look at each peak reveals that they are not rigorously single-mode (see figure 3.7 (c). Peaks A and B are doublets corresponding to the two band edges of the band gap. Measuring the spacing between the two band-edge modes enables to estimate the coupling coefficient κ, as it is a measure of the bandgap width. Following [55], we use $\kappa = \pi n_{av}.\Delta(k_{gap}) \simeq 5\text{cm}^{-1}$, where $n_{av} \simeq 3.17$ is the average effective index in the laser waveguide and $\Delta(k_{gap}) \simeq 0.5\text{cm}^{-1}$ (c.f. figure 3.7 (c). In comparison, we measured the coupling coefficient for DFB lasers fabricated on the same chip (Figure 3.8 (a). We obtain $\Delta(k_{gap}) \simeq 1\text{cm}^{-1}$ which corresponds to $\kappa \simeq 10\text{cm}^{-1}$. As expected the coupling coefficient for GABs is lower than for DFB lasers, but this is not an issue for QCLs as they are usually processed into long waveguides (typically 2 to 3 mm long). Peak C is composed of three peaks. The third peak probably corresponds to a higher order lateral mode, as the lasers were processed in relatively wide ridges (23-μm-wide).

We verified the temperature tuning performance of the GAB lasers by monitoring the position of the peak A in figure 3.7 (b) at regular temperature intervals from 80K up to room temperature. The results are shown in figure 3.8 (b). A continuous temperature tuning of 0.06 $\text{cm}^{-1}.K^{-1}$ is obtained. This is comparable to typical values obtained for QCLs operating in the long-wavelength infrared range (LWIR) [56].

3.3.6 Conclusion

We introduced *gratings with an aperiodic basis* (GABs) as a generalization of several existing approaches to design gratings having multiple selected spatial frequencies. The

use of aperiodic sequences opens a range of new possibility for the Fourier spectrum engineering of superstructure gratings. We used such gratings to provide distributed feedback and demonstrate simultaneous multi-wavelength lasing of mid-infrared quantum cascade lasers on up to three wavelengths having each a SSR of 20dB. More generally, the concept of GABs could find significant applications wherever multi-band reflectors are needed.

Chapter 4

Mode switching in a multi-wavelength distributed feedback quantum cascade laser using an external micro-cavity

In this chapter, we demonstrate a multi-wavelength distributed feedback (DFB) quantum cascade laser (QCL) operating in a lensless external micro-cavity and achieve switchable single-mode emission at three distinct wavelengths selected by the DFB grating, each with a side-mode suppression ratio larger than 30 dB. Discrete wavelength tuning is achieved by modulating the feedback experienced by each mode of the multi-wavelength DFB QCL through a variation of the external cavity length. This method also provides

a post-fabrication control of the lasing modes to correct for fabrication inhomogeneities, in particular related to the cleaved facets position.

4.1 Motivation

In the multi-wavelength QCL presented in the previous chapter as well as in regular DFB QCLs, the output power and the selection of the actual lasing mode is sensitive to the phase of the radiation reflected from the uncoated end facets relative to the phase of the DFB mode [23]. This reduces fabrication yield and reproducibility. While anti-reflection coatings have been employed for QCLs to mitigate these problems [23], their use for broadband QCLs is limited by the availability of IR-transparent materials and long-term reliability issues. In multi-wavelength DFBs, the effect of the facet feedback is amplified by gain competition between the different grating modes.

Here, we use an external mirror positioned close to the back facet of the laser to modulate the feedback experienced by each mode and provide a post-fabrication control over the lasing modes. The effect of the small feedback modulation is amplified by gain competition, leading to a switching behavior between the individual grating modes of a multimode DFB QCL. By controlling the position of the external mirror, different modes or subsets of modes can be selected, with excellent extinction ratio. Our external micro-cavity QCL is free of any collimation optics and thus compact and easy to align.

4.2 Description of the experiment

The QCL active region used for this work is a broadband bound-to-continuum design [54] operating around 8.4 μm. It was grown by organometallic chemical vapor deposition on a conducting InP substrate [53]. Details on the grown layers and fabrication steps can be found in [7]. The fabricated laser ridges (20, 23 and 26-μm-wide) were cleaved to a length of 2.5 mm and indium mounted epi-side up on copper heat sinks. The QCLs are operated in pulsed mode at a repetition frequency of 20 kHz with a pulse duration of 50 ns.

Two types of gratings were fabricated. As a reference, we used a standard first-order single-mode DFB grating designed for operation at 1185 cm^{-1}. For multi-mode operation, we used a DFB grating with an aperiodic basis [7], providing distributed feedback for five equidistant modes separated by ≈ 20 cm^{-1} within the gain region of the material. Details on the grating sequence can be found in [7].

A microscale external cavity is formed by a gold mirror mounted on a piezo-stepper, and initially positioned almost in contact with the uncoated laser back facet. A schematic of the setup is shown in inset of Fig. 4.1 (a). During the experiment, the emission spectra of the QCLs were measured using a Fourier transform infrared spectrometer, while scanning the mirror position in sub-micrometer steps from a facet distance of less than 1 μm to about 0.9 mm. For each mirror position the driving current was swept from threshold to rollover (maximum output power), resulting in a full parameter map

of the devices performance. The output power was measured by a calibrated powermeter during a second parameter sweep.

4.3 External feedback for a single-mode QCL

Figures 4.1 (a) and (b) show the dependence of the peak power of a single-mode DFB with the mirror position. For short cavities, the modulation of the output power can be understood by treating the external cavity like a lossy Gires-Tournois (GT) etalon, where the high cavity losses stem from the large divergence of the uncollimated QCL output. When the DFB wavelength is on resonance with the lossy GT cavity, the power is efficiently coupled into the cavity. This results in a low effective reflectivity of the back facet - gold mirror system since the power is dissipated inside the external cavity, leading to a high threshold and a low peak power. Such resonant condition is reached whenever the external cavity length is an integer multiple of half the DFB wavelength, hence the 4.2 μm periodicity of the modulation. In Fig. 4.1 (b), showing a zoom-in on the first few modulation periods, we observe sharp dips in peak power (and sharp peaks in threshold current) corresponding to these lossy resonances. From the width of the first dip, we estimate a quality factor of 6.

As the external cavity length is increased beyond the Rayleigh length of the uncollimated output beam, the finesse of the GT etalon drops rapidly, since less power is reinjected into the laser waveguide. For a mirror distance of 100 μm, about 1% of the power emitted by the back facet actually hit the device facet after one round trip (see Appendix B). The

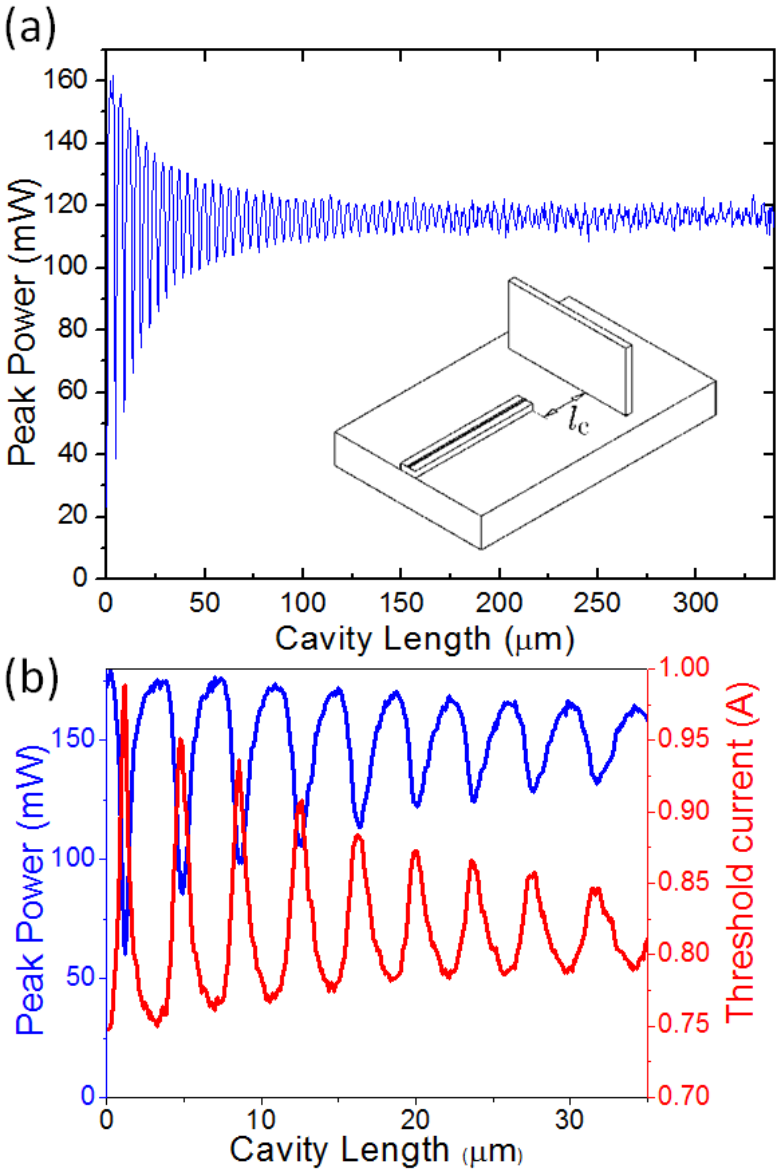

FIGURE 4.1: (a) Measured modulation of the peak power of a single-mode DFB QCL with the external cavity length. Inset: Schematic of the experimental setup, with a laser bar mounted on a copper submount and a gold coated mirror in front of the uncoated back facet. The cavity length l_c is controlled by a piezo stepper. (b) Peak power and threshold current for short cavity lengths ($0 < l_c < 30\mu$m).

peak power dips become accordingly broader. Eventually, when multiple reflections in the external cavity can be neglected, the peak power and current threshold modulations have a sine wave shape resulting from the interference between the back facet reflection and the small reinjected reflection from the external mirror. In this weak-coupling regime the output power modulation is less than 10%.

4.4 External feedback for a multi-mode QCL

Figure 4.2 shows the experimental results obtained for the multi-wavelength DFB. The black curve in Fig. 4.2 (a) shows the spectrum of the original laser (without external feedback). While five Fourier peaks were designed to fall within the gain bandwidth, with their amplitude adjusted in an effort to reach a flat net gain for all five modes [7], only four wavelengths are lasing simultaneously on this particular device, with one mode at ≈ 1205 cm^{-1} being significantly less powerful than the others. The number and subset of modes lasing simultaneously varies with drive current and from device to device, with a strong influence of the facet cleave position, as discussed later in the text.

With the introduction of the external mirror, each mode of this multi-wavelength DFB experiences an effective feedback from the composite system formed by the back cleaved facet and the external cavity. This feedback is modulated periodically as the external cavity length varies, with a period of $\lambda_i/2$, where λ_i is the wavelength of each mode. Corresponding oscillations in power output can be observed on Fig. 4.2 (b) and (c). Interestingly, we note that even though the feedback provided by the external mirror is

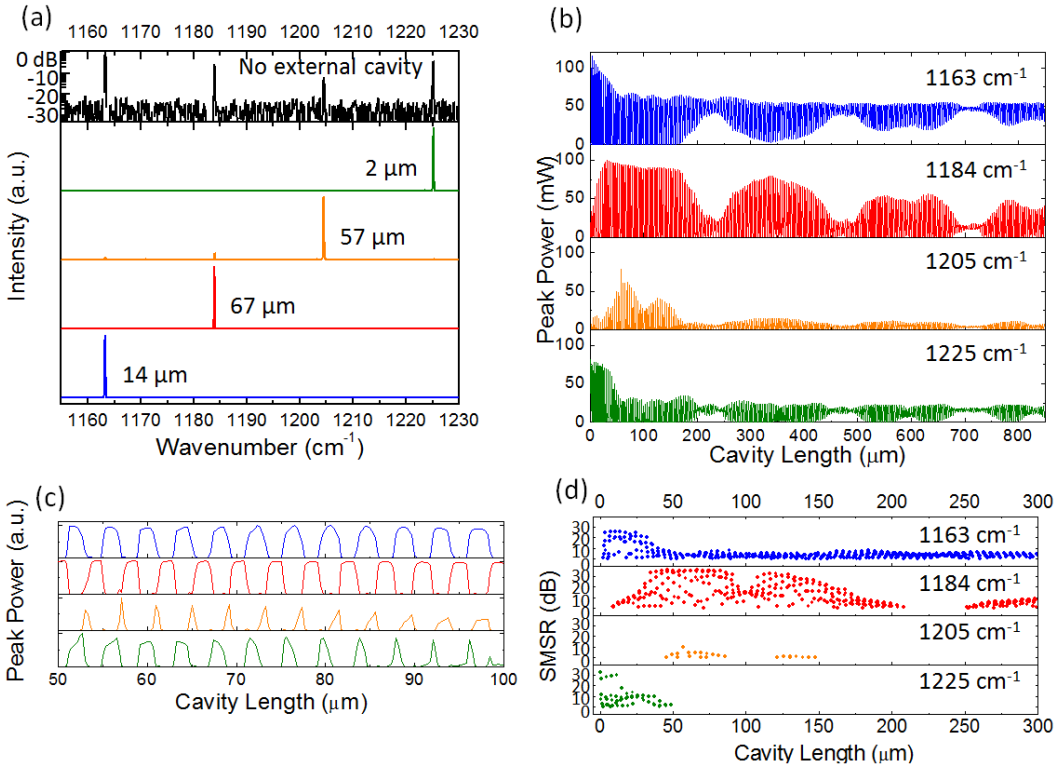

FIGURE 4.2: (a) Spectra of the multi-wavelength DFB QCL. From top to bottom: original laser (no external cavity)(black - log scale), laser with external cavity length $l_c = 2$ μm (green), $l_c = 57$ μm (orange), $l_c = 67$ μm (red) and $l_c = 14$ μm (blue). (b) Intensity modulation for the four lasing DFB modes with varying cavity length. The peak power values are obtained from the measured spectral intensity of the four modes. (c) Zoom-in of the modulation shown in Fig. 4.2 (b), for external cavity length between 50 μm and 100 μm. The traces are normalized to emphasize the modulation depth for each mode. (d) Measured side-mode suppression ratio for the dominant mode at each mirror position.

very small ($R < 1\%$ for a cavity length of 100 μm and more), the observed intensity modulations are very deep, periodically switching off most modes. This is due to the fact that a small feedback difference can modify the competition between the DFB modes, resulting in one or two modes suppressing all the others. Such amplification of the modulation depth by mode competition is also responsible for the persistence of the modulation for larger cavity length close to 1 mm, where the feedback from the external mirror is very weak ($R < 0.1\%$). As seen in Fig. 4.2 (a), this results in

true single-mode operation of the device at certain mirror positions. The wavelength of single-mode operation can be switched between the individual modes of the multi-mode DFB grating by varying the external cavity length.

To evaluate the mode selection capability, we find the most powerful mode at every mirror position, and calculate its side-mode suppression ratio (SMSR). Results are shown in Fig. 4.2 (d). While multi-mode operation (SMSR $\prec$ 10dB) is observed at a large number of mirror positions, the system features single-mode operation at certain cavity lengths for three of the DFB modes, with a SMSR larger than 30 dB. For the mode around 1205 cm^{-1}, true single-mode operation could not be achieved due to a persistent lasing of the modes at 1184 cm^{-1} and 1163 cm^{-1}. As seen from the spectrum recorded without an external cavity at the same driving current (Fig. 4.1 (a)), the mode at 1205 cm^{-1} is the weakest mode without feedback.

We also note that there is a beat pattern in the modulation amplitude. Individual modes λ_i experience comparable feedback at mirror positions fulfilling $l_c \approx m_i\lambda_i/2$, where m_i are integers. Certain mirror positions fulfill the above condition for all wavelengths simultaneously, and slightly moving the mirror away from this position affects all of the modes equally. As a consequence, the influence of the external mirror on mode competition drops around these points and the modulation amplitude decreases accordingly.

4.5 Simulation results

In order to gain insight into the behavior of the multi-wavelength laser, with and without external cavity, we used a linear model with gain first described by Ebeling and Coldren [57] (see Appendix B for further details). The system is described by a transfer matrix and by solving an equation translating a self-oscillating condition, we obtain the longitudinal modes of the laser and their respective thresholds. We can thus theoretically study the evolution of the lasing threshold for the five DFB modes of interest, as the cleaved facet positions or the external cavity length are varied.

Theoretical results on the influence of the cleave position (without external feedback) are shown in Fig. 4.3. The curves are normalized so that the five modes have the same threshold when the waveguide is cleaved exactly at the interface between two unit cells (i.e. no additional layer, as defined in Fig. 4.3 (a)). This assumes perfect design of the grating so that all five modes experience the same net gain. According to the simulations, the threshold gain varies drastically with the cleave position (close to 10% in modulation amplitude), with very different profiles for the five modes of interest. The pattern repeats approximately periodically for added layer thickness spaced by $\approx \lambda/2n$, where n is the refractive index of the added layer (QCL waveguide material, $n = 3.18$ assumed here). Only the first period is shown in Fig. 4.3. The differences in the threshold dependence between the modes as well as the observed symmetries are related to the grating unit cell design. The equality in threshold between the five modes, as assumed for a perfect cleave position at the unit cell interface, degrades rapidly within 200 nm of additional

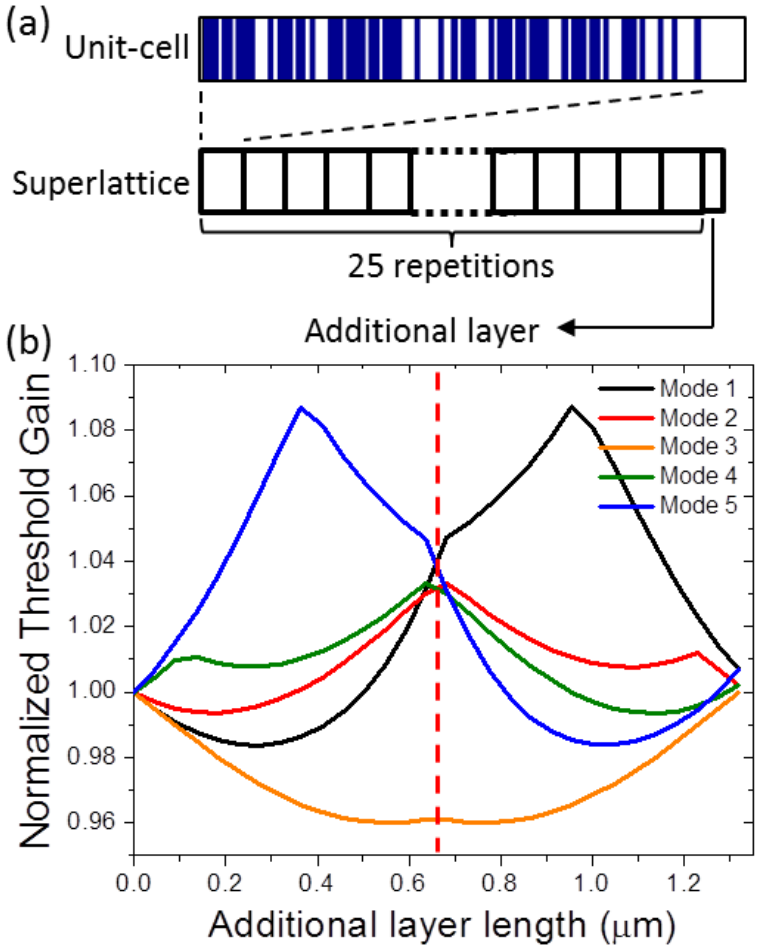

FIGURE 4.3: (a) Schematic of the simulated DFB structure, with 25 repetitions of the unit cell, itself composed of 108 quarter layers with refractive index 3.16 or 3.18, arranged according to a Rudin-Shapiro sequence. An additional layer with refractive index 3.18 is included at the end of the designed grating to account for the cleave position uncertainty. (b) Calculated threshold gain, normalized so that all modes have identical threshold when no additional layer is present. The red vertical line indicates the layer thickness (660 nm) for which multiwavelength lasing is the least likely, used for the results shown in Fig. 4.4 (d).

layer thickness. Assuming a random cleave position with uniform probability, we can thus estimate that only $\approx 15\%$ of lasers will lase simultaneously on more than three modes. Note that this is only a rough estimate, since it is not precisely known what threshold gain difference can be overcome by spatial hole burning and other instabilities or nonlinearities in the laser waveguide, in order to achieve multi-mode operation. The fact that the laser chosen here operates simultaneously on four modes without external feedback indicates that for this particular laser, the waveguide was cleaved close to an optimal position.

We then included the external mirror in the linear model. Results of the simulations are shown in Fig. 4.4. The experimental observations are well reproduced: for each mode with wavelength λ_i, the threshold is modulated with a period of $\lambda_i/2$. Two regimes can be distinguished: at short external cavity length (see Fig. 4.4 (b)), the threshold gain features sharp peaks, revealing the feedback drop whenever a mode wavelength is on resonance with the lossy external cavity. As the quality factor of the lossy GT etalon decreases, the modulation approaches the shape of a sine wave (see Fig. 4.4 (c)), characteristic of a simple interference between the light reflected by the laser back facet and the light reflected by the external mirror and reinjected into the waveguide. Assuming waveguide losses of 10 cm^{-1}, we obtain a threshold gain modulation by up to 50% in the strong feedback regime, and of $\approx 3.5\%$ around $l_c = 250$ μm. The experimentally observed beat pattern is also reproduced: the feedback modulation is in phase for the different modes for $l_c = 225$ μm (see Fig. 4.4 (c)), in agreement with the experiment.

For the results shown on Fig. 4.4 (a)-(c), the positions of the facets are assumed to be

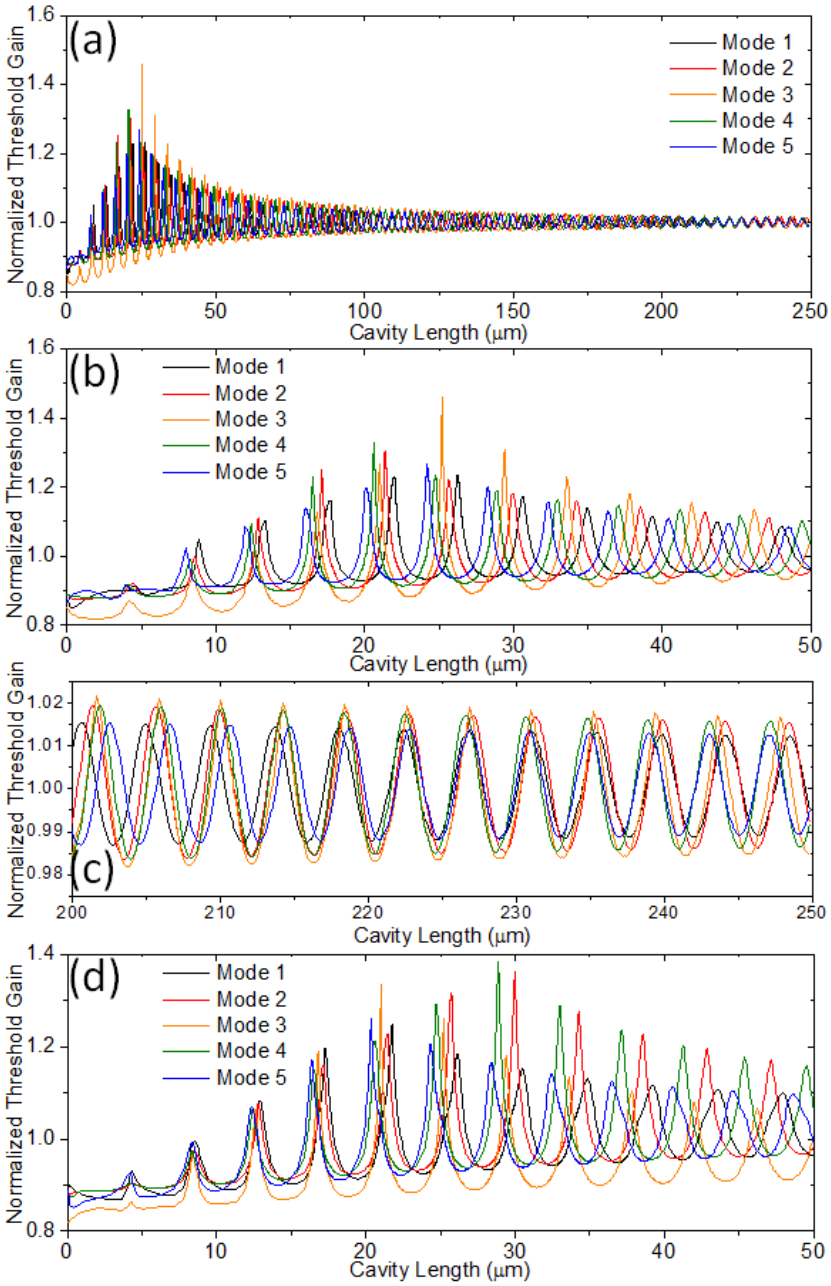

FIGURE 4.4: Calculated threshold gain for different external cavity length l_c, normalized so that all five modes have identical threshold when no additional layer and no external cavity are present. (a)-(c) No additional layer is included (perfect cleave position). (d) With a 660 nm-thick additional layer added at the end of the laser waveguide, corresponding to the red line in Fig. 4.3 (b).

perfect, i.e. exactly at the end of the designed grating. This is a realistic choice for the measured device since it originally lases on four modes, indicating a close to optimal cleave position. However, as discussed earlier, the cleave position will statistically be less optimal in most samples. In order to investigate the susceptibility of the observed effects to this parameter, we calculated the variations in threshold gain for the five DFB modes of interest in the case of a 660 nm-thick additional layer, which corresponds to the least favorable situation for multi-wavelength lasing (without external cavity), as indicated by Fig. 4.3 (b) (vertical dashed red line). In such conditions, the original laser is expected to lase on a single-mode (referenced as mode 3 in Figs. 4.3 and 4.4). With the external cavity, this mode still has the lowest threshold for most mirror positions. However, for certain mirror positions within the plotted range (0 to 50 μm), modes 1 and 5 show the lowest threshold, increasing the potential for single-mode operation on these modes. These positions are in the vicinity of the GT resonances for mode 3, where this mode experiences less feedback from the composite back facet.

4.6 Conclusion

In conclusion, we have demonstrated switching between individual wavelengths of a multi-wavelength DFB QCL by means of feedback from a short external lensless microcavity. We rely on gain competition between the individual DFB modes in order to achieve a 100% intensity modulation for each mode. The concept is robust against fabrication uncertainties such as the precise position of the cleaved facet and can offer

a post-fabrication laser mode control. The switchable multi-wavelength QCL demonstrated here is suitable as a source for selected spectroscopic applications which require wavelength tuning in the vicinity of several well-defined frequencies in order to identify a chemical compound.

Chapter 5

Double-waveguide quantum cascade laser for broadband emission

5.1 Motivation

We present in this chapter a waveguide structure designed to obtain broad and bright emission from a single monolithic device by growing two full QCLs, each with its own optical waveguide, on top of each other. Contrary to previous works using indium phosphide (InP) inter-stacks in a QCL structure [58, 59], the thick InP spacer used in this work to separate the active regions of the two QCLs is intended to create two uncoupled optical waveguides. We demonstrate excellent room temperature performance

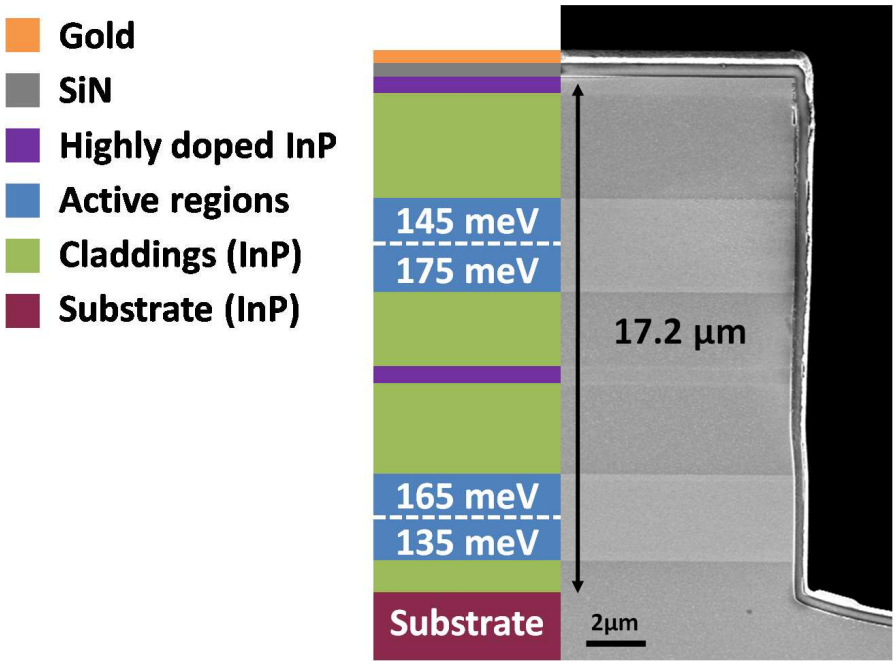

FIGURE 5.1: Schematic of the waveguide structure and scanning electron microscope (SEM) image.

from this device grown by metal-organic chemical vapor deposition [53] (MOCVD). The ability to grow thick QCL structures by MOCVD is particularly interesting for industrial production prospects since the growth of such complex structures in a single growth run can significantly reduce manufacturing costs. The device demonstrated here offers the advantages of a small footprint in addition to a small and reliable spacing between active regions, enabling to obtain good beam quality, for example using a microlens array.

5.2 Design of a double-waveguide QCL

In order to maximize the spectral coverage of the device, we distribute four different cascade designs over the two gain media (see Fig. 5.1). All cascades are based on a

bound-to-continuum design [18], characterized by an inherently broad gain spectrum, respectively centered at 135, 145, 165 and 175 meV, (in wavenumbers: 1089, 1170, 1331 and 1411 cm^{-1}). In order to reduce gain competition [60], which increases with increasing overlap of the gain curves, spectrally adjacent active regions were separated from each other. The number of stages for each wavelength was adjusted in an attempt to obtain a flat net gain spectrum. The layer sequence of the structure is described below:

InP (1.5μm, 5.10^{16} cm^{-3})/InGaAs (300nm, n_1=3.10^{16} cm^{-3})/first active region (22 cascades at λ=9.12μm and 15 cascades at λ=7.05μm)/InGaAs (300nm, n_1)/InP (3μm, 3.10^{16} cm^{-3})/InP (500nm, 1.10^{19} cm^{-3})/ InP (2.5μm, 3.10^{16} cm^{-3})/InGaAs (200nm, n_1)/second active region (20 cascades at λ=6.33μm and 19 cascades at λ=7.95μm)/InGaAs (300nm, n_1)/InP (1.5μm, 5.10^{16} cm^{-3})/InP (2μm, 1.10^{17} cm^{-3})/InP (500nm, 1.10^{19} cm^{-3})/InGaAs (20nm, 1.10^{19} cm^{-3}).

A low doping is used for the layers next to the gain media, in order to reduce free-carrier absorption. We reduce the coupling between the two waveguides, first by having a thick cladding between them and second, by inserting a highly doped plasmon layer to attenuate the far-reaching evanescent tails.

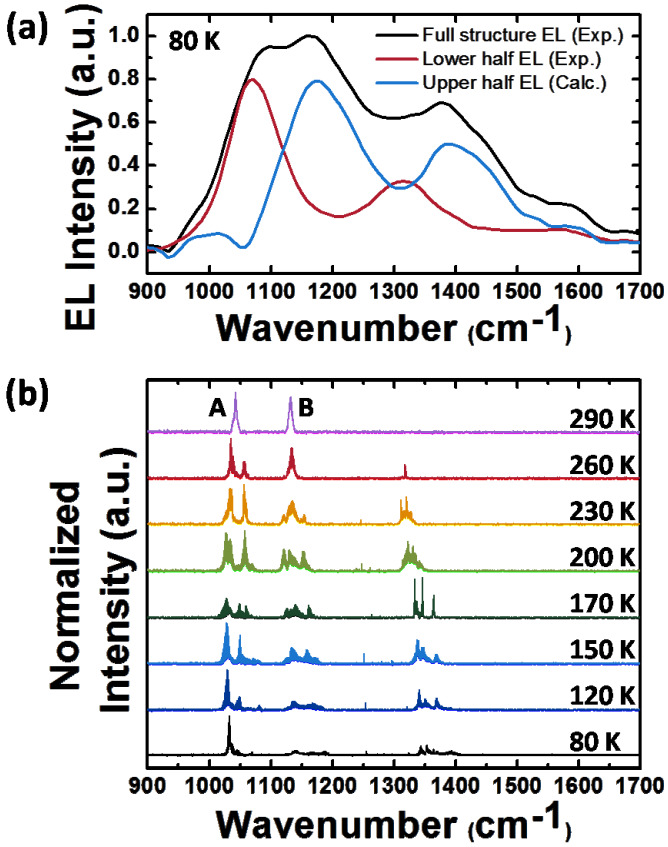

FIGURE 5.2: (a) Measured electro-luminescence (EL) spectra at 80 K from the full double-waveguide structure (black) and from the lower waveguide only (red), with upper waveguide etched away. (blue): Calculated difference of the two spectra as an approximation of the EL from the upper waveguide only. The measured spectra are taken for two cleaved mesas of similar sizes with similar current ($\simeq$ 1.4 A) flowing through them. The corresponding bias for the full structure is $\simeq$20 V, comparable to the 19 V bias used for the lasing spectra in (b). EL is shown at 80 K for direct comparison with the lasing spectrum at 80 K. (b) Lasing spectra at different temperatures for a 23 μm wide and 3 mm long laser, operated in pulsed mode (100 ns, 20 kHz). The laser is driven at a constant bias of 19 V (current $\simeq$ 2 A). A high-reflectivity coating was deposited on the back facet of the laser. The letters A and B allow identification of the two groups of modes.

5.3 Experimental results

Round mesas with a 200 μm diameter were processed for the measurement of the electroluminescence (EL) spectra. A broad EL spectrum spanning 1025 to 1475 cm^{-1} is obtained for the full double-waveguide structure, as shown in Fig. 5.2 (a). We etched away the upper waveguide, down to the middle of the spacer separating the two waveguides, and reprocessed some mesas in order to measure the EL from the lower waveguide only. From the difference between the spectrum measured for the full structure and the lower waveguide only, we deduced the spectrum for the EL of the upper waveguide only. We observe two EL peaks for each waveguide, at 1070 cm^{-1} and 1310 cm^{-1} for the lower one (measured), and at 1170 cm^{-1} and 1390 cm^{-1} for the upper one (calculated). For both waveguides, the long-wavelength peak is about twice as strong as the short-wavelength peak. We believe that this can be explained by resonant cross-absorption of the short wavelengths in the long-wavelength stages, resulting in a significantly lower net gain at short wavelengths. We identified two transitions that can lead to a strong absorption of the short wavelength. One is from the upper lasing state to a high energy state in the active region quantum wells, close to the continuum. The second is from the lower laser level to the state above the upper laser level. While gathering spectrally adjacent stages in the same waveguide could reduce cross-absorption, it would increase gain competition. For this reason, cross-absorption would be better addressed with a careful design of the stages. In future work, we will focus on improving the designs of the individual active regions, in particular by implementing innovative solutions for broadband lasing [29]. The combination of these proven broadband designs [19, 20, 29]

with our double-waveguide QCL approach is a straightforward path towards monolithic QCL sources with unprecedented lasing bandwidth.

Fabrication of the lasers started with the etching of 17 μm-deep trenches by reactive ion etching (RIE) using a photolithography-defined SU8 mask. The side-walls remain straight and smooth over the whole depth, as seen on Fig. 5.1. The trenches defined waveguides 20, 23 and 26 μm-wide. A 300nm-thick SiN insulation layer was then deposited by plasma-enhanced chemical vapor deposition and opened by RIE on top of the laser ridges. Top and bottom metallization consisted of Ti(15 nm) and Au(450 nm) layers. The fabricated devices were cleaved to 3 mm length, high-reflection coated (Al_2O_3/Au) on the back facet and indium mounted epi-side up on copper heat sinks. The devices were characterized in pulsed operation with 100 ns pulse width and 20 kHz repetition rate.

Fig. 5.2 (b) shows lasing spectra obtained at different operating temperatures. Up to 260 K, a temperature that can be reached with thermoelectric coolers, we can distinguish three main islands of Fabry-Perot modes, with lasing modes separated by up to 360 cm^{-1}. For temperatures above 260 K, only the two long-wavelength islands survive. They are positioned where maximum luminescence is observed (see Fig. 5.2 (a)). We note that for lasers processed from a piece of wafer containing only the lower active region, only the group of modes A is lasing. Together with the luminescence data, this indicates that the group of modes B is lasing mainly in the upper waveguide where it experiences the most gain, whereas the group of modes A is lasing mainly in the lower waveguide.

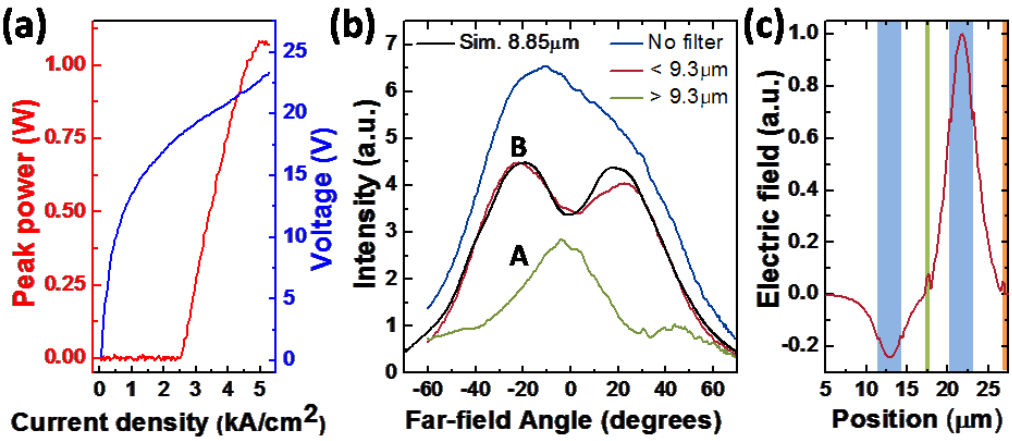

FIGURE 5.3: (a) Light intensity (peak power) (red) and voltage (blue) versus current density for a representative device (with high-reflectivity coating) operated in pulsed mode (100 ns, 20 kHz) at room temperature. (b) Far-field of the representative device of Fig. 5.2 (b), operated in the same conditions. In blue, without filter, in red, with a short-pass filter at 9.3 μm. In green, the calculated difference of the two previous curves (blue minus red), illustrating the far-field of modes A. In black, simulated far-field of the linear combination of the two lowest-order orthogonal TM waveguide modes fitting best to the experimental data. The simulations are done at the central wavelength of the group of modes B (8.85 μm). The far-fields are measured by scanning a mercury-cadmium-telluride detector located 10 cm away from the laser, along a direction perpendicular to the growth planes. (c) Instantaneous electric field (at a time maximizing field amplitude) across the structure, along the direction perpendicular to the layer planes. The two active regions are in light blue, the central plasmon layer in green and the top gold contact in yellow.

The light-current-voltage characteristics shown in Fig. 5.3 (a) demonstrate good lasing performance from both gain media, at room temperature and in pulsed operation (100 ns/20 kHz). Using a short-pass filter at 9.3 μm (between the group of modes A and B), we observed that the threshold is the same for both groups of modes and that the power is approximately equally divided between them. This indicates that both waveguides have comparable optical losses. Remarkably, the good performance of the device, in particular of the group of modes B for which gain is provided by the last stages grown, indicates that high quality growth can be sustained for such thick structure and that

our waveguide design maintains low optical losses.

To investigate optical coupling between the two waveguides, we measured the far-field of a representative laser operated at room-temperature. Fig. 5.3 (b) shows line-scans along the direction perpendicular to the layer planes. We observe that the emission of the group of modes B features two peaks separated by a shallow dip. Using finite-difference simulations (Lumerical FDTD), we solved for the two lowest-order orthogonal TM modes supported by the double-waveguide structure. We then computed the far-fields (obtained by near-field to far-field transformations) of linear combinations of these two modes in order to identify the superposition corresponding best to the experimental far-field. The best fit is shown in black in Fig. 5.3 (b), and the corresponding mode profile is shown in Fig. 5.3 (c). The intensity is mostly confined to the upper waveguide, with only about 6% of the power in the lower waveguide. The two lobes of the electric field in the two waveguides are π-shifted one with respect to the other. Lasing on such mode is favored as it corresponds to a minimum of field at the center of the spacer region where we introduced a highly doped lossy layer. A thicker highly-doped layer with a larger doping level between the two active regions could easily reduce the coupling between the two waveguides. In contrast, the far-field calculated for the group of modes A indicates that light is emitted mainly from one waveguide, the lower waveguide in our case.

5.4 Conclusion

In summary, we have presented a double-waveguide QCL design. This small-footprint design provides flexibility to distribute multiple QCL stages over two weakly-coupled optical waveguides, in order to obtain broadband emission while dealing with common issues of heterocascade QCLs, such as cross-absorption and gain competition. We demonstrated that good room temperature performance is preserved with this very thick device grown by MOCVD. Full decoupling of the waveguides was not achieved at all wavelengths but this can easily be accomplished by increasing the thickness and/or doping of the cladding layers. Furthermore, intentional coupling of the two waveguides can be explored to obtain beam-steering of the laser emission. Our design also opens the route to more complex three-terminal devices by using the highly doped plasmon layer separating the two waveguides as a third contact.

Part II

Wavefront engineering of QCLs

Chapter 6

Introduction to plasmonic collimators

6.1 Motivation

Semiconductor lasers are the key components in many widespread commercial technologies such as optical fiber communications and compact disk/digital video disk players. They are also accelerating the development of many other technological fields, including 3-D display technology, quantum information, and medical imaging. However, the output beams of semiconductor lasers have their own problems. In particular, the beams usually have a large divergence angle of around tens of degrees due to large diffraction caused by the small emission aperture of the devices [61].

Laser beam shaping (i.e., collimation, polarization control) is conventionally conducted externally using optical components such as lenses, beam-splitting polarizers, and wave plates [62]. These optical components are bulky and can be expensive; some are available only for certain wavelength ranges. Devices that have the desired beam characteristics intrinsically built-in to the active devices themselves would therefore be very interesting.

Our group demonstrated very small beam divergence in the laser polarization direction in $\lambda = 9.9$ μm QCLs by patterning a 1-D plasmonic grating on the device facet [63]. We then extended the idea to achieve complete collimation in the laser emission plane using 2-D plasmonic structures [64, 65]. It was shown in both situations that the beam divergence angles were greatly reduced, from tens of degrees for the original devices to just a few degrees for the devices integrated with plasmonic collimators. The fabricated devices preserve good room-temperature performance; the devices with an optimized design exhibit an output power that is comparable to that of the original unpatterned lasers.

A detailed account of our recent research on 1-D and 2-D plasmonic collimation for QCLs can be found in [10]. In these works, QCLs are chosen as a model system, but the design with proper adjustment should be applicable to diode lasers as well.

6.2 Plasmonic collimators

A basic physical understanding of plasmonic collimators is easily illustrated using the example of two-dimensional plasmonic collimators [65], consisting of a subwavelength

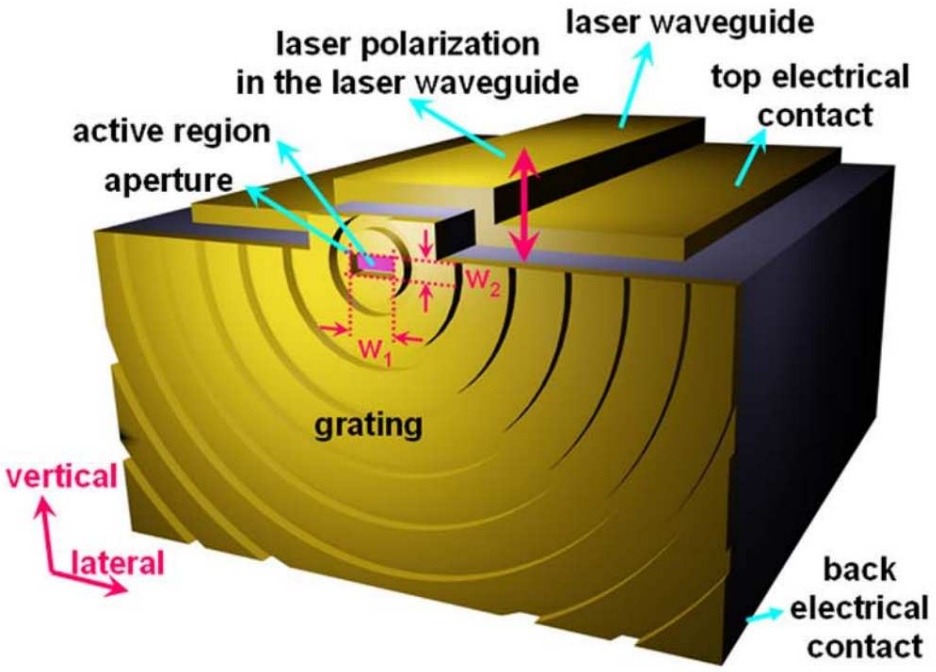

FIGURE 6.1: A sketch of the device, consisting of a QCL and a metallic aperture-grating structure defined on its facet.

aperture opened on the laser active region and an array of half rings centered on the aperture; see Fig. 6.1 for a sketch of the design. The rings are defined into a metallic coating initially deposited onto the laser facet. This metal layer supports plasmonic modes at the metal/air interface, providing a channel to transfer energy from the central aperture to the rings.

Beam collimation in the fabricated devices is essentially an interference effect: the aperture couples the laser output into surface plasmons (SPs) while the half-ring pattern functions as a 2D ensemble of scatterers that coherently radiate the energy of the SPs into the far field; radiation from the aperture and from the scattered SPs interfere constructively, leading to increased intensity in a small solid angle.

This concept is quite analogous to that of array antennas or Yagi-Uda antennas, whereby the fields emitted by a master antenna and an array of slave antenna all constructively interfere in a given direction, increasing the directionality of the system.

6.3 Non-symmetric plasmonic gratings

While working on the design of plasmonic collimators to shape increasingly complex beams, it became necessary to devise more complex grating patterns to act as secondary emitters.

In particular, one interesting future development would be to provide a means to beam the light output of a laser in different directions (beam steering). Having an integrated passive solution would open a path to active beam steering with no moving parts. Such off-axis collimation requires a pattern that does not have circular symmetry as in the case of the two-dimensional grating of [65].

Since the design of two-dimensional structures can be computationally intensive using standard simulation tools, such as finite-difference time-domain (FDTD) or finite-element methods (FEM), we had to devise a simple model to provide design rules. Such a model is presented in Chapter 7, along with experimental results obtained for off-axis plasmonic collimators. Multi-beam collimators are then designed and demonstrated, as shown in Chapter 8, providing a good example of the complex beams that can be achieved [11].

Chapter 7

Dipolar modeling of plasmonic collimators

7.1 Introduction

In recent years, plasmonics, the study of the coupling between electromagnetic fields and electronic oscillations at a metal-dielectric interface, has emerged as one of the most rapidly growing fields of optical physics [66]. Plasmonics has made it possible to move optics to the sub-wavelength scale, opening up a range of new opportunities in science and technology for communication, sensing, and imaging [67, 68]. However, for this vision to bear fruits, new components are needed that can act as interconnects between the nanoscale volumes involved in plasmonics and free-space optical elements. Such components would enable the design of complex optical systems where signal, pumps

or probes can be sent in and out of photonic waveguides, quantum dots or even single molecules.

The general problem of coupling a surface wave (SW) to free-space beams is usually addressed using one-dimensional (1D) gratings [63, 69–72]. Two-dimensional (2D) gratings obtained by simple rotation of a second-order 1D grating (also named *bull-eye* structures) were also devised to generate a collimated beam from a point-like source of SWs, or reversely to focus incident light into a nanoscale-size "hot spot" [65, 73–76]. Such structures are still 1D in a cylindrical coordinate system. However, designing truly novel 2D structures using standard simulation tools, such as finite-difference time-domain (FDTD) or finite-element methods (FEM), is made very difficult by the large size of the 3D simulations required, typically on the order of 10^7 to 10^8 mesh cells [77].

The essential physical phenomenon involved in a grating is the interference between the emissions of scatterers distributed along the surface, whether they are holes, particles, grooves or ridges. We introduce here a phenomenological model to calculate the far-field radiation pattern of any 2D grating, which approximates the field scattered by the grating as that of an ensemble of electric dipoles distributed on the surface. The simulation time is reduced to several minutes on a personal computer. While ray tracing models have already been used to describe two-dimensional focusing holographic gratings [78], our dipolar model is more versatile. In particular, by using a 'microscopic' description of the grating, it enables accurate modeling of complex structures with finite size and local parameters that can be varied at will (illumination intensity, scattering efficiency, losses, etc...).

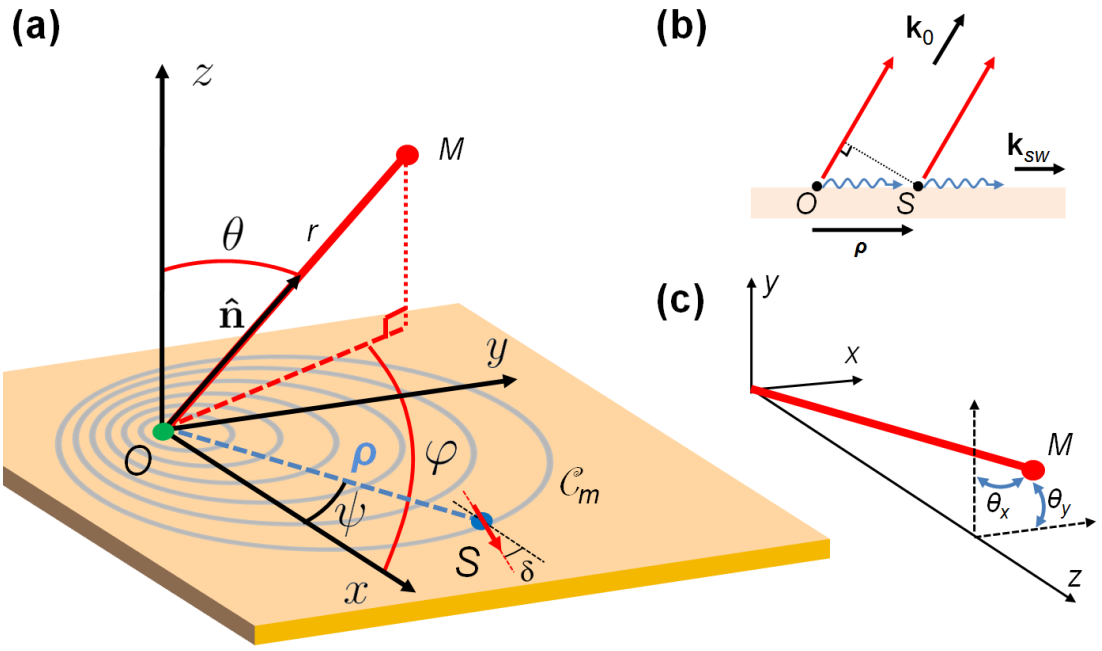

FIGURE 7.1: (a) Schematic of a plasmonic lens. (b) Interference between the field radiated by the source O and the field scattered by S. (c) Definition of the angle system (θ_x, θ_y).

7.2 Basics of the model

Let us consider a point source O that launches surface waves (SWs) along a corrugated metal-air interface, and an ensemble of point scatterers S lying on the lines $\mathcal{C}_m$ in the x-y plane (Figure 7.1(a)). A point source approximates well a source of sub-wavelength dimensions such as an aperture defined in the metallic film. This point source can often be modeled as a point dipole whose polarization imposes a particular angular distribution on the launched SWs [10]. The lines $\mathcal{C}_m$ describe the grooves of a generic 2D grating. We assume that each point S, with polar coordinates (ρ, ψ), scatters a portion of the SWs out of the plane, while the other portion keeps propagating along the surface. The radiation pattern of this system is obtained by summing over all scattered fields.

We assume that the field $\mathrm{d}\mathbf{E}_S(\mathbf{r})$ scattered by an infinitesimal portion of $\mathcal{C}_m$ around S, subtending an angle $\mathrm{d}\psi$, can be modeled by that of an electric dipole located at S, and having an amplitude proportional to the amplitude of the SW at that point, modulated by a scattering efficiency. The SW complex amplitude at S can be expressed as $a_S = f_1(\rho)f_2(\psi)\exp(ik_{sw}\rho)$, where $f_1(\rho)$ expresses the decay of the SWs as they propagate away from the source (due to diffraction, scattering, and absorption losses), and $f_2(\psi)$ is the angular distribution of the SWs launched at the point source. k_{sw} is the SW wavevector. For a point source polarized at an angle $\psi = \psi_s$, $f_2(\psi)$ can be expressed as $f_2(\psi) = cos(\psi - \psi_s)$ [10]. As the lines of scatterers represent grooves, the orientation of the dipole is taken in the x-y plane, normal to the groove. Qualitatively, this choice stems from the picture of an incident SW driving charge oscillations on one edge of the groove, which in turn triggers oscillations of image charges on the opposite edge, at the shortest distance and thus in the direction normal to the groove. Polarization sensitive experimental results will corroborate this assumption (c.f. Figure 8.2).

If $\hat{\boldsymbol{\delta}}$ is a unit vector which defines the orientation of the dipole, δ being the angle formed with the x-axis, one can write:

$$\mathrm{d}\mathbf{E}_S(\mathbf{r}) \propto a_S f_3(\delta - \psi)\frac{e^{i(k_0\hat{\mathbf{n}}\cdot(\mathbf{r}-\boldsymbol{\rho})+c_1)}}{r}[(\hat{\mathbf{n}} \times \hat{\boldsymbol{\delta}}) \times \hat{\mathbf{n}}]\mathrm{d}\psi \tag{7.1}$$

where $\hat{\mathbf{n}}$ is the unit vector in the direction OM. The source is assumed monochromatic, with a free-space wavelength $\lambda_0 = 2\pi/k_0$. We neglect the reflections of SWs at the grooves, which is a valid approximation except in the case of constructive interference

of the small reflections from each groove, which sets in when the grating period is about $m \cdot \lambda_{sw}/2$, where $m = 1, 2, 3, ...$ The groove scattering efficiency at S is denoted by $f_3(\delta - \psi)$. It depends on the direction of the incident SW relative to the groove, and on the groove depth and width. The phase shift introduced by the scattering event is c_1.

We emphasize that the input parameters of our model (f_1, f_3 and c_1), specific to a given groove geometry and working wavelength, can be readily determined through simple considerations and 2D simulations as we show thereafter for our particular structure. The simulations we use here require orders of magnitude less resources (in time and memory) than the 3D simulations one would need to perform to simulate the final device. Importantly, once these parameters have been evaluated, it is possible to study the response of all sorts of gratings by simply changing the equation of the curves $\mathcal{C}_m$, predicting not only the amplitude pattern but also the phase pattern of the radiated light.

7.3 Far-field radiation pattern

The expression of the total field is obtained by summing over the continuous distribution of scatterers S on the line $\mathcal{C}_m$, and over N lines. The radiated power density in the far-field is proportional to the angle-dependent component of $|\mathbf{E}(\mathbf{r})|^2$:

$$D(\theta, \varphi) \propto \left| \sum_{m=1}^{N} \int_0^{2\pi} e^{i\Delta\phi} f_1 f_2 f_3 \hat{\boldsymbol{e}}(\theta, \varphi, \delta) \mathrm{d}\psi \right|^2 \tag{7.2}$$

where $\hat{\boldsymbol{e}}(\theta, \varphi, \delta) = \cos(\theta)\cos(\delta - \varphi)\hat{\boldsymbol{\theta}} + \sin(\delta - \varphi)\hat{\boldsymbol{\phi}}$. $\Delta\phi$ is the phase difference between the field $\mathbf{E}_S$ scattered by S and the field $\mathbf{E}_0$ directly emitted from the source O, both evaluated at point M with spherical coordinates (r, θ, φ) in the far-field ($r \gg d \gg \lambda$, the grating dimensions being of order d). It is given by:

$$\Delta\phi = k_{sw}\hat{\mathbf{m}} \cdot \boldsymbol{\rho} - k_0\hat{\mathbf{n}} \cdot \boldsymbol{\rho} + c_1 \tag{7.3}$$

where $\hat{\mathbf{m}}$ is the unit vector in the direction OS.

7.4 Grating design

The model developed here enables us to calculate the far-field radiation pattern of any 2D grating, once the equation of the curves $\mathcal{C}_m$ is known. We are interested in a particular grating that would scatter SWs originating from a point source into a collimated free-space beam of arbitrary direction (θ, φ). We obtain the equation of the curves $\mathcal{C}_m$ for such a grating by requiring constructive interference in that specific direction. This condition is $\Delta\phi = m2\pi$, m being an integer. Introducing the SW effective index n_{sw}, we obtain from (7.3) the equation that yields the position of the scatterers:

$$\rho = \rho_m(\psi) = \lambda_0 \frac{m - c_1/2\pi}{n_{sw} - \sin(\theta)\cos(\psi - \varphi)}. \tag{7.4}$$

This equation states that the scatterers must be located on the curves $\mathcal{C}_m$ defined by the polar equations $\rho = \rho_m(\psi)$ for all emitted fields to constructively interfere in the

direction (θ, φ). The curves $\mathcal{C}_m$ are ellipses with the origin O at one of their foci. Note that the ellipses $\mathcal{C}'_m$, obtained by translation of the ellipses $\mathcal{C}_m$ in such a way as to position O at the other focus, would lead to constructive interference in the direction $(\theta, \varphi + \pi)$. As our experimental set-up scans the far-field in the angle system (θ_x, θ_y), which are the angles with respect to the z-axis projected on the planes x-z and y-z (Figure 7.1(c)), we convert the angle system (θ, φ) to this new one.

Chapter 8

Experimental demonstration of multi-beam plasmonic collimators

8.1 Design of elliptical plasmonic gratings for off-axis collimation

We now use the model presented in Chapter 7 to devise a general class of plasmonic lenses that collimate light originating from a single point source and direct it into one or several free-space beams propagating along arbitrary off-axis directions, thus enabling flexible interfacing of plasmonic devices with complex optical systems.

From (7.2) and (7.4) we are able to calculate the far-field patterns of elliptical gratings. In order to demonstrate that such elliptical gratings can act as plasmonic lenses, we

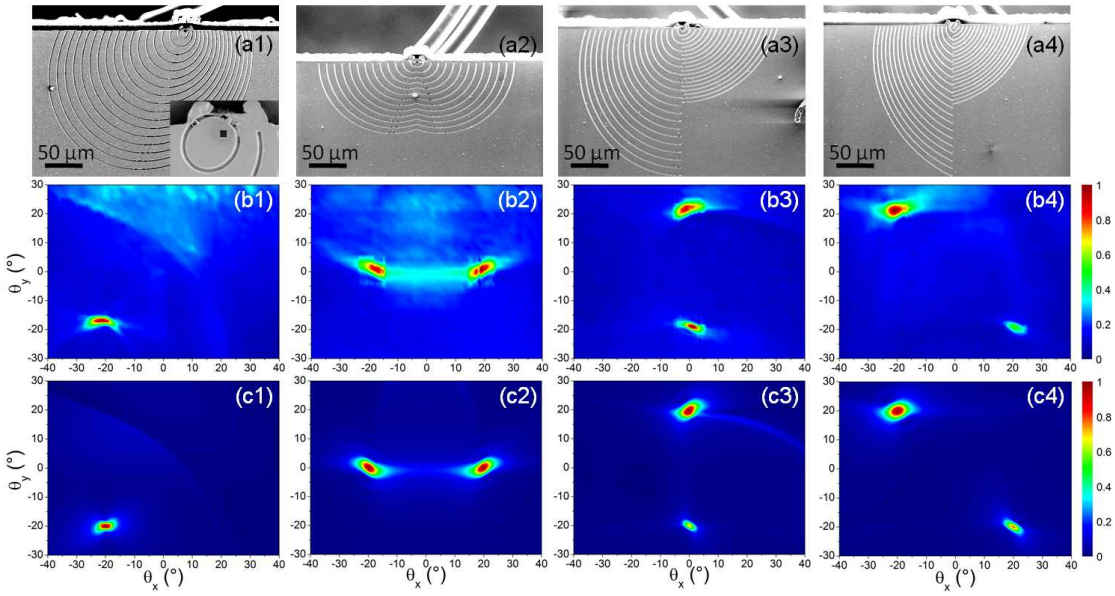

FIGURE 8.1: Four different plasmonic lenses producing one (a1) or two (a2, a3, a4) beams, fabricated on the facet of quantum cascade lasers. For each structure, we show an SEM image (a), and the measured (b) and calculated (using the model we develop herein) (c) far-field intensity (normalized to 1). The inset in (a1) is a close-up image of a typical aperture. The measured far-fields are obtained by scanning a liquid-nitrogen-cooled mercury-cadmium-telluride detector, positioned 10-20 cm away from the device, over θ_x and θ_y, with a resolution of 0.5°.

fabricated the structures directly on the gold-coated facet of mid-infrared quantum cascade lasers (QCLs) emitting at $\lambda = 8.06$ μm, using the process described in [64]. QCLs with small divergence beams are highly desirable. Second-order gratings directly defined on the laser waveguide are often used to obtain surface emission into a beam with reduced divergence in the direction along the laser ridge [46, 79]. Using aperiodic gratings, multi-beam emission has been demonstrated in such structures [44] and collimation in two-dimension has been reported for gratings defined on microdisk or ring cavities [80, 81]. However, the solution we present here offers the advantage that it decouples beam engineering from waveguide engineering, providing much more flexibility. Previous demonstrations of multi-beam emission from semiconductor lasers using plasmonic

structures defined on their facet relied on simple 1D gratings which resulted in asymmetric beam shapes [82]. These structures presented limited control over the direction of emission. Here, the application of our dipolar model has enabled us to overcome these limitations by facilitating the design of more complex grating structures. Note also that the concept is general and such lenses can be implemented on any structure supporting surface waves or quasi-two-dimensional optical modes (e.g. slab waveguides). It is also scalable to other spectral ranges.

We performed 2D simulations of a 1D grating, using a commercial FEM simulation package (COMSOL Multiphysics), in order to design the groove parameters and extract the relevant parameters. Groove depth and width of 1 μm have been found to maximize the peak intensity of the collimated beam for a grating comprising 10 to 20 grooves. This optimization relies on a trade-off between the grooves scattering efficiency and the amount of energy reaching the last grooves. With these dimensions, and for an off-resonance grating (i.e. for a grating period different from $m \cdot \lambda_{sw}/2$, where $m = 1, 2, 3, ...$), we estimated $n_{sw} \simeq 1.03$ and $c_1/2\pi \simeq 0.23$ at $\lambda = 8.06$ μm. The decay law was found to scale as $\rho^{-1/2}$. This is consistent with the decay of quasi-cylindrical waves (which is the dominant mode of propagation of SWs at long wavelengths [83]) and implies a dependency $f_1(\rho) \propto \rho^{-1}$ for the 3D case. Finally, we neglected the variation of f_3 with ψ since the SWs always impinge on the grooves with an angle close to $\pi/2$ in our small eccentricity elliptical gratings.

8.2 Collimator fabrication

Figure 8.1(a1) shows a scanning electron microscope (SEM) image of a representative fabricated grating, designed to emit light in the direction ($\theta_x = -20°, \theta_y = -20°$). In this device, the point-like source of SWs is an aperture opened in the metal film (inset in figure 8.1(a1)). The light in the laser waveguide impinges on the back side of the aperture, launching SWs on the grating-air interface, along with some directly transmitted light. The point-like character of the aperture stems from its subwavelength dimensions (2 μm x 2 μm for $\lambda = 8.06$ μm).

The fabrication process involves focused ion beam (FIB) milling to sculpt 1-μm-wide and 1-μm-deep grooves into the semiconductor facet (indium phosphide), then deposition of 250 nm of alumina, acting as an insulation layer, followed by 250 nm of gold. The small aperture in the metal film is eventually opened using FIB [64]. As can be seen in figure 8.1(a1), only a portion of the grating is fabricated because of the geometry of our laser facet.

8.3 Experimental results

8.3.1 Single beam emission

Figure 8.1(b1) presents the measured far-field of the device shown in figure 8.1(a1), which is composed of 13 grooves described by (7.4). The direction of highest intensity is centered at ($\theta_x = -21°, \theta_y = -17°$). The angular divergence, defined as the full width at

half maximum (FWHM), is about 8° along θ_x and 3° along θ_y. This divergence angle is comparable to those obtained with simple circular collimator designs [65] and represents a dramatic improvement compared to the divergence angles of about 40° along θ_x and 70° along θ_y for the original unpatterned laser. The small discrepancy between our data and the designed angular direction is due to misalignment of the far-field measurement set-up. Note that a residual signal is visible in the upper part of the measured far-field, mainly due to light emitted from the back facet of the laser reaching the detector after undesired reflection on the laser mount. To suppress this signal, high reflection coatings have been applied to the back facets of the devices subsequently fabricated (a2, a3 and a4). Moreover, a background, which is measured to be $\sim 10\%$ of the maximum intensity, is present. As only a small portion of the light throughput is coupled into the SWs, the destructive interference between the fields scattered by the grooves and the strong direct emission from the aperture is not complete. This results in the background observed. This coupling efficiency could be greatly increased by patterning the metal around the aperture with subwavelength grooves to reduce the wavevector mismatch between the laser waveguide mode and the SWs, as was demonstrated in the terahertz range by Yu *et al.* in [77].

This data demonstrates that our 2D plasmonic grating transforms a point source of SWs located at the focal point into a collimated free-space beam in a tailorable direction, i.e. it acts as planar plasmonic lens.

8.3.2 Multi beam emission

We now show that one can design a plasmonic lens with a single focus capable of forming several beams in arbitrary preselected directions. This is achieved by placing portions of different gratings side by side on the facet. We fabricated three different structures (Figure 8.1)(a2,a3,a4), each designed to collimate light in two specific directions, respectively ($\theta_x = \pm 20°$,$\theta_y = 0°$) with $N = 13$ grooves, ($\theta_x = 0°$,$\theta_y = \pm 20°$) with $N = 19$ and ($\theta_x = \pm 20°$ and $\theta_y = \mp 20°$) with $N = 20$. The results are presented in figure 8.1 (columns 2, 3 and 4), where both the measured (b) and calculated (c) far-field intensity are plotted. The two collimated beams are clearly distinguishable for each plasmonic lens, proving the robustness of the concept.

Figure 8.1(c) shows the radiation pattern emitted by the four structures in figure 8.1(a), calculated using (7.2) and considering a source polarized along y ($\psi_s = \pi/2$). We included in $\mathbf{E}(\mathbf{r})$ only the fields scattered by the grating. The other contributions due for example to the light directly radiated at the aperture will contribute to the background but will not alter significantly the shape of the collimated beam. Our model aims at elucidating the intrinsic operation of the gratings, and we thus considered them to be free of the defects stemming from our specific implementation. For each plasmonic lens, the agreement between calculated and measured data (Figure 8.1(b)) is good. The shape of the collimated beams is well reproduced, and the measured divergence angle is generally close to the calculated one (relative error of $\sim 15\%$ in average). The discrepancies are mainly attributed to fabrication defects, in particular the presence on the grating surface

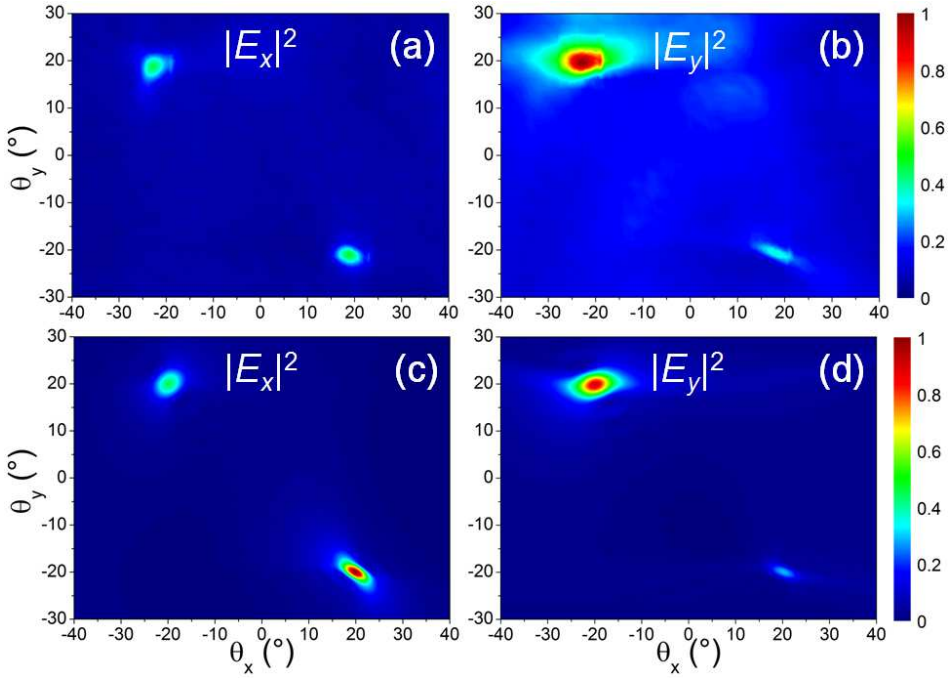

FIGURE 8.2: Far-field of the device (4) of figure 8.1. Measured field intensity $|E_x|^2$ (a) and $|E_y|^2$ (b), normalized to 1. Calculated field intensity $|E_x|^2$ (c) and $|E_y|^2$ (d), normalized to 1.

of dust particles that open additional scattering channels and reduce the propagation length of the SWs. The finite size of the spot is determined by the SW decay and the size of the grating.

8.3.3 Polarization of the emitted light

Since our model is vectorial, we can extract the state of polarization of the emitted light. Figure 8.2 shows the components $|E_x|^2$ and $|E_y|^2$ both calculated and measured (via a polarizer) for the fourth device of figure 8.1. The agreement between experimental and calculated data is good, which confirms the validity of our model relying on radiating dipoles oriented perpendicular to the groove tangent.

We finally note that our model gives the phase profile of the far-field as well. This model might thus be particularly valuable for designing new plasmonic components featuring complex phase responses, which could generate, for example, Bessel beams or optical vortices.

8.4 Conclusion

In summary, we introduced a phenomenological model to describe 2D metallic gratings. Using this model, we designed a new class of plasmonic lenses, capable of producing multiple free-space beams, in arbitrary directions, when a point source of surface waves is located at their focus. As an example of application, we demonstrated dual-beam emission from mid-infrared quantum cascade lasers and showed the versatility of the concept by realizing different emission directions.

Chapter 9

High-power low-divergence tapered quantum cascade lasers with plasmonic collimators

9.1 Overview

In this chapter, we demonstrate a tapered quantum cascade laser with sloped side-walls emitting a high-brightness single-lobe beam at 8.1 μm with a peak power of 4 W at room temperature. Using a combination of high and low reflectivity facet coatings, the power output is increased to 6.2 W while a high beam quality is maintained. Plasmonic collimators are fabricated on the facet of the uncoated lasers without compromising power output, demonstrating the viability of this beam-shaping strategy for high-power

lasers. The collimated lasers emit a beam with a more cylindrical cross-section which is more amenable to high-efficiency coupling into mid-infrared optical fibers.

9.2 Design and fabrication of tapered quantum cascade lasers

For many applications of quantum cascade lasers, from spectroscopy [4] to free-space communication [84] and military countermeasures, high power output and lasing on the fundamental transverse mode are desirable.

While high-power QCLs can be obtained by increasing the device area, their beam profile degrades quickly as higher-order lateral cavity modes are excited. To account for this tradeoff between beam quality and power, it is important to maximize the brightness of the laser given by $B = P/(\lambda^2 M_x^2 M_y^2)$, where P is the total emitted power, λ is the wavelength, and $M_{x,y}^2 = (4\pi/\lambda)\sigma_{0\mathrm{x,y}}\sigma_{\theta\mathrm{x,y}}$, where σ_0 and σ_θ are the standard deviations of the near-field spatial intensity profile and the far-field angular intensity profile, respectively, in either the x or y directions [85, 86]. The M^2 value is the ratio of the divergence angle of the laser to the divergence angle of a Gaussian beam whose waist is equal to the waist of the laser beam $w \equiv 2\sigma_0$, so that $M_{x,y}^2 = 1$ for a diffraction limited beam and larger otherwise. For semiconductor lasers, we can take $M_y^2 = 1$, due to the strong vertical mode confinement, and consider only the beam distortion in the lateral direction.

Angled cavity QCLs with broad waveguides have been reported [87] for lateral mode control, but no data was provided on the robustness of the design as driving current is increased.

One method of achieving high brightness is the master oscillator/tapered amplifier (MOPA) geometry, in which the output of a nearly diffraction-limited seed laser is directed through a tapered gain section, which acts as a traveling wave amplifier. The broader area of the tapered section mitigates the effect of gain saturation on reducing the single-pass gain. Such an architecture has been implemented in both interband lasers using gain guiding [88] and QCLs using index guiding [89, 90]. To prevent lasing in the amplifier section, the front facet can be antireflection (AR) coated [88, 90] or cleaved at a small angle relative to the normal to the propagating direction [89]. Since QCLs can be tailored to emit across a broad range of the mid-IR spectrum, the design of an AR coating for broadband MOPA QCLs becomes a very challenging issue. The need for an AR coating at the facet also makes the fabrication of integrated photonic circuits coupled to a MOPA QCL difficult. Furthermore, the MOPA devices require separate electrical contacts for the seed and amplifier sections.

Tapered lasers are a different approach in which the laser oscillation takes place in the combined tapered and seed sections and require only a single top contact. A short ridge waveguide section is followed by a tapered waveguide section, which expands at an angle smaller than the free diffraction angle of the fundamental mode of the ridge. (Such a geometry is also useful for improving the outcoupling of terahertz radiation generated by difference frequency generation in QCLs [91, 92]. The ridge is narrow enough that the

losses for higher-order lateral modes are substantially greater than for the fundamental mode; the preferred fundamental mode is then adiabatically expanded in the tapered section. Such tapered QCLs have been demonstrated with vertical sidewalls, an AR coating on the wide facet and high reflectivity coating on the narrow facet, but the peak output power was limited to 200 mW [93]. To further improve the beam quality, we proposed to enhance the loss disparity between the fundamental and higher-order lateral modes in the ridge section using curved sidewalls, which were recently shown to introduce additional losses in the form of reflection into the InP bulk as well as plasmonic losses [94]. Although this loss is detrimental for a narrow Fabry-Perot (FP) ridge laser because it affects the fundamental mode as well, the additional losses are even greater for the higher-order modes, which have greater intensity near the walls.

Using this approach, we showed that QCLs with tapered waveguides, curved wet-etched side-walls and no AR coatings feature the high power of broad-area QCLs while maintaining a good beam quality [95]. We reported a 1° half-width tapered device with a peak power of 2.5 W at 9.5 μm, an M^2 of 2.08 and a maximum brightness of 1.4 MW cm^{-2} sr^{-1}.

In the present work, we improve these results using a different QCL material [19] lasing at 8.1 μm and grown by metal-organic chemical vapor deposition. A schematic top-view of the waveguide design is shown in the inset of Fig. 9.1 (a). It consists of a 0.5 mm-long and 14 μm-wide narrow ridge section, followed by a 2.5 mm-long tapered section with a 1° half-angle. The waveguides were defined by wet etching two trenches approximately 20 μm-wide and with a depth reaching just beyond the active region ($\approx 9.5\mu$m). This

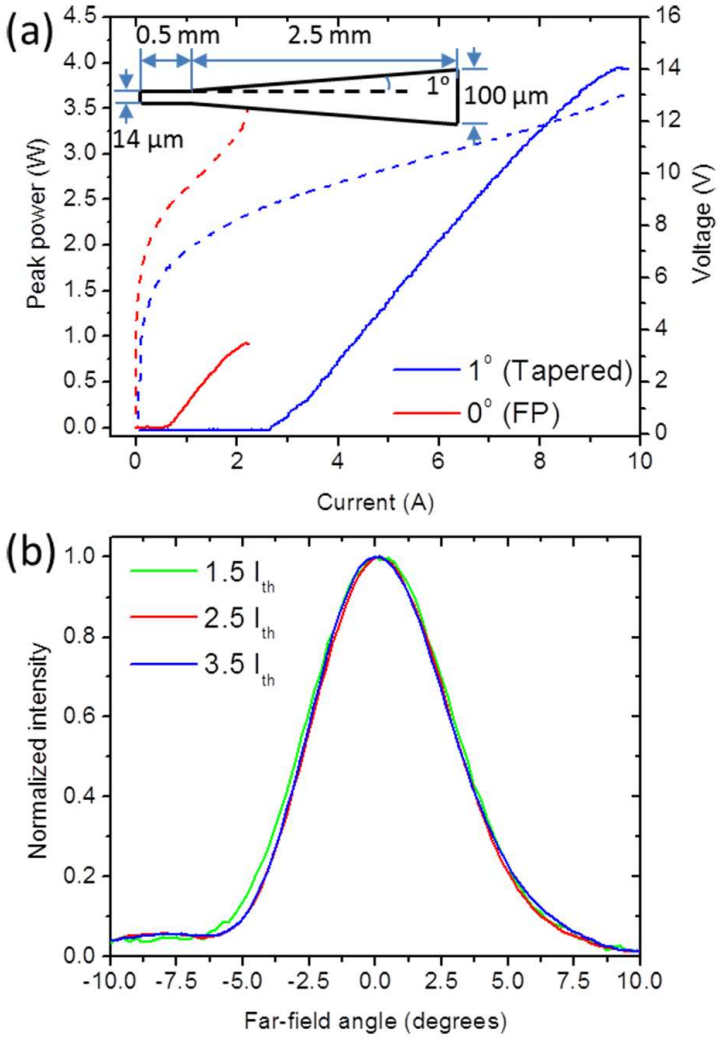

FIGURE 9.1: (a) L-I (solid) and I-V (dashed) curves of representative FP and tapered QCLs with 1° taper half-angle (laser A). The FP laser waveguide is 14 μm-wide and 3 mm-long. The optical power is measured from the front (wide) facet. Inset: schematic of the waveguide structure. (b) Far-field profiles of laser A for increasing pump current. The far-fields are measured using a thermoelectrically cooled mercury-cadmium-telluride detector mounted on a rotation stage 18 cm away from the laser facet. The plane of the scan is parallel to the planes of the QCL epitaxial layers (slow axis).

resulted in sidewalls inclined at about 37° with respect to the plane of the epitaxial layers. A 500 nm-thick SiN passivation layer was then deposited by plasma-enhanced chemical vapor deposition and opened by reactive ion etching on top of the laser ridges. The contact opening is also tapered so that the width of the contact is about half the waveguide width all along the laser. Top and bottom metallization consisted of Ti (15 nm) and Au (350 nm) layers. Finally, an additional 4 μm of gold was electroplated on the top contact to improve heat dissipation. The wafer was then cleaved into 3 mm-long chips which were indium-soldered epi-side up on copper heat sinks. For all the results presented here, the lasers are driven in pulsed operation, with a 10 kHz repetition rate and 100 ns pulse width, and maintained at 20° C with a Peltier cooler.

Fig. 9.1 (a) shows the L-I and I-V characteristics of a representative tapered QCL (laser A), as well as a Fabry-Perot (FP) QCL (i.e. non-tapered QCL, 14 μm-wide, 3 mm-long) for comparison. The tapered QCL reaches 3.95 W peak power. For comparison, devices reported in [95] with a similar geometry and lasing at 9.5 μm had a peak power of 2.5 W. The increased performance from this earlier work is due to the different active region design and growth conditions. The slope efficiencies for the FP and the tapered QCLs are 720 and 660 mW/A, respectively. The small reduction in slope efficiency can be ascribed to higher optical losses due to the small non-adiabaticity of the taper. From the same fabrication run, we cleaved five 3 mm-long chips, each containing four similar tapered QCLs. We measured the L-I curves of the 20 tapered lasers and found an average peak power of 4.08 W with a standard deviation of 0.35 W.

The far-field profile of laser A (along the slow axis) is shown in Fig. 9.1 (b). We observe

only a small dependence on drive current across the operating range. The M^2 value is calculated to be between 1.6 (at $I = 2\ I_{th}$) and 1.8 (at $I = 3.5\ I_{th}$) while the maximum brightness reaches 3.35 MW cm^{-2} sr^{-1} (details on the definitions and calculations of M^2 and brightness can be found in [85, 86, 95]). Gain, temperature or refractive index inhomogeneities in the waveguide as well as scattering from facet defects provide a coupling mechanism between lateral modes and can cause the asymmetries and small side-lobes sometimes observed in the far-field. For this fabrication run, facet defects are expected to play a predominant role since the continuous thick electroplated gold contact covered the entire waveguide, which led to difficult cleaving of the wafer. This can be improved easily by leaving narrow sections of the waveguide free of electroplated gold. On some of the devices measured, the lasers could start lasing predominantly on a higher order lateral mode when driven beyond 80% to 90% of the roll-over current. This was usually also visible in the L-I curve since it translates into a change in slope efficiency. The far-field of the FP laser (not shown) was Gaussian with a full-width at half-maximum of 43.7° and independent of current, from just above threshold to the roll-over current.

9.3 Optimization of the power output using facet coatings

We then proceeded to optimize the power output of the tapered QCLs using a high reflectivity (HR) coating on the back facet and a low-reflectivity (LR) coating on the front facet. Such a strategy has already been successfully employed to optimize the

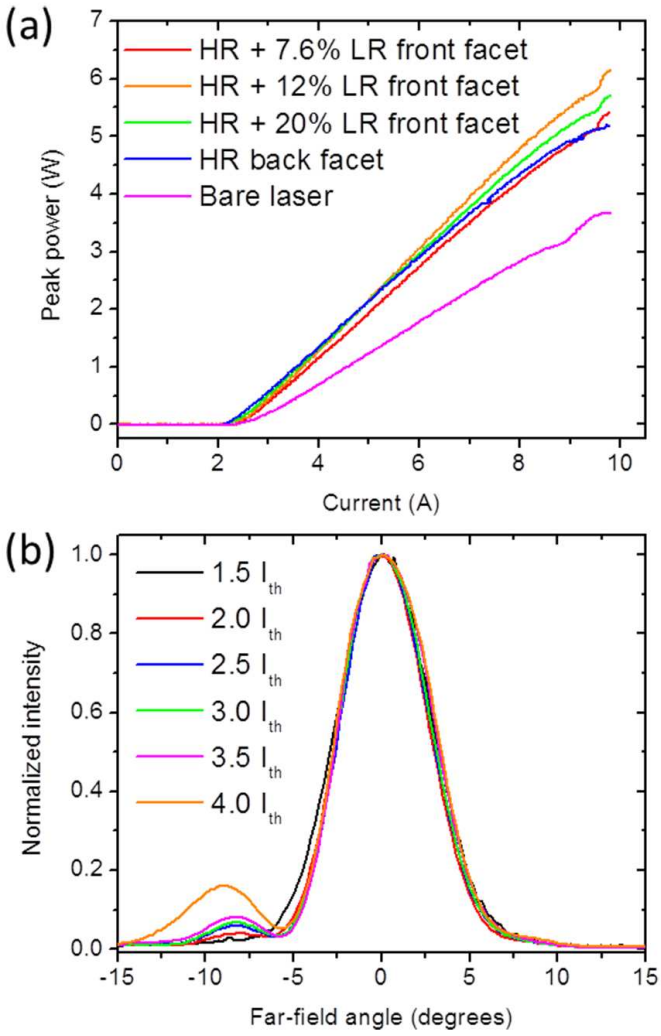

FIGURE 9.2: (a) LI curves of a representative tapered QCL with different facet coatings. The successive thicknesses reached by the LR coating are 740 nm, 1110 nm and 1510 nm, corresponding respectively to theoretical reflectivities of 20%, 12% and 7.6%. (b) Far-field profiles of the final device shown in (a), with HR coating on the back facet and 7.6% LR coating on the front facet, for increasing pump current.

output power of either long [96] or short[97] cavity QCLs operating at 4.6 μm. The HR coating here consists of a 50 nm-thick Al_2O_3 insulating layer followed by a 10 nm-thick titanium adhesion layer and a 400 nm-thick gold reflecting layer, all deposited by electron-beam evaporation. The LR coating was realized by a single layer of Al_2O_3. While Al_2O_3 starts having optical losses around 8 μm ($\approx$ 150 cm^{-1}), we chose to use this material because of its good thermal and insulating properties, its ease of deposition and its reliable adhesion to QCL facets. The refractive index [98] of Al_2O_3 at 8.1 μm is close to 1.37, allowing to reach reflectivities between 29% (uncoated) and 7.6% (quarter-wave layer). We use 3.3 as the refractive index of the QCL waveguide in our calculations. Successive electron-beam evaporations resulted in an Al_2O_3 layer with increasing thickness from 740 nm to 1100 nm to 1510 nm, corresponding respectively to theoretical reflectivities of 20%, 12% and 7.6%.

The L-I characteristics of the uncoated original device (laser B) and measured after each deposition are shown in Fig. 9.2 (a). We observe that the HR coating improves the power output by 40% to a peak power of 5.2 W. While theoretical analyses have been employed in the literature [96, 97] to predict the optimal front facet reflectivity (or equivalently, the optimal laser length), they usually rely on the assumption of uniform gain saturation and photon density, which is not valid with our geometry. We measured the output power from both the front (wide) and the back (narrow) facet of uncoated tapered lasers and observed that the power emitted from the back facet is typically only about 65% of the power emitted from the front facet. Since the narrow and broad facets have similar transmission, this indicates that the photon density (P) does not

simply scale with the width (w) of waveguide ($P.w$ $\neq$constant). A correct modeling of the photon density inside the tapered laser is outside the scope of this paper. We thus rely on an experimental study to approximate the optimal front facet reflectivity. We obtain a maximum peak power of 6.2 W for the LR coating with 12% reflectivity. This corresponds to an increase of the power output by 67% compared to the uncoated device. The lowest reflectivity coating (7.6%) has a reduced output power and is thus past the optimal value of reflectivity. We also note that for this last device the slope efficiency is reduced which indicates that the laser experiences stronger waveguide losses (in addition to increased mirror losses). We attribute these losses to absorption in the Al_2O_3 quarter wave layer, since more intensity builds up inside the resonant layer.

A discontinuity in the slope efficiency can be observed in the L-I characteristics shown in Fig. 9.2 (a) at high currents (I $\approx$ 9.5 A). It corresponds to the lasing threshold of a higher order lateral mode. We can observe from the LI curves that this threshold is affected by the coatings, although not in a straight-forward manner, as indicated by the absence of observed higher order mode for the HR coated device measured. Scattering from facet defects and diffraction upon reflection are expected to influence the lateral mode structure since they are major coupling mechanisms between the different lateral modes. Both effects are modified by facet coatings. Previous works reported the use of anti-reflection coatings on the front facet of a tapered QCL in order to improve the beam shape [93].

Figure 9.2 (b) shows the far-field profiles of laser B with the final coating (HR + 7.6% LR) for increasing drive currents. Apart from a small side lobe that grows with increasing

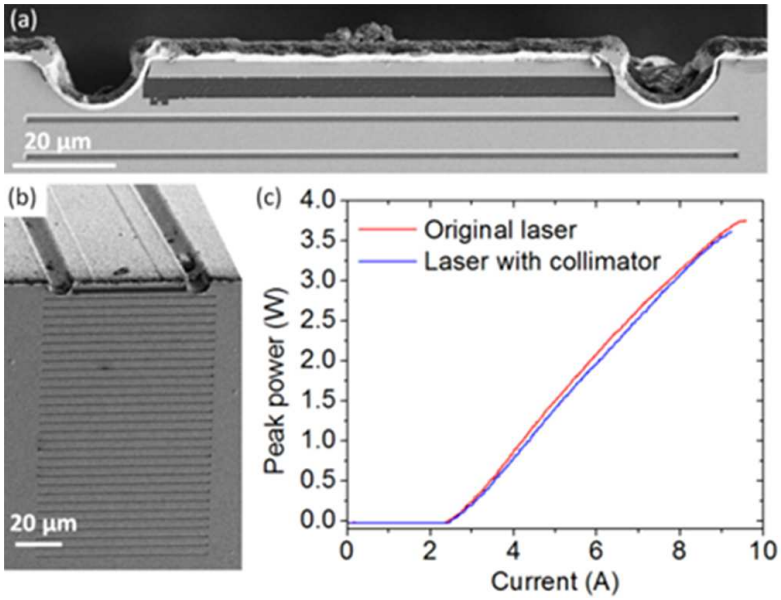

FIGURE 9.3: (a) Scanning electron micrograph (SEM) image of a collimator fabricated on the facet of an uncoated tapered laser (laser C), after deposition of Al_2O_3 and Au and subsequent opening of the aperture in front of the laser waveguide. (b)SEM image of the collimator. The substrate of the QCL (250 μm) can accommodate 30 large grooves constituting a second-order grating with period 7.5 μm. The grooves are 130 μm long, 1.7 μm wide and 1 μm deep. After subsequent deposition of Al_2O_3 (90 nm) and Au (250 nm) by sputtering, the groove width is reduced to 1 μm. (c) LI curve of the device shown in (a) and (b), taken before and after fabrication of the plasmonic collimator. Both the collimated beam and a residual uncollimated background are measured by the powermeter placed directly in front of the laser.

drive current, the far-field is very stable. The M^2 value is 1.6 at $I = 3.5I_{th}$, where the maximum brightness of 4.05 MW cm^{-2} sr^{-1} is reached. As discussed earlier, the side-lobe observed indicates the presence of higher order lateral modes.

9.4 Plasmonic collimator on the facet of high power quantum cascade lasers

Since the aperture of the laser at the end of the taper is very wide while its height remains bound by the active region thickness, the output beam has a very elongated cross-section, with a typical full-width at half-maximum of 6.1° in the slow axis and more than 60° in the fast axis. Furthermore, since the waveguide mode reaches the facet with a non-uniform phase profile along the lateral direction, it diverges in the slow axis from a virtual source that is approximately L/n_{wg} behind the output facet, where L is the length of the taper and n_{wg} is the refractive index of the QCL waveguide [99]. In contrast, the beam diverges from the output facet in the fast axis. This results in an astigmatism of the beam.

In an attempt to address these issues, we employed a strategy developed in our group to shape the output of edge-emitting QCLs into low-divergence beams using plasmonic collimators defined on their facets [10, 63, 65]. Plasmonic collimators are composed of an aperture and a grating defined on the gold-coated facet of a semiconductor laser. The light coming from the laser waveguide passes through the aperture where it partially couples to surface plasmons (SP) propagating along the facet, which are in turn scattered by the grating grooves. The grating can be viewed as an antenna array, with the fields scattered by the grooves and the field directly radiated into free-space by the aperture all constructively interfering to form a low-divergence beam. In addition to achieving low-divergence output for standard edge emitting Fabry-Perot QCLs ($< 4°$ in both vertical

and horizontal directions [65]), plasmonic collimators can be used for polarization control [82] and multi-beam emission [11]. However, previous results on low-divergence QCLs using plasmonic collimators showed substantial reduction of the power output (as much as 80% power reduction for the smallest divergence obtained [65]). This power reduction is caused by the low transmitivity of the aperture opened in front of the laser waveguide, especially for two-dimensional collimators (collimating in both the fast and slow axis) which require a small aperture to diffract the SP waves and spread the energy laterally on the laser facet [65]. Here, since the output beam already has a small lateral divergence because of the large width of the aperture (100 μm), we only need a one dimensional collimator (with straight grooves and a broad aperture) in order to reduce the divergence along the fast axis. The large width of the aperture (98 μm) results in a very small overlap between its lateral edges and the waveguide mode. Additionally, we chose the vertical dimension for the aperture (4 μm) to be larger than the waveguide thickness (3.5 μm) to reduce the overlap between the horizontal edges of the aperture and the laser waveguide mode. While this comes at the expense of a lower coupling to SP waves and results in a larger uncollimated background, we expect an increased power output compared to earlier collimator designs.

The fabrication method is similar to the one described in [65]. Focus ion beam (FIB) milling was used to define 30 grooves into the 250 μm-thick InP substrate of a QCL (laser C). A 90-nm-thick Al_2O_3 film was then deposited for electrical insulation, followed by a 250-nm-thick gold film. For both depositions, we used sputtering in order to obtain a quasi-conformal coating of the grooves. Finally, the aperture was opened using FIB. Fig.

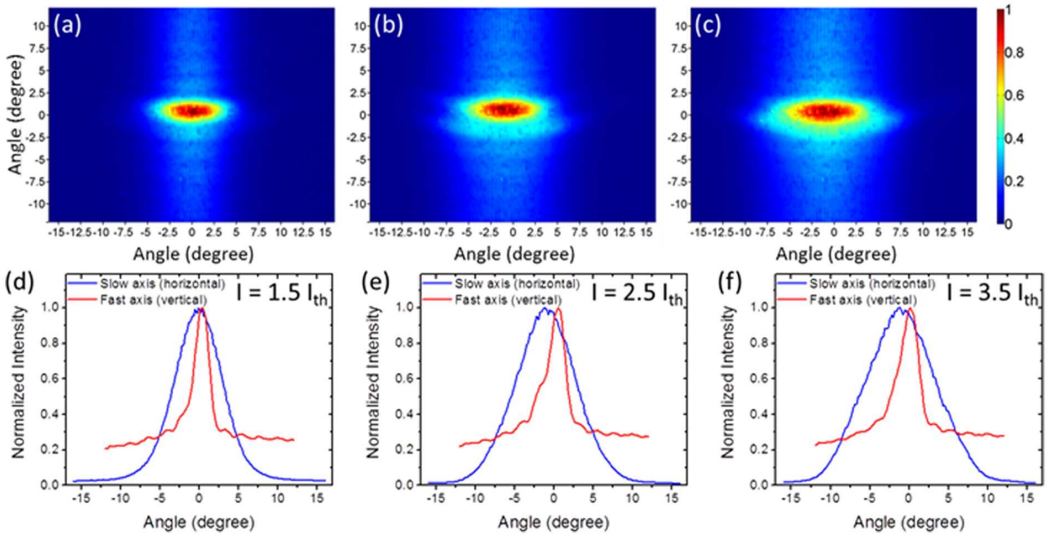

FIGURE 9.4: (a)-(c) Two-dimensional far-field intensity distribution (normalized) of the tapered QCL with plasmonic collimator (laser C), measured using a mid-infrared microbolometer array (160 x 120 pixels, INO IRXCAM) with no optics placed directly in front of the laser facet. From (a) to (c), the pump current is respectively 1.5 I_{th}, 2.5 I_{th} and 3.5 I_{th}. The angles are computed from the known pixel pitch (52 μm) and the distance between the facet and the sensor (14 mm). (d)-(f) Respective averages of the column and rows of the images shown in (a)-(c), showing the horizontal and vertical profiles of the beam.

9.3 (a) shows a zoomed-in scanning electron microscope (SEM) image of the resulting aperture. An SEM image of the pattern facet is shown in Fig. 9.3 (b). The grating design parameters are detailed in the caption. We observe in Fig. 9.3 (c) the L-I characteristics of laser C, before and after fabrication of the collimator. The L-I characteristics are almost indistinguishable, demonstrating that the plasmonic collimator does not affect significantly the power output of the QCL. A maximum peak power of 3.6 W is reached for the collimated device. The maximum output power of previously reported plasmonic collimators is under 200 mW [10].

We measured the two-dimensional far-field profile of the collimated laser C for different driving currents, using a bare mid-infrared microbolometer array placed directly in front

of the laser facet. The results are shown in Fig. 9.4 (a)-(c). We observe that the collimator results in a central low-divergence beam with FWHM of 7.1° and 2.8° respectively along the slow and fast axis, for a driving current of $I = 1.5\ I_{th}$. However, the directivity [10] achieved is fairly low (< 15 dB) because of the substantial uncollimated background whose level is between 20% and 30% of the peak intensity. As the current is increased, we observe a broadening of the central beam in the slow axis which could be caused by a narrowing of the intracavity lateral intensity profile.

9.5 Conclusion

We have demonstrated high-power, high-brightness QCLs based on 1° tapered waveguides with sloped side-walls. Their output power was optimized using a combination of HR and LR coatings, reaching a maximum peak power of 6.2W. Plasmonic collimators were employed on the original uncoated tapered lasers to reduce the large fast axis beam divergence and obtain a more cylindrical beam shape, which may circumvent the need for external beam-shaping optics in applications such as high-efficiency coupling into mid-infrared optical fibers. The high power output was preserved in the presence of the plasmonic collimators.

Part III

Design of passive flat optical elements in the infrared

Chapter 10

Multi-wavelength mid-infrared plasmonic antennas with single nanoscale focal point

10.1 Introduction

Infrared near-field imaging and spectroscopy are emerging as powerful tools for the understanding of the structure and chemistry of materials at the nanoscale. Recent notable examples include the infrared nanoscopy of strained semiconductors [100] and the nanoscale free-carrier profiling of semiconductor nanowires [101]. A major development in this field was a recent demonstration of infrared-spectroscopic nanoimaging using a thermal source [102]. The ability to use a spectrally broad source in such systems

allows for the use of Fourier-transform infrared (FTIR) spectroscopy techniques at the nanoscale for the chemical identification of unknown nanostructures.

These applications typically rely on the use of scattering-type scanning near-field optical microscopy (s-SNOM) [103–106], where the diffraction limit is overcome by the use of a sharp atomic force microscope (AFM) tip acting as an antenna to concentrate the incident radiation to nanoscale volumes. By measuring the light scattered by the tip, one can obtain information on the local properties of a sample. One limit of this technique lies in the weakness of the tip-scattered field requiring complex detection schemes to isolate it from the strong background [107]. There is thus a need for more refined techniques to feed power into a nanoscale volume. Recent examples of such techniques make use of tapered transmission lines [108] and adiabatic compression of surface plasmon polaritons [109].

We approach this technologically relevant problem by considering a novel optical antenna structure collecting radiation over an extended area and funneling it into a single well-defined nanoscale focal spot. Following a design strategy recently proposed for multi-wavelength plasmonic nanoantennas in the visible range [110], we present here a design based on embedding a single bow-tie nanoantenna in an array of scattering nanoparticles that funnel incident radiation into the central gap of the bow-tie. Moreover, we demonstrate the possibility to achieve multi-frequency operation by using nested particle arrays with multiple periodicities. Such multiple-wavelength single-focus structures implemented on the facet of a chalcogenide fiber [111] would enable the realization of a fiber-based multi-channel infrared scanning optical microscope by providing efficient

focusing of the incident fiber-mode field into the nanoscale gap of the central bow-tie, while suppressing alignment sensitivity.

Moreover, differently from antenna arrays with periodic or aperiodic geometries featuring a high-density of hot-spots embedded in a background of photonic-plasmonic modes [51, 112–116], the proposed single hot-spot structure benefit from enhanced spatial resolution due to the large contrast between the field enhancement at the gap of a bow-tie antenna and at the edges of the metallic nanoparticles surrounding the isolated hot-spot.

10.2 Photonic-plasmonic coupling

In order to describe the proposed design strategy, we first study a simplified design, as shown in Fig. 10.1(a), providing high field enhancement at only one selected wavelength. It relies on the use of a bow-tie antenna (shown in Fig. 10.1(b)) surrounded by straight single-periodic arrays of identical discs to concentrate light onto the bow-tie. The antenna performance is optimized for normal illumination by a plane wave linearly polarized along the bow-tie direction.

We used a commercial Fourier-transform time-domain (FDTD) package (Lumerical FDTD) to simulate the electromagnetic behavior of these structures. Throughout this paper, we will use the term field enhancement to refer to the quantity $|E|^2 / |E0|^2$, where E is the peak near-field amplitude of the electric field generated either in the center of the antenna gap in the case of the bow-tie, or in close proximity to the edge in the direction of the incident polarization in the case of the discs; normalized to the incident

field intensity $|E0|^2$. In all simulations, the structures are illuminated from the substrate side by a linearly-polarized plane wave.

The structures were designed to operate in the mid-infrared spectral region (free space wavelength $\lambda = 5 - 10$ μm). Gold was chosen as a preferred material for the plasmonic elements because of its relatively low losses in that spectral range. Optical constants for gold used in the numerical simulations were taken from [98]. In all simulations and experiments the structures are located at an interface between a barium fluoride (BaF_2) substrate and air. BaF_2 was chosen as a substrate because it is transparent in the spectral region of interest and has a relatively low refractive index ($n \approx 1.42$) compared to other conventionally used mid-infrared materials (e.g. ZnSe $n \approx 2.4$, Ge $n \approx 4.0$, Si $n \approx 3.42$). A low refractive index is desirable in order to reduce dephasing effects between the waves propagating in air and those propagating in the substrate, since both concentrate energy onto the bow-tie antenna. Reduced dephasing effects result in sharper photonic-plasmonic resonances [117].

10.3 Design of a photonic-plasmonic antenna

We followed a hierarchical approach to designing and optimizing this antenna, starting from tuning the local properties of individual plasmonic particles followed by the controlled assembly of these elements into ensembles whose scattering response is defined by their collective electromagnetic properties. For example, we maximized the amplitude of the field scattered by the array by overlapping the localized surface plasmon (LSP)

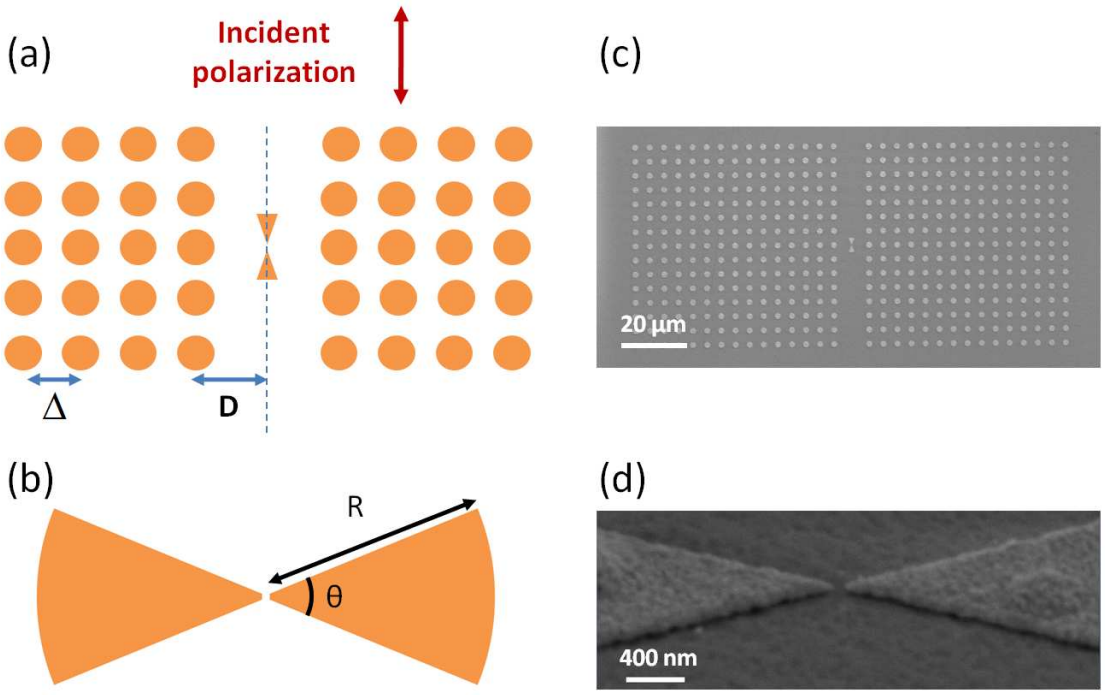

FIGURE 10.1: (a) Schematic of a hybrid plasmonic-photonic antenna consisting of a bow-tie antenna surrounded by straight single-periodic arrays of identical discs. Light is assumed to be incident normal to the plane of the structure and with a polarization oriented vertically. The main parameters to be adjusted in the design are the discs diameter, the array periodicity Δ and the distance D between the arrays and the central bow-tie antenna. (b) Schematic of the gold bow-tie antenna considered in this work. It is composed of two sections of disc with radius R = 2.2μm and $\theta = 45°$ opening angle. The central gap is 100 nm wide. (c) and (d) Scanning electron microscope (SEM) images of the fabricated structures. The gold discs have a radius of 890 nm. All structures have a thickness of 70 nm are deposited on a BaF_2 substrate. A zoom-in of the bow-tie gap is shown in (c).

resonance of each individual disc and the collective array resonance, because the scattering efficiency of each disc is maximized on resonance. This interplay between localized plasmonic resonances and array resonances has been discussed in much detail in the literature [112, 114–116, 118–122]. A similar concept of overlapping local and collective resonances was recently studied in the case of a plasmonic grating composed of deep resonant grooves [123]. However, we go further here and use these properties in complex non-uniform structures in order to engineer the near field excitation of particular

selected elements.

Fig. 10.2(a) shows the field enhancement of an isolated gold disc (in red) having a radius of 890 nm and a thickness of 70 nm. We observe a broad resonance with a maximum around $\lambda = 6.3\mu$m. For an infinite array of such discs, simulated by imposing periodic boundary conditions, we observe that for a period $\Delta = 4.3\mu$m all the fields scattered by the discs add constructively in phase, leading to the existence of a relatively long lived photonic mode manifested as the sharp blue resonance on Fig. 10.2(a). In other words, the array of discs is designed to form a second order grating that couples incident radiation into an in-plane collective photonic mode. We emphasize that there is no propagating surface plasmon involved in this work. The different discs are only weakly coupled through their near-field since their separation is large compared to their diameter. They interact through their scattered fields, emitted into a dipolar-like emission pattern. Because almost no field is scattered in the direction of polarization of the incident light, while maximum scattering occurs in the direction normal to the incident wave polarization, the collective excitation of the discs result in waves propagating in the direction normal to the polarization of the incident light, where constructive interference of the scattered fields occurs [112]. This is different from a plasmonic grating composed of grooves, where propagating surface plasmons are launched in the direction of incident polarization.

The frequency spectrum of the calculated field enhancement in a gold bow-tie antenna is shown on Fig. 10.2(b). The geometrical parameters considered are detailed in the caption. For an isolated antenna under direct illumination by a plane wave, a broad

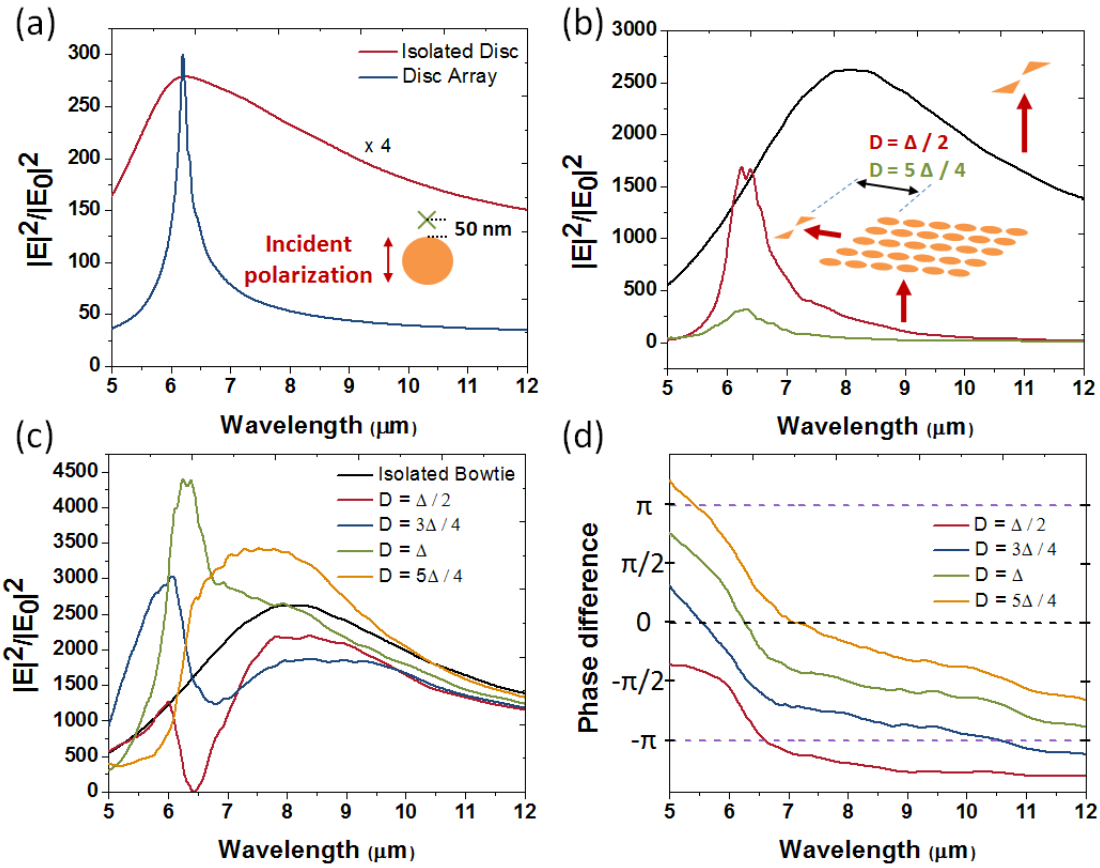

FIGURE 10.2: (a) Simulated field enhancement for gold discs with 890 nm radius and 70 nm thickness at the interface between a BaF_2 substrate and air. In red, an isolated disc, with intensity magnified 4 times; in blue, an infinite two-dimensional array of such discs with periodicity $\Delta = 4.3\mu$m. The near-field intensities are calculated 50 nm away from the disc edge, in the direction of the incident light polarization, as shown in the inset. We consider any arbitrary disc in the case of the infinite array as they are all equivalent. (b) Simulated field enhancement for a gold bow-tie antenna directly illuminated only by a plane wave (black) or illuminated only by the field scattered by the array of discs in (a), situated at a distance $D = \Delta/2$ (red) or $D = 5\Delta/4$ (green). The bow-tie is 70 nm-thick. Each arm is a section of disc with a radius of 2.2μm and an opening angle of 45°. The central gap is 100 nm wide. The insets represent the two excitation paths considered for the bow-tie antenna. (c) Simulated field enhancement at the center of the bow-tie gap, for an isolated bow-tie (black) and for the full structure as shown in Fig. 10.1(a), for different distances D between the bow-tie and the arrays of discs. (d) Phase differences between the two excitation paths of the bow-tie, as shown in the insets of (b), calculated at the center of the bow-tie gap, for different distances D between the bow-tie and the arrays of discs.

resonance is observed, with a maximum at $\lambda = 8\mu$m. Also shown on Fig. 10.2(b) is the field enhancement at the bow-tie gap when illuminated only by the field scattered by an array of discs similar to the one described above. As shown in the inset of Fig. 10.2(b), the plane wave in these latter simulations is incident only on the array while the bow-tie is illuminated only by the scattered field. This is made possible through the use of total-field/scattered-field boundaries [124] enclosing the array. We observe a large field enhancement corresponding to the scattering resonance of the array. Because of the diffraction of the scattered fields, the fields intensity at the bow-tie gap decreases with increasing distance between the array and the bow-tie (compare red and green curves).

We now assemble all these components to form the structure shown in Fig. 10.1(a). The two excitation paths for the bow-tie antenna, through direct illumination by the incoming plane wave (broad resonance), and through the fields scattered by the array of discs (relatively narrow resonance), give rise to a Fano-like interference phenomenon observed in the field intensity at the gap of the bow-tie antenna, as shown in Fig. 10.2(c). Depending on the distance D between the array and the bow-tie, and thus on the phase difference between the two excitation paths, either constructive or destructive interference occurs. In order to better illustrate that phenomenon, we plot in Fig. 10.2(d) the phase difference between the two excitation paths, as observed at the center of the bow-tie, for different distances D. Horizontal lines indicates the particular values 0, $-\pi$, and $+\pi$. As expected, whenever the phase difference vanishes, constructive interference occurs, leading to an increased intensity at the bow-tie gap. On the contrary, when the phase difference approaches $+/-\pi[2\pi]$, destructive interference is observed

with a complete suppression of the bow-tie excitation in the case of $D = \Delta/2$.

We note that on Fig. 10.2(d), the curve corresponding to the shortest distance to the array (red) is not parallel to the other curves because evanescent components from the discs are still important at this point. We also observe that the phase difference is not exactly equal to π between two curves separated by $\Delta/2$. This translates the fact that as the scattered waves exit the array and propagate toward the bow-tie antenna, their effective wavelength change. As a result, while the wavelength inside the array is equal to the periodicity Δ, so that the field scattered by two adjacent discs add up in phase, this is no longer verified outside the array.

10.4 Fabrication and far-field characterization

We fabricated the structure shown in Fig. 10.1(a) and performed far-field measurements. As explained below, these measurements illustrate an indirect manifestation of the interference phenomena occurring in the near-field between the two excitation paths for the bow-tie antenna and confirm our understanding of the physical phenomena at play in the structures studied here.

Fig. 10.1(c) and (d) shows scanning electron microscope (SEM) images of the structure represented in Fig. 10.1(a) and fabricated on a BaF_2 substrate using electron-beam (e-beam) lithography. As the substrate is electrically insulating, a thin layer (6 nm) of chromium (Cr) was deposited using e-beam evaporation after photoresist (poly-methyl methacrylate) spinning. Following e-beam exposure, the Cr layer is etched away and the

photoresist is developed. As the chromium etchant is in aqueous solution while BaF_2 is soluble in water, it is important to keep the etching time to a minimum. The gold patterns are then formed by e-beam evaporation of 70 nm of gold, followed by lift-off. As seen on Fig. 10.1(d), the gap of the bow-tie is well defined and has a width of ≈ 90 nm. In the fabricated structures, the bow-tie antennas are each flanked by two arrays of discs arranged in a square lattice with period $\Delta = 4.3\mu$m, and separated from the bow-tie by different distances D from $D = \Delta/2$ to $D = 5\Delta/4$. The arrays contain 15x15 discs each.

The far-field measurement setup is presented in Fig. 10.3 and consists of a Bruker Fourier-transform infrared (FTIR) spectrometer connected to an infrared microscope (containing only reflective optics). A particularity of the setup is the use of a knife-edge aperture inserted in a plane conjugate to the sample plane, which enables us to measure the far-field radiated from a specific rectangular area of the sample. Here we use it to measure the far-field radiated from a 6μm x 9.5μm area enclosing the central bow-tie antenna.

Fig. 10.4 shows the simulated transmission spectrum (red) through a single isolated bow-tie antenna, similar to the one described above. We observe a well-defined transmission dip at $\lambda \approx 7.2\mu$m. One could expect the transmission dip to be closer to the near-field intensity maximum ($\lambda \approx 8\mu$m), because this is where the material absorption and in-plane scattering are maximized. However, for the particular antenna design and the frequency range studied here, the dominant phenomenon explaining the transmission dip is the destructive interference between the directly transmitted light and the light

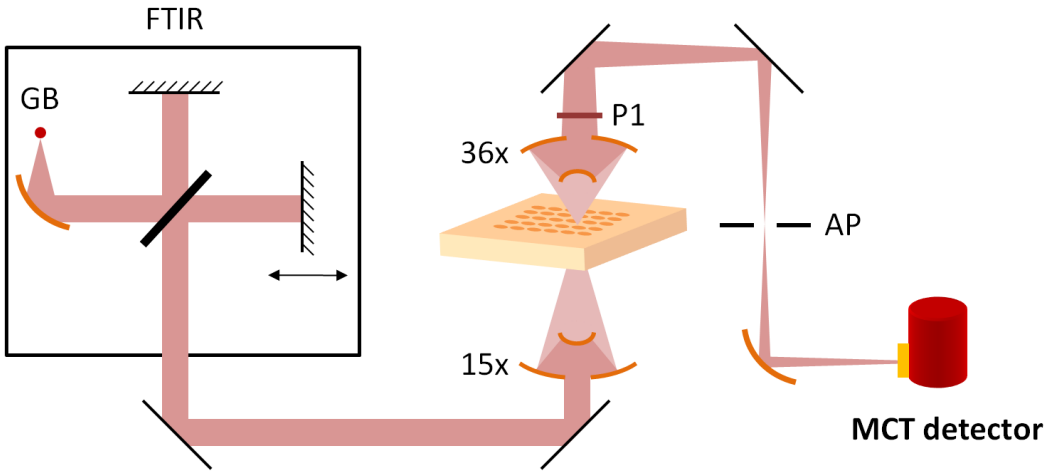

FIGURE 10.3: Schematic of the far-field characterization setup composed of a Bruker Vertex 70 FTIR spectrometer equipped with a Bruker Hyperion 2000 FTIR-microscope. The source of light is a globar (GB). One arm of the interferometer is focused on the sample with a 15x reflective (Cassegrain) objective (NA 0.4) and the transmitted/scattered light is collected with a 36x reflective objective (NA 0.5). A polarizer (P1) is inserted in the beam path. Light is then re-focused and a knife-edge aperture (AP) is inserted in the image plane to select only the light coming from a specific area. Finally, light is focused onto a liquid nitrogen cooled MCT detector. Not represented in the schematic are a set of two movable mirrors which introduce visible white light and extract a visible output toward a set of binoculars. This visible beam, overlapped with the infrared beam, enables the alignment and focusing of the sample. As the signal detected by the MCT is very small, special care is taken to obtain significant spectra. For all measurements, the spectra are averaged over 256 scans and we use a low scan speed (1 mm.s^{-1}) for the scanning mirror of the FTIR, in order to have more integration time on the detector for each point. We extract the signal from the MCT detector after its dedicated pre-amplifier and use a second external voltage pre-amplifier (20x) with a low-pass filter at 1 kHz. A low-pass Butterworth filter is applied on the final spectra to remove the high frequency noise and smoothen the curves.

scattered by the bow-tie. The position of maximum destructive interference, and hence of the transmission dip, is blue-shifted with respect to the near-field resonance for two main reasons: first the phase difference of the scattered field with respect to the incident field gets closer to π on the high-frequency side of the intensity resonance and second, the amplitude of the scattered field is expected to be peaked on the blue-side of the near-field peak [125]. The precise position of the transmission dip results from an interplay

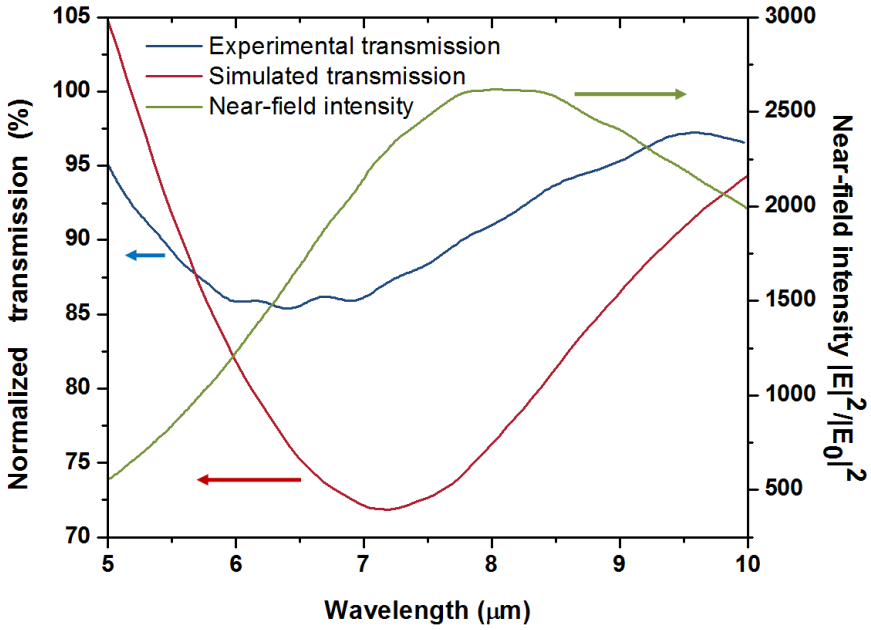

FIGURE 10.4: Simulated (red) and measured (blue) normalized transmission through a 6μm x 9.5μm area enclosing an isolated bow-tie antenna. The transmission curves are normalized to that obtained for the incident light polarized perpendicularly to the antenna axis. A rectangular monitor positioned 500 nm above the bow-tie and having the same dimensions as the knife-edge aperture is used in the simulation to calculate the transmission. (green) Simulated near field enhancement at the central gap of an isolated bow-tie antenna.

between phase and amplitude of the scattered light and directly transmitted light.

Also shown in Fig. 10.4 is the measured transmission spectrum (blue). Here, as in all our measurements (see Fig. 10.5), the transmission dips are systematically blue-shifted by $\approx 10\%$ of their expected position. We believe this blue shift stems from imperfect modeling of the frequency-dependant optical constants of the various materials in our system. The experimental transmission dip is shallower and broader than the simulated one, which we believe is mainly due to the fact that our illumination is not a plane wave, as in the simulations, but a focused beam collected with an objective having a finite numerical aperture.

All measured and simulated transmission curves are normalized to the transmission obtained for the incident light polarized perpendicularly to the antenna axis. This enables us to extract more selectively the part of the transmission that results from the interaction with the fields scattered by the bow-tie antenna near its LSP resonance. In particular, as shown in the inset of Fig. 10.4 (a), the aperture over which transmission is measured (red frame) may include some discs at small distances D between the bow-tie and the arrays. Transmission through this aperture thus also contains information on the interaction of the fields scattered by the discs with the directly transmitted light. Using the fact that the scattering properties of the discs are polarization insensitive, our normalization scheme enables to extract the transmission properties of the bow-tie antenna. We note that we cannot use, as an alternative solution, a smaller aperture in our experimental setup because the intensity impinging on the MCT detector would then be too low.

We now use the fact that the transmission dip results from an interference phenomenon to obtain information about the near-field intensity at the gap of the bow-tie through far-field measurements. Indeed, when the arrays of discs contribute to a stronger excitation of the bow-tie, the fields scattered by the bow-tie will be larger and thus the destructive interference will be stronger, resulting in a more pronounced transmission dip. On the contrary, when destructive interference occurs between the two excitation paths of the bow-tie, the intensity of the scattered light will be suppressed and a larger transmission is expected. These effects are clearly observed in the results of the simulations shown in Fig. 10.5(a), in reasonable agreement with the experimental spectra shown in Fig.

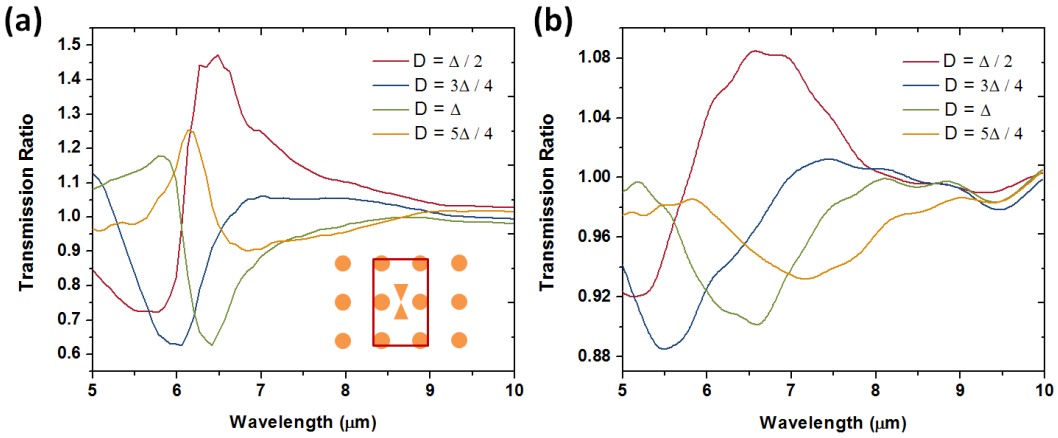

FIGURE 10.5: (a) Simulated transmission ratio for different distances D between the bow-tie and the arrays of discs. The reference is an isolated bow-tie antenna. The inset is a schematic representing the size of the aperture (red frame) with respect to the structure. Shown here is the case $D = \Delta/2$. (b) Experimental transmission ratio for different distances D between the bow-tie and the arrays of discs.

10.5(b).

The curves shown on Fig. 10.5 represent the ratio between the normalized transmission of the bow-tie embedded in the arrays of discs and the normalized transmission of an isolated bow-tie:

$$T_{ratio} = \frac{T^N_{embedded}}{T^N_{isolated}} = \frac{T_{embedded}}{T^{\perp}_{embedded}} / \frac{T_{isolated}}{T^{\perp}_{isolated}}, \tag{10.1}$$

where T_i^N is the normalized transmission, T_i denotes the transmission obtained for light polarized along the bow-tie antenna axis and $T_i^{\perp}$ the transmission obtained for light polarized perpendicularly to the bow-tie axis.

We observe a reasonable agreement between simulations and experiments. As discussed above, the experimental features are broader, shallower and systematically blue-shifted.

Compared to the case of an isolated bow-tie antenna, an additional factor contributes here to the increased width of the measured spectral features. Because the beam waist illuminating the sample has a diameter of $\approx 20\mu$m, only a few periods of the arrays are illuminated, leading to a broadening of the corresponding spectral features. As the distance D between the bow-tie and the arrays increases, the illuminated portion of the arrays decreases in size, resulting in the decreased depth and increased width of the measured spectral features observed in Fig. 10.5(b). Previous theoretical simulations of single-periodic grating-assisted antennas revealed that they are robust to disorder with random displacements of the particles up to 30% of the lattice spacing [120]. We thus do not expect fabrication-induced disorder to be contributing significantly to the observed discrepancies between experiments and simulations.

The measurements clearly show the existence of both dips and peaks in the transmission spectra, corresponding to either increased or decreased near-field excitation of the central bow-tie. They thus constitute a demonstration of the interference occurring between the two excitation paths for the bow-tie antenna. Furthermore, they confirm that the transmission dip observed is mainly the result of an interference phenomenon between the directly transmitted light and the light scattered by the bow-tie. In particular, the observed suppressed transmission caused by the presence of the arrays around the bow-tie can only be explained by the mechanism of destructive interference.

10.5 Multi-wavelength antenna and near-field imaging

Having experimentally proven the possibility of engineering and manipulating the coupling between the LSP resonance of the bow-tie antenna and the collective photonic-plasmonic resonance of the disc array, we proceed to design a more complex triple-band antenna, as shown in Fig. 10.6(a). It relies on the use of a single bow-tie antenna to provide a high field enhancement at its central gap, surrounded by arrays of discs with three different periodicities and disc diameters to concentrate light onto the bow-tie at three selected wavelengths. The arrays are arranged radially, thereby reducing the polarization sensitivity of the structure and making efficient use of the space surrounding the bow-tie antenna. The geometrical parameters of the structure are detailed in the caption of Fig. 10.6. We noticed in our simulations that the disc LSP resonance match with the collective array resonance when the disc diameter is roughly equal to half the array periodicity. Considering the large width of the discs LSP resonance, we chose this simple rule to design our structure. The distance between the bow-tie gap and the center of the first disc for each array is equal to an integer multiple of the array periodicity, in order to obtain constructive interference, as seen above. We note that in this work we use a bow-tie antenna as the central element, but any structure featuring a high near-field enhancement due to an LSP resonance could be used instead. In particular, replacing a bow-tie with a sharp metallic tip could provide a high field-enhancement in a volume that is more accessible to a sample to be measured [109].

We show in Fig. 10.6(b) the field enhancement obtained at the center of the bow-tie.

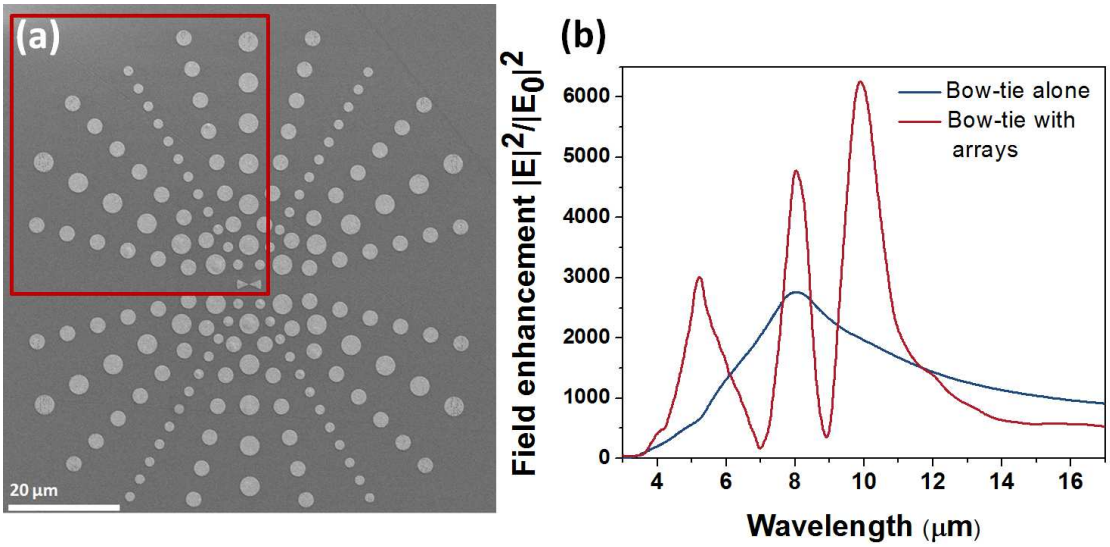

FIGURE 10.6: (a) SEM image of the fabricated triple-band antenna. The red frame indicates the area over which the near-field image in Fig. 10.8 is taken. The arrays periodicities are 3.6μm, 5.7μ?m and 7.2μm. The corresponding discs diameters are respectively 1.8μm, 2.85μm and 3.6μm, and the distances between the bow-tie gap and the center of the first disc are respectively 3.6μm, 11.4μm and 7.2μm. The bow-tie is composed of two sections of disc with radius 2.2μm and 45° opening angle. The central gap is 100 nm wide. All structures have a thickness of 70 nm and are deposited on a BaF_2 substrate. (b) Simulated field enhancement at the center of the bow-tie for the structure shown in (a) (red) and for an isolated bow-tie (blue).

We observe that at the three wavelengths corresponding to the scattering resonances of the three different arrays, the field enhancement in the bow-tie gap is increased as compared to that in the isolated bow-tie (blue). Additionally, we observe that intensity is strongly suppressed in between the enhanced peaks due to the destructive interference mechanism discussed above. We note that the three wavelengths of operation of our device are spanning more than one octave, which could open interesting applications using non-linear processes such as second-harmonic generation.

We imaged the near-field supported by the structure using the mid-infrared transmission-mode s-SNOM setup represented in Fig. 10.7. Transmission-mode s-SNOM [126] is

used to minimize near-field distortions by the probing tip and to provide a homogeneous illumination. The s-SNOM setup is based on a commercial atomic force microscope (AFM) (PSIA XE-120), previously used in [127]. The beam of a continuous-wave 10W CO2 laser emitting at $\lambda = 10.6\mu$m is first expanded (for safety reason) and then focused onto the sample, after significant atmospheric absorption. This attenuation is desirable because our source is too powerful and could otherwise damage the sample. The ZnSe lens used to focus the beam on the sample is chosen so that the focus size is on the order of the size of our antenna structure ($\approx 100\mu$m). A metal-coated AFM tip (Mikromash NSC19/Pt/AlBS) with resonant frequency of ≈ 90 kHz is then scanned over the sample in tapping mode, scattering the near-field into free-space propagating radiation collected by a set of ZnSe lenses and focused onto a liquid-nitrogen cooled Mercury-Cadmium-Telluride (MCT) detector. Lock-in detection at the second harmonic of the tapping frequency of the AFM tip was utilized to discriminate the scattered near-fields from the optical background that originated mainly from reflection and scattering of laser light from the tip shaft, the cantilever end, and the structure itself [128, 129].

Fig. 10.8 shows the measured SNOM signal as well as the FDTD simulation of the E_z component (perpendicular to the sample plane) of the electric field taken 10 nm above the gold structures. Only one quadrant is shown, corresponding to the red frame in Fig. 10.6(b), as information on the other quadrants is deduced by simple symmetry considerations. As expected, our metallic tip is sensitive mainly to the normal component of the electric fields (E_z). A large elastic scattering background can be seen in our SNOM image. It is both an amplitude background, resulting in the diffuse bright

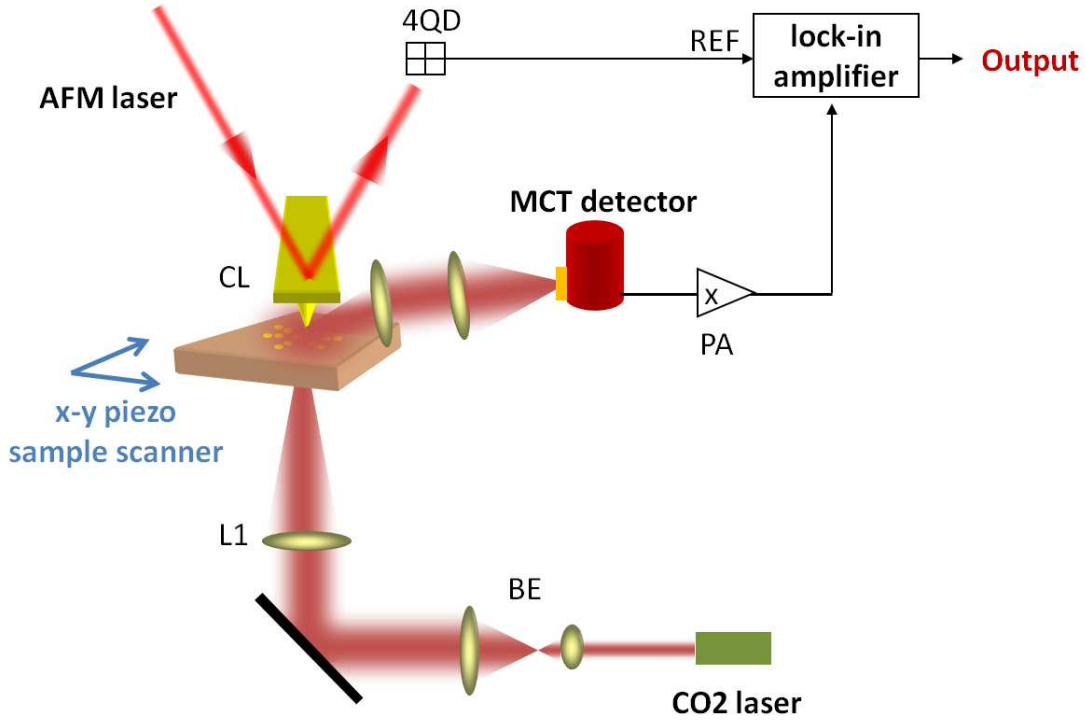

FIGURE 10.7: Schematic of the transmission mode s-SNOM used to image the near-field around the antenna. BE is a beam expender composed of two ZnSe lenses with respective focal lengths 0.5″ and 2″. L1 is a long focal length (3″) ZnSe lense, focusing the beam onto a $\approx 100\mu$m-diameter spot. CL is the AFM cantilever and tip. 4QD is the four-quadrant detector of the AFM monitoring the oscillation of the AFM tip. We used it as the reference signal for the lock-in amplifier. PA is the pre-amplifier of the liquid nitrogen cooled MCT detector.

spots spreading over the structure, and a phase background, resulting in the distortions of the measured near-field pattern. For example, the intensity minima crossing the discs are not always aligned along the vertical diameter but can be tilted and shifted because of interference between the scattered near-field and the background scattering [129]. Background suppression methods such as cross-polarization schemes [130] and pseudo-heterodyne detection [107] can be employed to reduce this spurious background

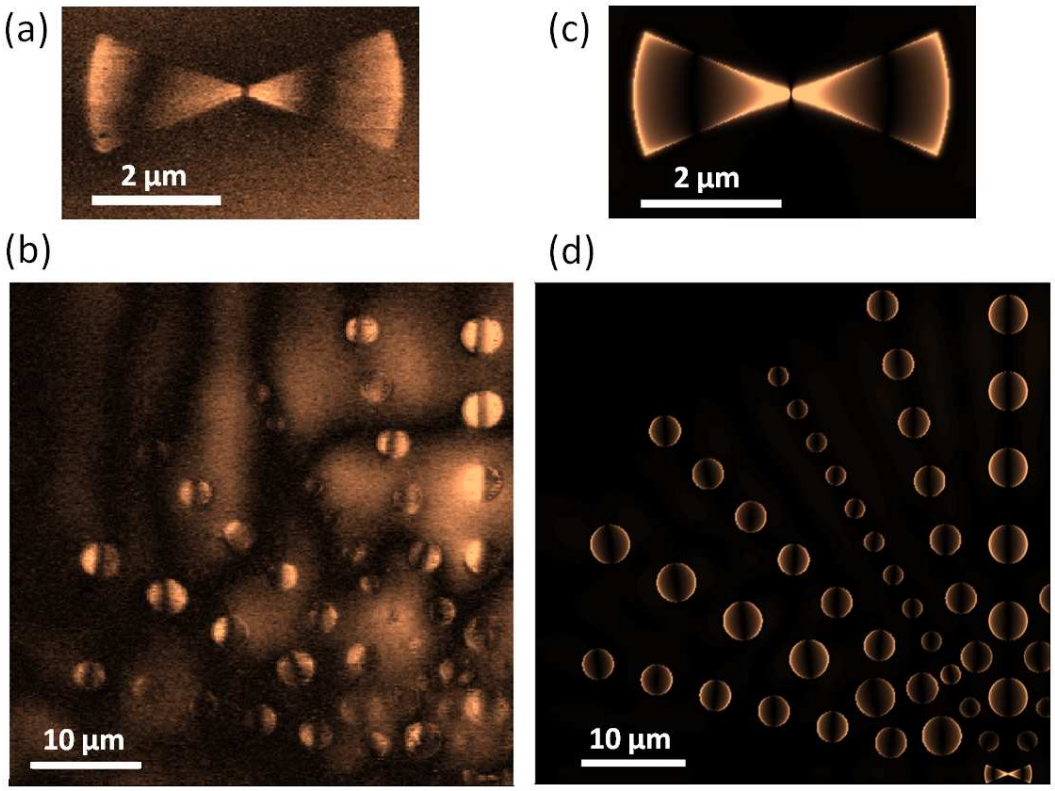

FIGURE 10.8: (a) and (b) Experimental near-field images of the fabricated antenna shown in Fig. 10.6(a). (c) and (d) Simulated E_z-component of the near-field monitored 10 nm above the gold structures.

which contains no useful information on the near-field distribution. However, as discussed in [131] even the state-of-the-art s-SNOM setups including all these background suppression techniques still suffer from these background issues. Considering the large dimensions of our scanning areas, the problem is even more serious and would require the development of novel techniques that are outside the scope of this paper.

However, the main features of the simulation are visible in the experimental data. Each disc has two high intensity lobes diametrically opposed in the direction of incident polarization, separated by an intensity minimum. The arrays with the largest discs, having a resonance frequency around $\lambda = 10\mu$m, are maximally excited, while the arrays of

smaller disks remain relatively dark. The field-enhancement contrast between the discs and the central bow-tie is not visible in Fig. 10.8, because only the E_z-component of the electric field is shown for the simulation results and our experiment meanly measures that same field component, while the stronger field component at the bow-tie gap is in-plane. Simulations indicate that when the total intensity is taken into account, the bow-tie gap is one to two orders of magnitude brighter than the discs edges. The structures thus conserve a high spatial resolution.

Importantly, the multi-band capabilities of our design opens the possibility to further increase the spatial resolution using nonlinear effects, since the central bow-tie gap is the only spot with high enhancement at multiple wavelengths. A sensing scheme relying on the simultaneous near-field enhancement of several wavelengths in a single nanoscale volume could be implemented using our antenna. More generally, plasmonic antennas capable of focusing light into a single sub-wavelength spot at multiple frequencies, potentially spanning more than one octave as shown here, can be used for a range of novel functions, including the resonant enhancement of both pumping and emission efficiency of nanoscale emitters, background-free sensing of optically trapped nanoparticles, broadband near-field imaging, Raman and fluorescence sensing of multiple molecular targets with nanoscale spatial resolution [110].

10.6 Conclusion

We have proposed and demonstrated a new antenna structure that provides high electric field enhancement at multiple wavelengths in a single nanoscale focal point. The structure uses the coupling between the LSP resonance of a central bow-tie antenna and the photonic-plasmonic modes of an array of resonant nanoparticles. A simplified design providing a high field enhancement at one selected wavelength was used to study this coupling, through FDTD simulations and far-field transmission experiments. Calculations and experiments confirmed the existence of Fano-like interference phenomena between the two excitation paths of the bow-tie, through direct illumination and through illumination by the scattered field of the surrounding nanoparticle arrays. The near-field of the proposed structures has been imaged using an s-SNOM setup, and the experimental data confirmed the possibility of simultaneous excitation of both the arrays photonic resonances and the central bow-tie nanoantenna. The work presented here gives insight into the interactions between local and collective plasmonic or photonic modes of complex antenna structures and paves the road to the development of broadband nanoantennas with high-spatial resolution that can be utilized as near-field probes for a variety of applications in nanoimaging, spectroscopy and biosensing.

Chapter 11

Modeling nanoscale V-shaped antennas for the design of optical phased arrays

11.1 Introduction

Optical devices modify the wavefront of light by acting on its phase and amplitude. At the core of many optical components is a spatially varying phase response, as illustrated by a simple lens, which has a parabolic phase profile. Most conventional optical components rely on light propagation over different optical lengths in order to create such a spatial phase response profile. However, it was recently shown [132] that abrupt phase changes over the scale of a wavelength can be introduced by using the phase response of

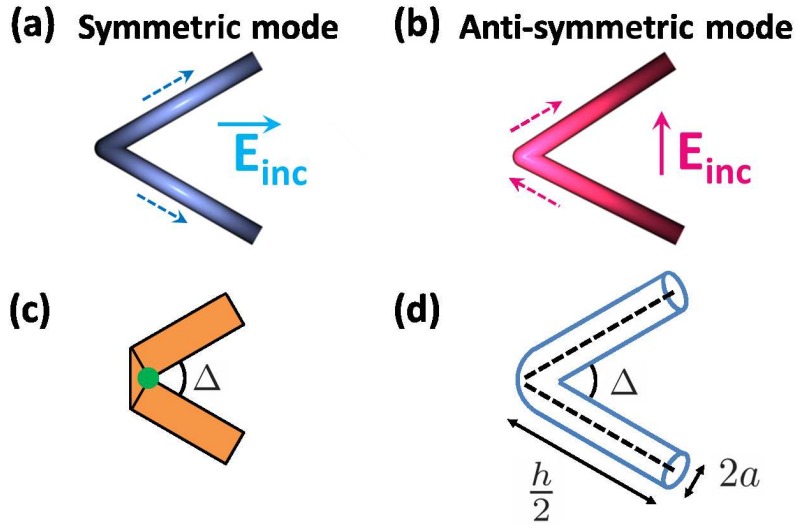

FIGURE 11.1: (a) and (b) Schematic of the first-order (a) symmetric and (b) anti-symmetric modes supported by a V-shaped antenna excited by an incident electric field polarized either (a) along the antenna symmetry axis or (b) perpendicular to the antenna symmetry axis. The arrows indicate the instantaneous direction of the current in each arm while the colored shading represents qualitatively charge density (the darker the more charges). (c) Schematic of a geometry used for FDTD simulations with $h = 1.2$ μm and $\Delta = 60°$. The rectangular arms are 200 nm wide and 100 nm thick. Antennas with different opening angle Δ are obtained by rotation about the connecting corners of the rectangular arms (green dot). The junction is formed by adding a triangular section. (d) Schematic of the geometry used for the Method of Moments calculations. Each antenna arm is modelled as a cylinder of diameter $2a$, but the geometry will be effectively reduced to that of a wire antenna (dashed line). The V-shaped antennas have an opening angle Δ and a total length h.

plasmonic resonators. While a single resonator is limited to providing a phase response with a maximum range of π, it was shown that an element consisting of two orthogonal resonators can provide arbitrary amplitude and phase response, covering the entire 2π range for the scattered light component polarized perpendicularly to the incident light [132].

In previous works [132, 133], nanoscale gold V-shaped plasmonic antennas supporting two plasmonic eigenmodes of opposite symmetry (Fig. 11.1 (a)-(b)), and thus acting as

two-oscillator systems, were used to provide adequate phase and amplitude control of light. Such V-shaped antennas can be used as the basic building blocks of a new class of flat optical components using phase discontinuities [132–134], since they enable the creation of arbitrary phase and amplitude masks with subwavelength 'pixel' size.

We present here the results of numerical solutions for the current distribution and scattered fields of V-shaped antennas, and in doing so obtain a detailed picture of their near- and far-field properties. In particular, we are able to accurately map their amplitude, phase and polarization responses in arbitrary directions. The convenient modeling tool presented here enables one to select and assemble various V-shaped antennas into more complex optical systems, in addition to giving detailed insight into the behavior of the antenna, illustrating for example the effects of near-field coupling between the two arms.

11.2 Method and approximations

Models describing the response of antennas have been extensively studied [135–138]. One of the main challenges is that the integral equations governing the behavior of antennas have no exact analytical solutions. However, with the development of numerical methods in the last few decades, we can obtain accurate numerical solutions in an efficient manner. This work is presenting how the Integral Equation Method of Moments (MoM) [136, 137, 139–141] can be used to study the behavior of V-shaped plasmonic antennas described by a Pocklington-type integral equation [142]. This numerical technique is very general and has been used to compute the characteristics of complex radio-frequency and microwave

antenna geometries [137]. The Pocklington equation is often used to determine the current distribution on cylindrical wires of small radius [136–138].

We study here how the methods and approximations used for long-wavelengths apply to the mid-infrared spectral range, where plasmonic properties play a significant role, by comparing our numerical results with the results of finite-difference time-domain (FDTD) simulations. We emphasize that we use a series of approximations to simplify the calculations as much as possible, effectively reducing the problem to one dimension. While full three-dimensional MoM simulation techniques could be implemented on our geometry, our main goal here was to propose a fast and efficient simulation method to probe a large design parameter space, bringing in the meantime radio-frequency methods to the attention of the plasmonics community. Since our numerical solution is one dimensional, it gives direct access to integral quantities such as the current distribution on the antenna, enabling straightforward interpretation of nanoantennas as circuit elements [143–145]. In contrast, three-dimensional FDTD simulations give access to a current density, whose integration into a one-dimensional quantity can be challenging, in particular at corners and edges. Finally, our method is approximately five orders of magnitude faster than FDTD simulations, enabling the accurate mapping of the properties of V-antennas over various geometric parameters.

The geometry considered is that of gold V-shaped antennas fabricated at the interface between a silicon substrate and air. Light is incident on the antenna from the silicon substrate. The antennas are 200 nm wide and 100 nm thick. For all the results presented, the incident wavelength is $\lambda_0 = 7.7$ μm. The two arms of the antennas have

equal length ($h/2$), in order to preserve the symmetry of the structure and thus simplify the understanding of the two orthogonal plasmonic modes. We note however that the calculation presented here could very easily be generalized to non-symmetric geometries. As shown in Fig. 11.1 (c), antennas with different opening angles are obtained by rotation of the rectangular arms about their connecting corners. While this exact geometry is simulated in our FDTD calculations, we use several approximations in our MoM calculations (see Fig. 11.1 (d)): (1) We assume the antennas to be cylindrical with a radius $a = 100$ nm. The optical properties of the antennas are moderately affected by the cross-section dimensions since they are much smaller than the length of the antenna. We verified that our results have limited dependence on the value of a chosen. (2) We use the thin-wire approximation ($a << \lambda$ and $a << h$, with a the antenna radius and h its total length) which enables us to consider the current distribution on the antenna to be purely axial and azimuthally invariant [136, 137], i.e. invariant for rotations around the antenna axis (see Appendix B). This approximation transforms the geometry studied to that of an infinitely thin antenna and thus enables to reduce the problem to an effective one-dimensional problem, which results in the dramatic increase observed for the computation speed. Information on the finite dimension of the cross section (radius a) is however preserved in our equations, in particular in the expression of the effective distance between two points of the antenna (see Appendix B). While fully justified at long wavelengths, this approximation may seem crude for mid-infrared antennas for which typically $\lambda/a \simeq 5$ and $h/a \simeq 10$. Our first concern will thus be to validate our results by comparing them with the results of well established simulation

tools. For this purpose, we use here FDTD simulations realized with a commercial software (Lumerical FDTD) as a reference. (3) We consider the antenna to be surrounded by a uniform medium with an effective index $n_{\text{eff}} = 2.6$. This value is such that the scattering resonance curve for a straight rod antenna embedded in a uniform dielectric of index n_{eff} overlaps with the scattering resonance curve of the same antenna located at an interface between silicon and air, both curves being obtained by FDTD simulations. Although imperfect, our approach offers the advantage to preserve simplicity and comparisons with FDTD simulations will show that it is accurate enough to guide the design of optical components, answering doubts expressed in the past that the numerical solution presented here would accurately handle wire antennas in a space partially filled with dielectric medium [146, 147], such as antennas defined on a dielectric substrate. (4) The finite conductivity of gold is taken into account in our calculations (details in the Appendix B) and is derived from the optical constants found in [98].

Our solution follows the outline of the derivation presented in [136] for the numerical integration of Pocklington's equation in the case of a straight cylindrical rod antenna. We first derive the integral equation governing the behavior of V-shaped cylindrical antennas, reduce the two-dimensional problem to one dimension, and implement a numerical solution based on the MoM. We first obtain the current distribution driven at the surface of the antenna by a known incident field. The far-field scattered by the antenna in any direction, with amplitude, phase and polarization information, is then calculated as the coherent sum of the fields scattered by a series of infinitesimal current elements

distributed along the antenna and having their amplitude and phase given by the current distribution, using an analytical expression for the radiation pattern of interfacial dipoles [148]. The numerical solution is detailed in the Appendix B.

11.3 Results

11.3.1 Comparison with FDTD

In order to compare our results with FDTD simulations, we calculated the far-field amplitude and phase of the scattered field, for different antenna lengths h, ranging from 0.6 μm (total length) to 3.2 μm, and different opening angles Δ, ranging from 0 to 180°. The antenna is illuminated by a plane wave coming at normal incidence with respect to the antenna plane. The details of the FDTD simulations are provided in the Appendix. In Fig. 11.2, we present the calculated amplitude and phase response of the V-shaped antennas, in the direction normal to the antenna plane, for an incident electric field oriented either along the symmetric ((a)-(d)) or anti-symmetric ((e)-(h)) plasmonic mode (see inset schematics).

We observe a very good agreement between FDTD calculations and our MoM calculations, demonstrating that our calculations give an accurate picture of the phase and amplitude response of nanoscale V-shaped antennas. Importantly, each point on the map is calculated in about 10 ms on a desktop computer using our method, compared to about 15 minutes for the corresponding FDTD simulation. In order to obtain the full map with 57x37 points, each corresponding to a different geometry and thus requiring

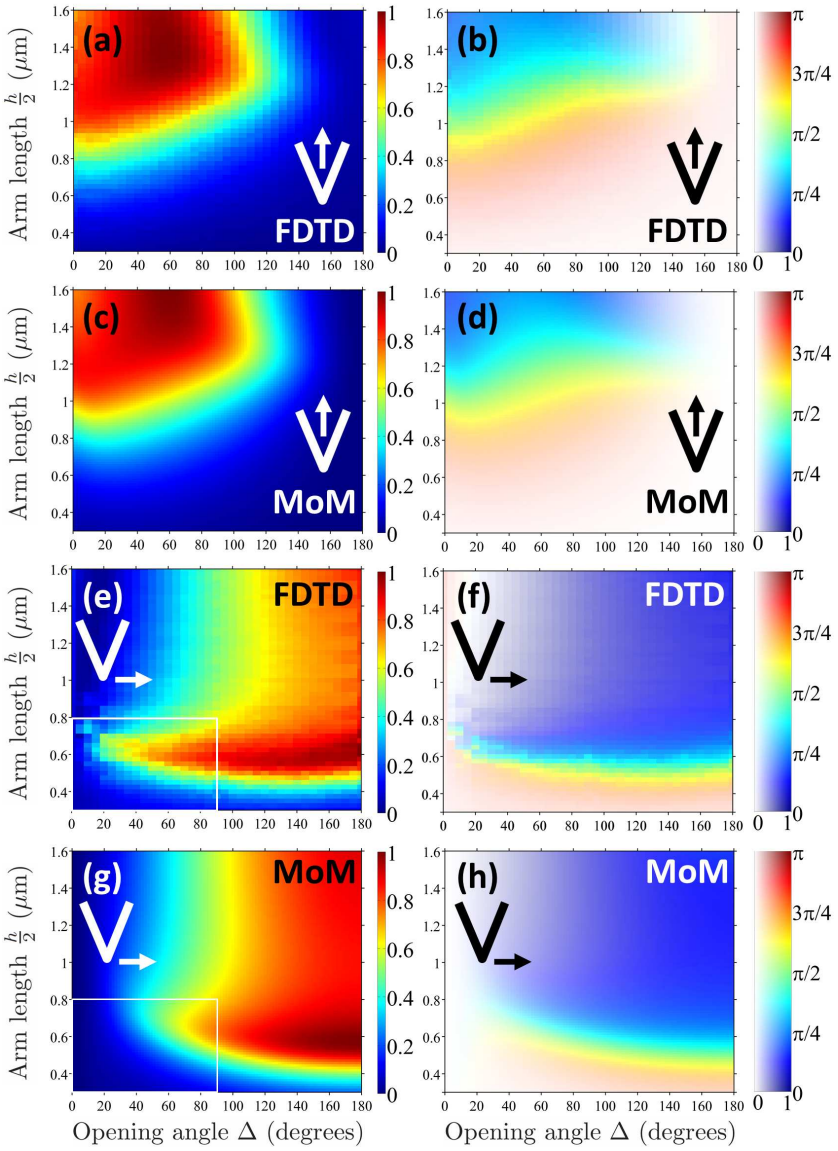

FIGURE 11.2: (a) and (c) (resp. (b) and (d)): Amplitude (resp. Phase) of the scattered field in the direction normal to the plane of the antenna, for an incident electric field oriented parallel to the symmetric mode (see insets and Fig. 11.1), obtained with FDTD calculations ((a) and (b)) and our MoM numerical solution ((c) and (d)), for different antenna geometries. (e)-(h) are similar to (a)-(d), but for an incident electric field oriented parallel to the anti-symmetric mode. Details of the FDTD simulations are provided in the Appendix B. For the phase plots, the colors encode the phase and we superposed a white mask whose transparency is proportional to the amplitude of the scattered field.A white frame is added in (e) and (g) to highlight the region where our approximations are least valid and where the main differences are observed between our MoM calculations and FDTD simulations. The FDTD maps have 57x37 cells, each corresponding to a different three dimensional simulation. The MoM maps have 100x100 cells.

a new three dimensional simulation, three weeks of computation is needed for FDTD, while only about 100 seconds is required with our method to obtain 100x100 points.

In the symmetric mode (Fig. 11.2 (a)-(d)), excited by an incident electric field parallel to the axis of symmetry of the antenna, the current distribution in each arm approximates that of an individual straight antenna of length $h/2$ and therefore the first-order antenna resonance occurs at $h/2 \simeq \lambda_0/(2.n_{\text{eff}})$ [149]. In the antisymmetric mode (Fig. 11.2 (e)-(h)), excited by an incident electric field perpendicular to the axis of symmetry of the antenna, the current distribution in each arm approximates that of one half of a straight antenna of total length h and the condition for the first-order resonance of this mode is $h \simeq \lambda_0/(2.n_{\text{eff}})$. These features can be observed in Fig. 11.2, where a maximum of the scattered field amplitude is observed when a resonance condition is satisfied. We also observe a phase shift of magnitude approximately equal to π across the resonances, as is expected across any resonance.

The scattered field amplitude vanishes for large (resp. small) opening angles Δ for a symmetric (resp. anti-symmetric) excitation, corresponding to the evolution of the scattering cross-sections with opening angle. We note that for the symmetric mode, the results from our numerical solution are still in very good agreement with FDTD for small Δ, where near-field interactions between the two arms are expected to be maximum. This suggests that distortions of the current distributions induced by coupling effect between the two arms are well accounted for in our numerical solution.

The scattering amplitude at small opening angles ($\Delta < 90°$) and close to the first anti-symmetric resonance (Fig. 11.2 (e) and (g), within the white frame), shows the main divergence between our calculations and FDTD simulations. This region (the lower left corner) corresponds to the region where the thin-wire approximation is the least valid since the arm length is only two to three times larger than the antenna diameter. We observe that the scattering amplitude decays faster in our MoM calculations than in FDTD simulations as the opening angle is reduced. The geometry simulated by FDTD (see Fig. 11.1 (b)) is such that there is always a significant portion of the antenna, in particular at the junction, that is oriented parallel to the anti-symmetric excitation (i.e. perpendicularly to the antenna symmetry axis). This is a result of the finite width of the arms. We thus expect a slow decrease of the scattering cross-section with decreasing opening angle. In contrast, the effective geometry considered in our MoM calculations is that of an infinitely thin wire. This effect is thus not taken into account and we expect the scattering cross-section to decrease faster with decreasing opening angles. In the rest of this work, we will leave out this region in our discussion of the results.

One could expect in a first order approximation that as the opening angle is reduced for a fixed antenna length, the resonance position does not move and only the scattering cross section is reduced. However, the 'tilted' shape of the symmetric resonance in Fig. 11.2 (a) and (c) suggests the opposite. The red-shift (resp. blue-shift) of the resonance as the opening angle is reduced for the symmetric (resp. anti-symmetric) mode is a result of the interaction between the two arms of the V-shaped antennas. Charges of similar (resp. opposite) signs accumulating at both extremities of the antenna contribute to a weaker

(resp. stronger) restoring force in the symmetric (resp. anti-symmetric) mode, and thus a red-shift (resp. blue-shift). We note that we use the expressions red- and blue-shift even though our results are for a fixed wavelength because we translate a resonance shifting to a longer (resp. shorter) antenna length as a blue-shift (resp. red-shift) of the resonance.

The polarization of the scattered radiation is the same as that of the incident light when the latter is polarized parallel or perpendicular to the antenna symmetry axis. However, for an arbitrary incident polarization, both antenna modes are excited with different amplitude and phase because of their distinct resonance conditions. As a result, the scattered light can have a different polarization from that of the incident light. In Fig. 11.3 (a) and (b), we show the amplitude and phase of the scattered field component polarized perpendicularly to the incident polarization, which is itself polarized at 45° with respect to the symmetry axis of the antenna. the plots are obtained with our MoM numerical solution. The two areas of highest amplitude correspond to the resonant excitation of either the symmetric or the antisymmetric mode. Across each of these resonances, a π phase shift is observed, so that overall a coverage of almost the full 2π range can be achieved [132].

In Fig. 11.3 (c) and (d), we show for comparison purposes the same quantities as in Fig. 11.3 (a) and (b), as obtained with FDTD simulations. The absolute differences between the results of the two calculation methods are shown in Fig. 11.3 (e) and (f), respectively for the amplitude and the phase of the cross-polarized scattered field. Except for the lower left corner already discussed above, the two methods are in agreement to within

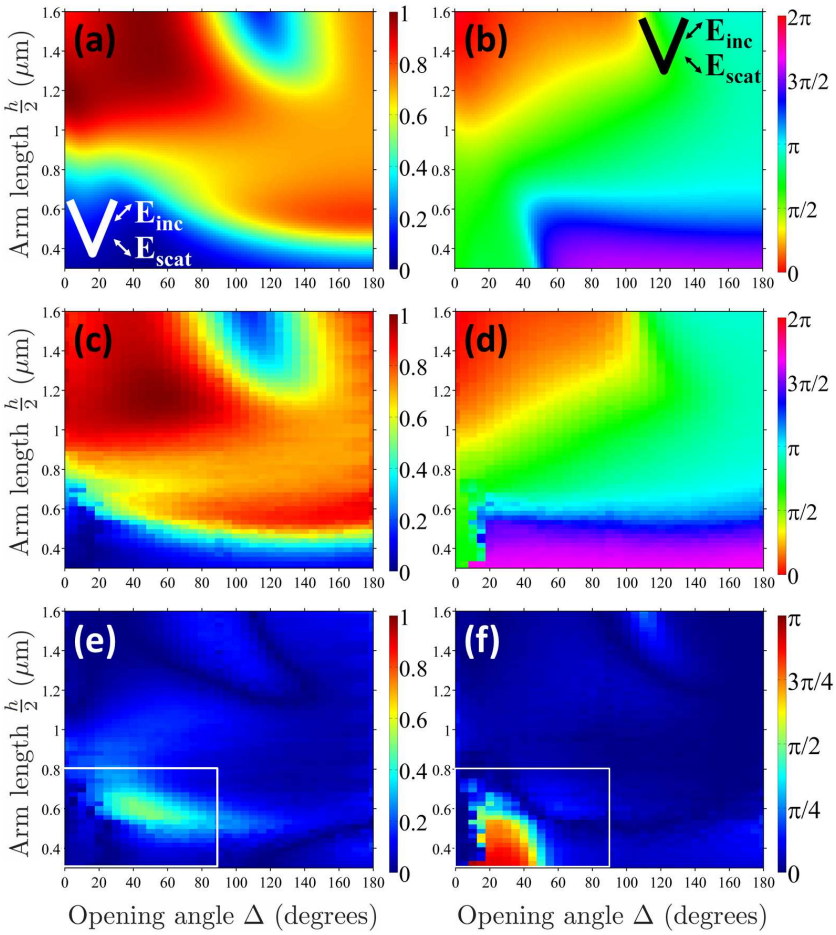

FIGURE 11.3: Amplitude ((a) and (c)) and Phase ((b) and (d)) of the scattered field component polarized perpendicularly to the incident polarization for different antenna geometries. The incident electric field is polarized at 45° with respect to the symmetry axis of the antenna. (a) and (b) are obtained with our MoM numerical solution while (c) and (d) are obtained with FDTD simulations. Details of the FDTD simulations are provided in the Appendix B. (e) and (f) correspond respectively to the absolute difference between (a) and (c) (amplitude) and (b) and (d) (phase). A white frame is added in (e) and (f) to highlight the region where the main differences are observed between our MoM calculations and FDTD simulations.

≈ 0.15 in amplitude, and $\pi/10$ in phase. These results demonstrate that resonant mid-infrared plasmonic antennas are within the domain of validity of our approximations. The errors observed (lower left corner) stem from distortions of the antenna response created by the finite width of the antenna. Provided the antenna geometry has a sufficient aspect ratio between the width and the length of the antenna, on the order of 1:4, such errors remain small.

Using the maps presented in Fig. 11.3 (a) and (b), one can quickly explore a large design-parameter space for V-shaped antennas, choose antennas with specific amplitude and phase response in the cross polarization, and assemble them to form an arbitrary phase and amplitude profile. For examples, for the phase-gradient plate used in [132], antennas with similar scattering amplitudes and regularly spaced scattering phases were chosen.

11.3.2 Current distribution

As mentioned above, we approximate the current to be purely axial. The current distribution is then fully described once given the complex value of the current as a function of the curvilinear coordinate running along the antenna length, as plotted in Fig. 11.4 for a constant antenna length $h = 2.4$ μm and for opening angles Δ varying from 30° to 180°. The π phase difference between the two arms for the symmetric mode (Fig. 11.4 (a)) indicates that the current flows in opposite direction in the two arms. We note here that we define the direction of the current with respect to the curvilinear coordinate orientation running from one end of the antenna to the other. There is a node of current

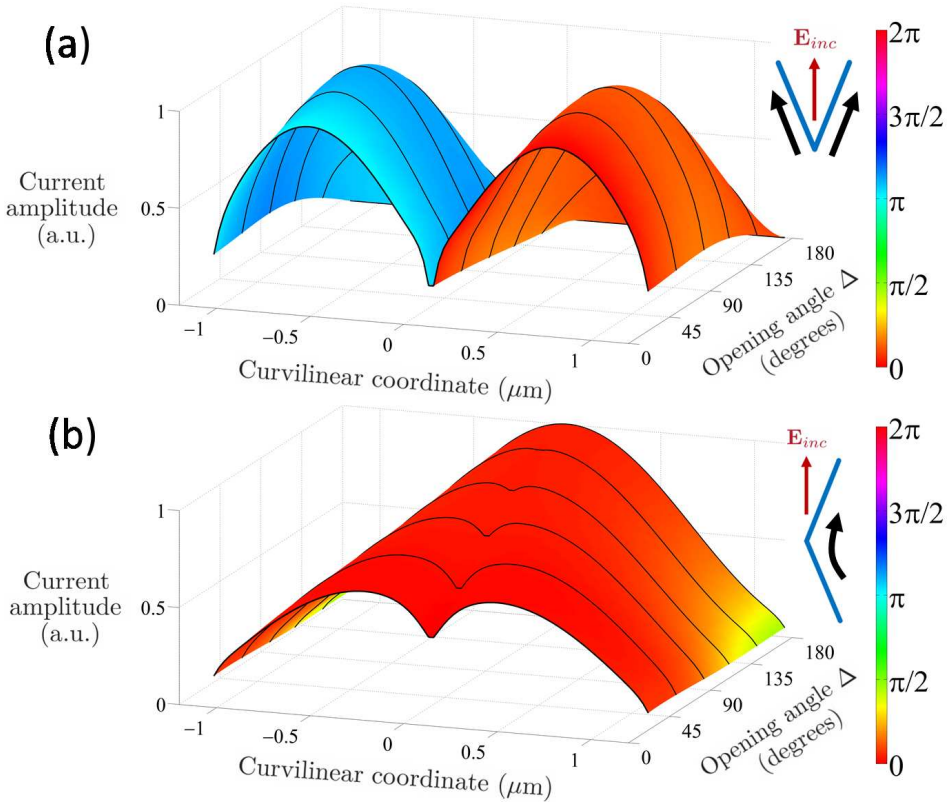

FIGURE 11.4: (a) Current distribution along an antenna of total length $h = 2.4$ μm for opening angles Δ from 30 to 180°. The incident electric field is polarized along the symmetric mode (see inset). The incident wavelength is $\lambda_0 = 7.7$ μm. The height indicates the amplitude of the current while the phase is given by the color. (b) is similar to (a), for an incident electric field polarized along the anti-symmetric mode (see inset). The black line are drawn at regular intervals of 30° in order to outline the amplitude variations of the current distribution. The position along the antenna is indicated by the curvilinear coordinate running along the antenna from one end to another, with its origin at the junction. Black arrows on the inset schematics of the antennas indicate the direction of the current in each arm for the symmetric and anti-symmetric modes.

at the center of the antenna. This agrees well with the picture of the symmetric mode being analogous to the mode supported by two parallel individual straight antennas of length $h/2$. In contrast, the asymmetric mode (Fig. 11.4 (b)) features a single lobe consistent with it being approximately equivalent to the mode of a single straight antenna of total length h.

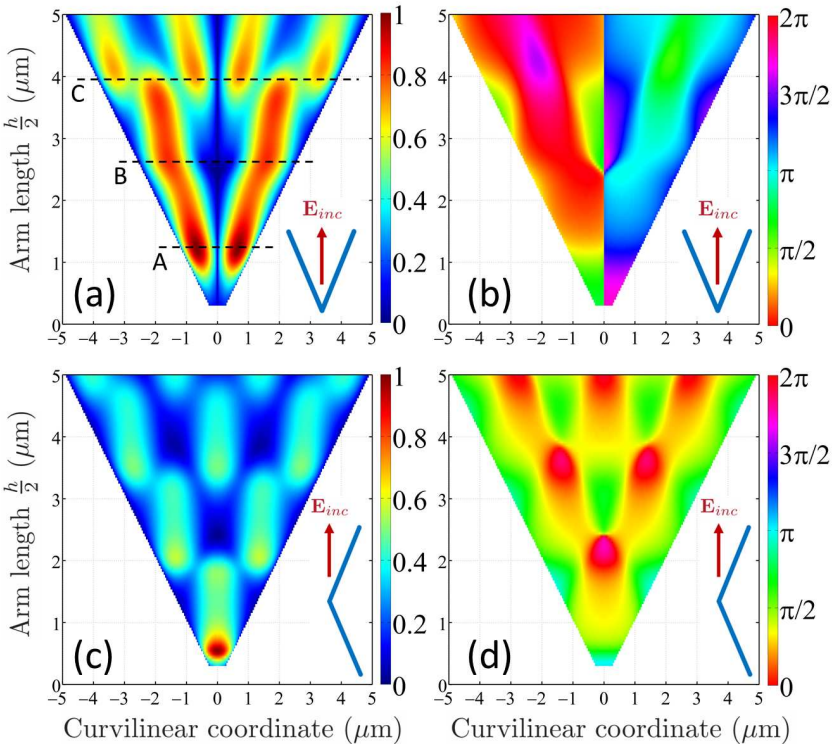

FIGURE 11.5: (a) Amplitude and (b) Phase of the current along an antenna with opening angle $\Delta = 45°$ and total antenna length varying from to 0.6 to 10 μm. The incident electric field is polarized along the symmetric mode. The incident wavelength is $\lambda_0 = 7.7$ μm. The labels A, B and C indicate the position of the first three resonances observed. (c) and (d) are similar to (a) and (b) for an incident electric field polarized along the anti-symmetric mode and for an opening angle $\Delta = 135°$.

The small distance between the two arms leads to near-field coupling translating into distortions of the current near the junction, especially for small opening angles. This is illustrated by the central dip which appears in the current distribution of the anti-symmetric mode for small opening angles. This feature can be easily understood since, for $\Delta < 90°$, the electric field radiated by the current in one arm opposes the current in the other arm. On the contrary, a small increase of the current near the junction can be observed for the symmetric mode (and for $\Delta < 90°$), since now the electric field radiated by one arm contributes to drive the current in the other arm.

Fig. 11.5 shows the current distribution along the antenna (with the position indicated by the curvilinear coordinate) for opening angles $\Delta = 45°$ ((a) and (b), with the incident electric field polarized along the symmetric mode) and $\Delta = 135°$ ((c) and (d), with the incident electric field polarized along the anti-symmetric mode) and different arm-lengths $h/2$. We can observe the appearance of the higher order modes with increasing length. For the symmetric mode (Fig. 11.5 (a)-(b)), the single lobe observed in each arm for $h/2 \simeq \lambda_0/(2.n_{\text{eff}})$ (A) splits into three lobes for $h/2 \simeq 3\lambda_0/(2.n_{\text{eff}})$ (C). This is again consistent with the picture of the symmetric mode being analogous to the mode supported by two parallel individual straight antenna of length $h/2$. Interestingly, we observe an intermediate resonance for $h/2 \simeq 2\lambda_0/(2.n_{\text{eff}})$ (B), whose excitation should be prohibited by symmetry considerations. The coupling between the two arms enables to couple energy into this mode. Other details of the current distribution indicate the effects of near-field coupling between the two arms, such as the asymmetry in the three-peak high-order pattern observed in each arm for $h/2 = 4$ μm (C): the side-lobe closer to the junction does not have the same shape as the one close to the extremity of the antenna. For the anti-symmetric mode (Fig. 11.5 (c)-(d)), the single lobe observed at $h \simeq \lambda_0/(2.n_{\text{eff}})$ splits into three (and then five, seven,...) lobes for h equal to odd integer multiples of $\lambda_0/(2.n_{\text{eff}})$, in agreement with it being approximately equivalent to the mode of a single straight antenna of total length h.

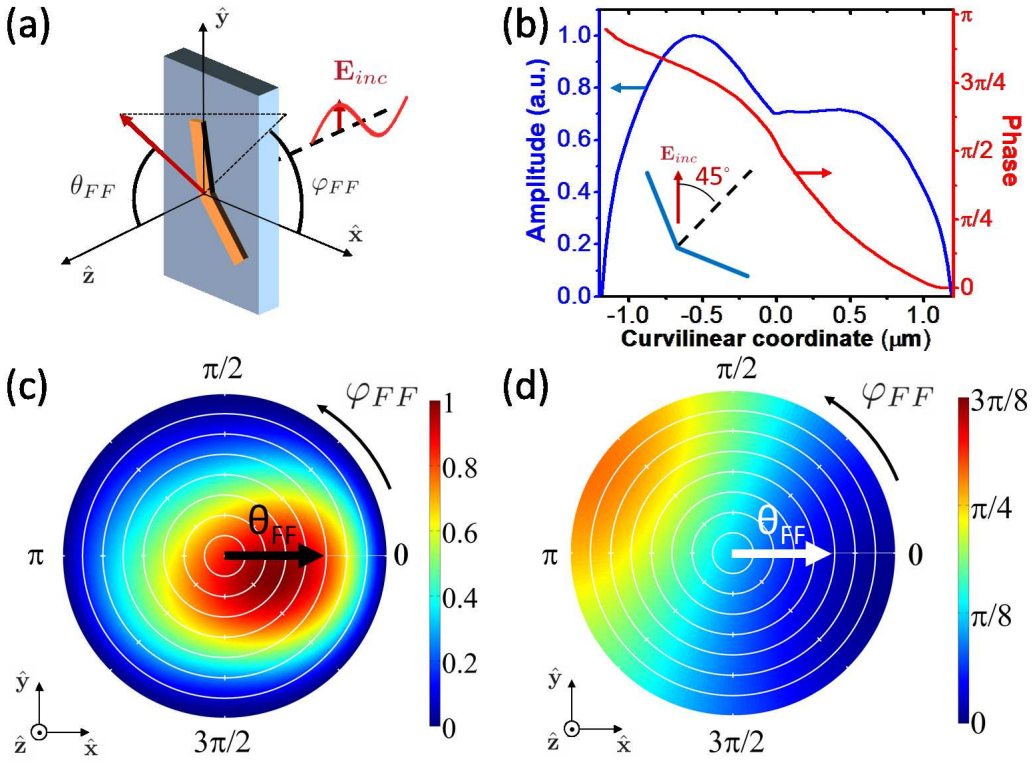

FIGURE 11.6: (a) Schematic with definition of the far-field coordinates ($\theta_{\rm FF}$, $\varphi_{\rm FF}$). The incident electric field is propagating along the z-axis and is polarized along the y-axis. The antenna is in the x-y plane. (b) Current distribution (amplitude and phase) for a V-shaped antenna with $\Delta = 135°$ and $h/2 = 1.2$ μm. The angle α between the symmetry axis of the antenna and the incident polarization is 45° (see inset schematic), in order to excite both symmetric and anti-symmetric modes. (c) Corresponding amplitude and (d) phase of the cross-polarized scattered field for different far-field coordinates ($\theta_{\rm FF}$, $\varphi_{\rm FF}$). The distance to the center of the plot is proportional to $\theta_{\rm FF}$, with $\theta_{\rm FF} = 0$ at the center and $\theta_{\rm FF} = \pi/2$ at the edge. The white circles represent values of $\theta_{\rm FF}$ regularly spaced from 0 to $\pi/2$. The azimuthal angle of the plot is equal to $\varphi_{\rm FF}$.

11.3.3 Far-field radiation pattern

We now study the far-field radiation pattern of a given V-shaped antenna with $\Delta = 135°$ and $h/2 = 1.2$ μm. The geometry and the definition of the far-field coordinates are represented in Fig. 11.6 (a) and the current distribution is shown in Fig. 11.6 (b). The angle α between the symmetry axis of the antenna and the incident polarization is 45°.

The current distribution is a superposition of a symmetric and an anti-symmetric mode, featuring two lobes reminiscent of the first order symmetric mode and a non-vanishing current at the junction as for the anti-symmetric modes.

In Fig. 11.6 (c), we show the amplitude of the cross-polarized scattered field. The far-field is calculated as the coherent sum of the far-fields radiated by infinitesimal current elements distributed along the antenna, having phase and amplitude following the current distribution plotted in Fig. 11.6 (b). The cross-polarized scattered field, i.e. the scattered field component resulting from a 90°-polarization conversion process, is obtained as the coherent sum of the fields radiated by the projections of these current elements on the x-axis. The information on the position of the current elements one relative to the other along the antenna is kept in order to calculate the interference of the fields radiated by different current elements. Note that the phase difference between the fields radiated by different current elements contains a geometric term as well as a term coming from the non-uniform phase of the current distribution along the antenna. We observe that the main lobe is not in the direction normal to the plane of the antenna, as a result of interference between the fields radiated by different sections of the antenna. The symmetry of the antenna is not preserved in the far-field since the incident electric field is not along one of the antenna symmetry or antisymmetry axis. The asymmetric amplitude and phase profile of the current distribution in Fig. 11.6 (b) also illustrates this point. The scattered intensity vanishes in all directions parallel to the antenna plane. This is a known result for dipoles located at an interface between two different dielectric media [148].

The phase of the cross-polarized scattered field is shown in Fig. 11.6 (d). It is interesting to observe that it is not constant, with variations on the order of $\pi/8$ over the main scattering lobe. A good knowledge of the amplitude and phase profile of the scattered field over the full half space is important to optimize optical components relying on the precise engineering of the scattering of the antennas at large angles, such as short focal-distance flat lenses.

11.4 Conclusion

In summary, using the Integral Equation Method of Moments, we presented an accurate and efficient numerical computation of the current distribution in V-shaped antennas excited by an electric field of arbitrary polarization. Using this information, we extracted the far-field phase, amplitude and polarization response of these elements in any direction. We demonstrated the accuracy of our numerical solution by comparing the results with FDTD simulations. The key element leading to the increased computational efficiency is the use of the thin-wire approximation which effectively reduces the problem to one dimension. This approximation necessitates aspect ratios of at least 1:4 between the width and the length of the antenna. We discussed details of the current distribution related to near-field coupling between the two arms of the antennas. The numerical method presented here enables a fast probing of the large design-parameter space of V-shaped antennas, that have been shown to be essential building blocks for optical elements relying on phase discontinuities [132].

Appendix A

Threshold gain simulation for external cavity quantum cascade lasers

A.1 Feedback from external mirror

The divergence of the uncollimated laser was measured with a microbolometer array placed directly in front of the laser facet (at a distance of 5 mm). The full-width half-maximum of the far-field intensity was measured to be respectively 36 and 73 degrees in the direction parallel and perpendicular to the epitaxial layers. Using these values, and assuming a Gaussian beam with its waist positioned at the laser facet, we can calculate the overlap between the laser waveguide core and the beam cross section after one

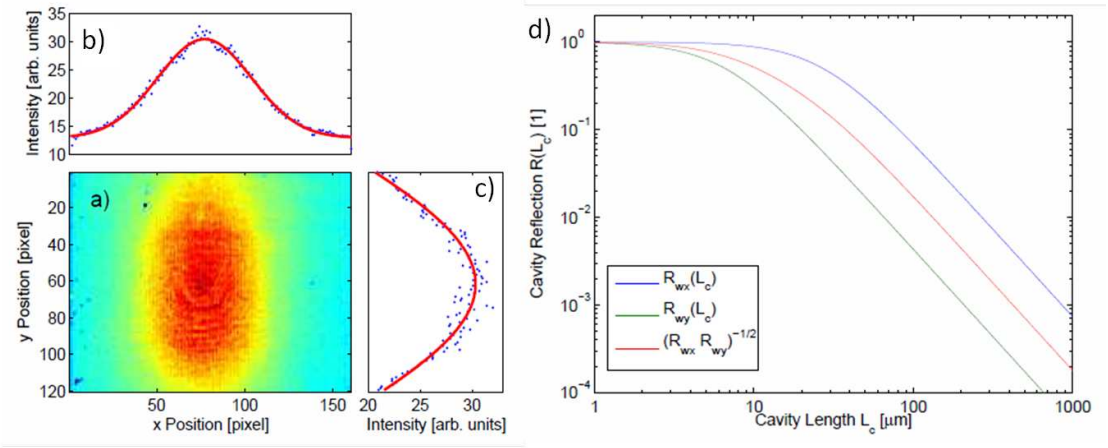

FIGURE A.1: (a) Far field of the multimode DFB laser as measured with a microbolometer array. The intensity profile through the intensity maximum is shown in (b)-(c), respectively for the direction parallel and perpendicular to the epitaxial layers. The intensity profile is averaged over five pixel lines and fitted to a Gaussian distribution. (d) Calculated single-pass external cavity reflectivity vs. Cavity length.

round trip in the external cavity. We thus obtain an estimate of the effective single-pass external cavity reflection, as shown in Fig. A.1.

In numerical calculations, we use these values as an effective reflectivity for the external mirror, and assume no propagation losses in the air-filled cavity.

A.2 Calculation method

We consider a one-dimensional multi-layer representation of the laser cavity (with distributed feedback grating), including an external cavity in some cases. The semiconductor material has gain, as well as waveguide losses of 10 cm^{-1}, while the external cavity is composed of air, assumed perfectly transparent. We assume that the laser operates on the fundamental transverse mode, and consider linearly polarized light. The laser

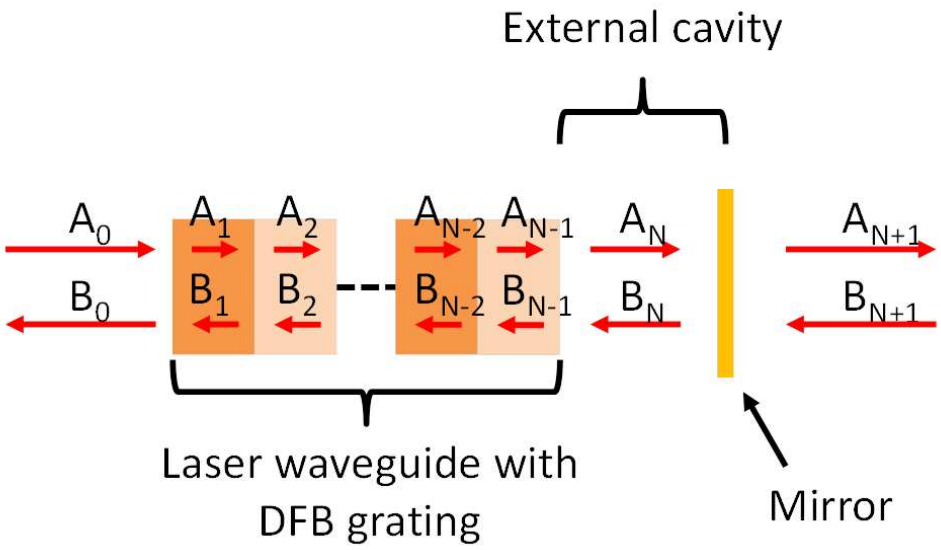

FIGURE A.2: Schematic of the one-dimensional transfer matrix model with notations.

is then described by a set of linear equations, expressed in matrix form by the transfer matrix formalism.

Using the notations shown in Fig. A.2 for the right- and left- propagating waves in the different layers, we obtain the following expressions:

$$\begin{bmatrix} A_0 \\ B_0 \end{bmatrix} = \begin{bmatrix} Q_{1,1} & Q_{1,2} \\ Q_{2,1} & Q_{2,2} \end{bmatrix} \begin{bmatrix} A_{N+1} \\ B_{N+1} \end{bmatrix} \tag{A.1}$$

In order to find the lasing modes and their threshold, we write a self-oscillating condition for which there can be an outgoing wave ($A_{N+1} \neq 0$) when there is no incoming wave ($A_0 = 0$) from outside the system:

$$\begin{bmatrix} 0 \\ \\ B_0 \end{bmatrix} = \begin{bmatrix} Q_{1,1} & Q_{1,2} \\ \\ Q_{2,1} & Q_{2,2} \end{bmatrix} \begin{bmatrix} A_{N+1} \\ \\ 0 \end{bmatrix} \Rightarrow Q_{1,1}(k,g) = 0, \tag{A.2}$$

where k is the wavenumber of the optical field and g is the material gain.

Solving the equation for the couples (k, g), we obtain the lasing frequencies and their threshold gain. As an example, we show in Fig. A.3 the results obtained for the multi-wavelength DFB QCL studied in this work, without external cavity, and with the cleaved facets placed exactly at the beginning and end of the grating (i.e. exactly at the interface between two unit cells).

Every blue dot corresponds to a different mode. The free spectral range corresponds to the laser waveguide length, assuming an average refractive index of 3.17. The thresholds of the longitudinal modes are modulated by the presence of the DFB grating. The five DFB resonances of interest are indicated by the red dashed lines.

The grating was designed so that the longitudinal modes with the lowest threshold (in the vicinity of the five DFB resonances) experience the same net gain, by balancing coupling constant and material gain. This is aimed at compensating for the finite bandwidth of the gain: the modes that lie on the side of the gain curve experience stronger feedback compared to the mode lying at the center of the gain curve [7]. Note that the correction for the finite bandwidth of the gain is not included in Fig. A.3.

Precise design requires precise knowledge of the gain curve. When studying the impact of different parameters (such as the position of the cleaved facets or the length of the

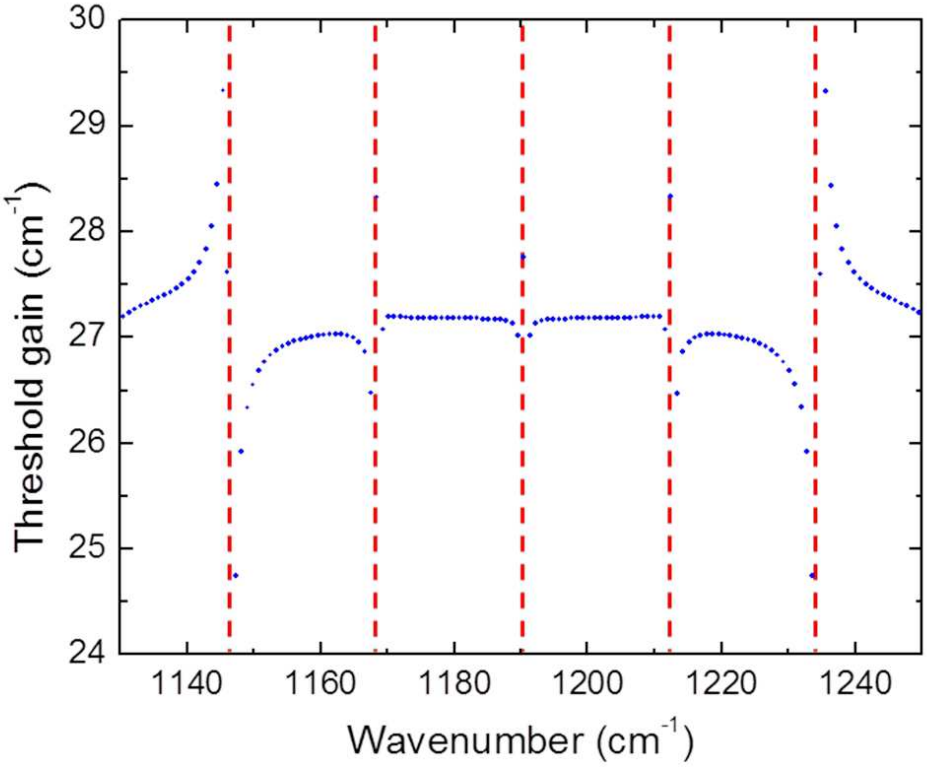

FIGURE A.3: Longitudinal modes of the multi-layer laser cavity with respective threshold gain. The positions of the five DFB modes of interest (i.e. lying within the gain region) are indicated with the red vertical dashed lines.

external cavity), we assume that the design is ideal and normalize the threshold curves obtained for the longitudinal modes closest to each one of the five DFB resonances of interest, such that the condition for identical net gain is reached in the case of perfectly positioned cleaved facets and in the absence of external feedback.

We then proceed to study the influence of a non-ideal cleaved facet position by adding a layer of high refractive index (3.18) at the end of the laser waveguide. This increases the lengths of the laser cavity and consequently shifts the comb of longitudinal modes, while the position of the DFB resonances remains fixed. As the longitudinal modes scan

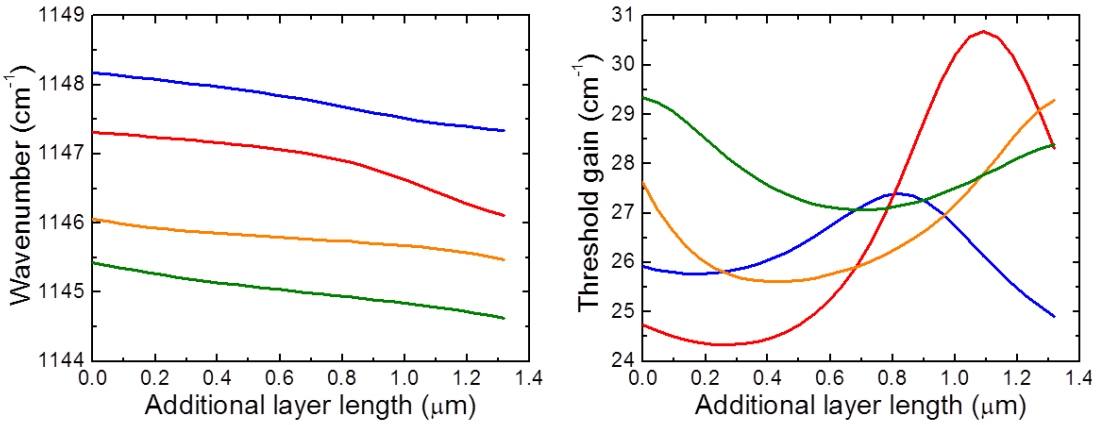

FIGURE A.4: Wavenumber and threshold gain of the four longitudinal modes closest to the first DFB resonance (left-most red dashed lines on Fig. A.3).

through the DFB resonances, their threshold is modulated. In order to find the lasing modes, we follow four longitudinal modes in the vicinity of each DFB resonance and track their wavenumber and threshold as the additional layer thickness is increased. Results are shown in Fig. A.4. We then obtain the curve of lowest threshold vs. additional layer thickness, indicating the mode that is the most likely to lase in the vicinity of each DFB mode and its threshold gain. After normalization (as mentioned earlier), we obtain the curve in Fig. 4.3 (b) in Chapter 4.

A similar procedure is used to obtain the gain threshold of the five DFB modes of interest as the external cavity length is varied.

Appendix B

Numerical details on V-shaped antenna modeling

B.1 General problem

Our solution is inspired by the derivation found in [136] of the numerical integration of Pocklington's equation in the case of a straight rod antenna. After deriving the integral equation governing the behavior of V-shaped antennas, we generalize the numerical solution to a two-dimensional problem.

We initially want to solve for the current distribution driven at the surface of the antenna by a known incident field $\mathbf{E_{inc}}$. By either assuming that the antenna is made of perfect electric conductor (PEC), or by modeling accurately the finite conductivity of a real metal, we obtain a relation between the incident and the scattered electric field $\mathbf{E_{scat}}$,

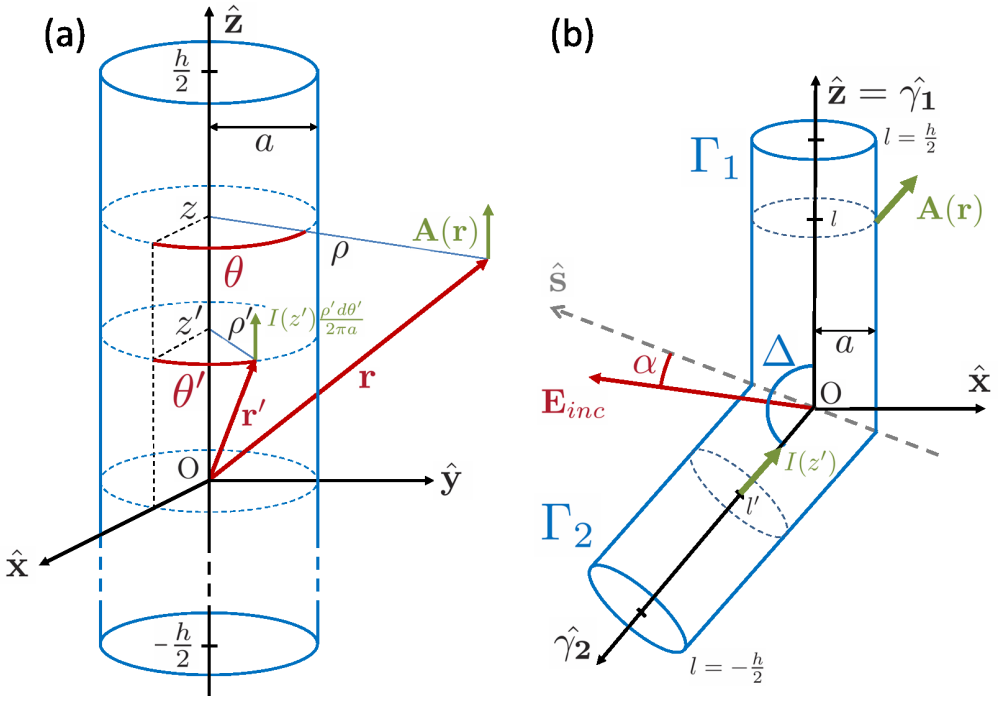

FIGURE B.1: (a) Schematic of a cylindrical antenna of radius a and total length h. We represented the vector potential $\mathbf{A}(\mathbf{r})$ at point $\mathbf{r}(\rho, \theta, z)$, radiated by the element of current $I(z')\frac{\rho' d\theta'}{2\pi a}$ at point $\mathbf{r}'(\rho', \theta', z')$. (b) Schematic of a V-shaped antenna with opening angle Δ. Note that the vector potential radiated by an element of current in one arm is not parallel to the other arm. The orientation of the antenna with respect to the incident electric field is defined by the angle α between the axis of symmetry of the antenna and the electric field polarization.

valid at the surface of the antenna. Using Maxwell's equations for the scattered field we further link the scattered field at the surface of the antenna and the current that radiates it. We thus finally obtain an integral equation expressing the scattered field as a function of the current distribution. Using a numerical method, we can then invert this equation and solve for the current. Once the current distribution is known, we are able to derive the electric field $\mathbf{E_{scat}}$ scattered by the antenna in all space (we initially only knew $\mathbf{E_{scat}}$ at the surface of the antenna) and thus infer the far-field response in amplitude, phase and polarization, in any direction. Fig. B.1 (a) describes the geometry

and defines the parameters used in the following derivation.

We start from Maxwell's equations to connect the scattered fields $\mathbf{E_{scat}}$ and $\mathbf{B_{scat}}$ to the current and charge sources [150]:

$$\nabla \cdot \mathbf{B_{scat}} = 0, \tag{B.1a}$$

$$\nabla \times \mathbf{E_{scat}} = -j\omega \mathbf{B_{scat}}, \tag{B.1b}$$

$$\nabla \cdot \mathbf{E_{scat}} = \frac{\rho}{\epsilon_0 \epsilon_\mathrm{r}}, \tag{B.1c}$$

$$\nabla \times \mathbf{B_{scat}} = \mu_0 \mathbf{J} + \frac{j\omega n^2}{c^2} \mathbf{E_{scat}} \tag{B.1d}$$

We assume here that the antenna is embedded in a uniform dielectric medium with refractive index $n = \sqrt{\epsilon_\mathrm{r}}$.

From Eqs. (B.1a) and (B.1b), we infer the existence of the magnetic and electric potentials $\mathbf{A}$ and φ satisfying:

$$\mathbf{E_{scat}} = -\nabla\varphi - j\omega \mathbf{A}, \tag{B.2a}$$

$$\mathbf{B_{scat}} = \nabla \times \mathbf{A} \tag{B.2b}$$

Substituting Eq. (B.2) and the Lorenz gauge $\nabla \cdot \mathbf{A} + j\omega\mu_0\epsilon_0\epsilon_\mathrm{r}\varphi = 0$ into Eqs. (B.1c) and (B.1d), we obtain the Helmholtz wave equation for the potentials:

$$\nabla^2\varphi + k^2\varphi = -\frac{\rho}{\epsilon_0\epsilon_\mathrm{r}} \tag{B.3a}$$

$$\nabla^2\mathbf{A} + k^2\mathbf{A} = -\mu_0\mathbf{J} \tag{B.3b}$$

where $k = \omega n/c$.

In order to find a solution to Eq. (B.3b), we introduce the Green function $G(\mathbf{r})$, solution of the Green problem $\nabla^2 G(\mathbf{r}) + k^2 G(\mathbf{r}) = -\delta(\mathbf{r})$, where δ is the Dirac delta distribution. In a three-dimensional space, the solution is given by $G(\mathbf{r}) = \frac{e^{-jk|\mathbf{r}|}}{4\pi|\mathbf{r}|}$. We then write the solution of Eq. (B.3b) as the convolution of $G(\mathbf{r})$ with the current source $\mu_0 J$:

$$\mathbf{A}(\mathbf{r}) = (G * \mu_0\mathbf{J})(\mathbf{r}) = \frac{\mu_0}{4\pi}\iiint_{\mathbb{R}^3} \mathbf{J}(\mathbf{r}')\frac{e^{-jk|\mathbf{r}-\mathbf{r}'|}}{|\mathbf{r}-\mathbf{r}'|}d\mathbf{r}' \tag{B.4}$$

For a rod made of a perfect electric conductor with vanishing skin depth, conservation of the tangential component of the electric field at the rod surface gives:

$$\hat{\mathbf{z}} \cdot (\mathbf{E_{scat}}(\rho = a) + \mathbf{E_{inc}}(\rho = a)) = 0, \tag{B.5}$$

where $\hat{\mathbf{z}}$ is a unit vector tangential to the antenna at the point where Eq. (B.5) is evaluated. In the case of a straight antenna, $\hat{\mathbf{z}}$ is parallel to the antenna axis. We study later how this relation is modified in the case of a real metal with finite conductivity. We consider the current to be limited to the surface of the rod ($\rho = a$). This is exact in

the case of a perfect electric conductor and represents an approximation in the case of real metals. Furthermore, using the thin-wire approximation ($a << \lambda$ and $a << h$), we can consider the current distribution $\mathbf{J}(\mathbf{r})$ to be axial and azimuthally invariant [147]. We can thus define the quantity $I(z)$ such that $\mathbf{J}(\mathbf{r}) = \hat{\mathbf{z}} I(z)\delta(\rho - a)\frac{1}{2\pi a}$. A sharp angle on the antenna, as in the case of the V-antennas discussed later, could break down this approximation. However, since a current element at one point affects the vector potential at another point with a magnitude decaying as the inverse of the distance between the two points (see Eq. B.4), the perturbation introduced by a sharp angle will remain local so that we can still consider the approximation valid along the entire antenna, except in the immediate vicinity of the junction.

We can now rewrite Eq. (B.4) as:

$$\begin{aligned} \mathbf{A}(\mathbf{r}) &= \frac{\mu_0}{4\pi} \iiint_{\mathbb{R}^3} \hat{\mathbf{z}}' I(z')\delta(\rho' - a)\frac{e^{-jk|\mathbf{r}-\mathbf{r}'|}}{2\pi a|\mathbf{r}-\mathbf{r}'|}\rho' d\rho' d\phi' dz' \\ &= \frac{\mu_0}{4\pi} \int_{-\frac{h}{2}}^{\frac{h}{2}} \hat{\mathbf{z}}' I(z') dz' K(|\mathbf{r}-\mathbf{r}'|), \end{aligned} \tag{B.6}$$

where we introduced the kernel $K(|\mathbf{r}-\mathbf{r}'|)$ as:

$$K(|\mathbf{r}-\mathbf{r}'|) \equiv \frac{1}{2\pi} \int_0^{2\pi} \frac{e^{-jk|\mathbf{r}-\mathbf{r}'|}}{|\mathbf{r}-\mathbf{r}'|} d\phi', \tag{B.7}$$

Additionally, substituting the Lorenz gauge in Eq. (B.2a), we obtain:

$$\mathbf{E_{scat}} = \frac{1}{j\omega\mu_0\epsilon_0\epsilon_r}[\nabla(\nabla \cdot \mathbf{A}) + k^2\mathbf{A}] \tag{B.8}$$

Writing this equation at the surface of the antenna, where we can express $\mathbf{E_{scat}}$ as a function of the known incident field $\mathbf{E_{inc}}$, we can solve Eqs. (B.6) and (B.8) for the current distribution I(z). Once the source current is known, we can determine $\mathbf{E_{scat}}$ in any point of space. Because we approximate the current as flowing only along a wire, we are only solving for a scalar quantity. Thus, solving a scalar equation is enough and we will use the projection of Eq. (B.8) on the tangent to the antenna at each point to obtain J.

Combining Eqs. (B.5), (B.6) and (B.8) leads to a Pocklington-type equation [142]. This equation has no exact analytical solution. However, it can be studied numerically. In order for the numerical solution to be tractable in a reasonable time, we use an approximation for the expression of the kernel defined in Eq. (B.7). Using again the thin-wire approximation, we can simplify the kernel by observing that the distance $|\mathbf{r} - \mathbf{r}'|$ is basically independent of ϕ' and, in the case of a straight antenna, approximately equal to $R_r = \sqrt{(z - z')^2 + a^2}$. We will refer to this simplified expression as the *effective* distance. We thus obtain the *reduced* kernel $K_r(z - z') = \frac{e^{-jkR_r}}{R_r}$. This approximation is valid as long as $|\frac{z-z'}{a}|$ is not too close to zero. Indeed, we notice that $K_r(0) = \frac{e^{-jka}}{a}$ whereas the exact kernal K diverges for $|\mathbf{r} - \mathbf{r}'| \to 0$. We will come back to this issue when explaining the details of our numerical solution.

B.2 V-shaped antennas

We now consider the case of a V-shaped antenna as represented is Fig. B.1 (b). The two arms of the antenna are Γ_1 and Γ_2, respectively in the directions $\hat{\gamma_1}$ and $\hat{\gamma_2}$. For convenience, we choose $\hat{\gamma_1}$ to be collinear to the $\hat{\mathbf{z}}$ axis. The angle between the two arms, oriented in the positive direction from $\hat{\gamma_1}$ to $\hat{\gamma_2}$, is Δ. We consider the curvilinear coordinate l along the antenna length, with origin at the junction point O, positive on Γ_1 and negative on Γ_2. For the sake of simplicity, we consider that the two arms have equal length $h/2$. However, the solution could be easily generalized to an asymmetric configuration with two different arm-lengths.

The effective distance between a current source at coordinate l' and the observation point (x, z) for the vector potential can be written as:

$$R_r(x, z, l', \Psi) = \sqrt{a^2 + (z + l' \cos(\Psi))^2 + (x - l' \sin(\Psi))^2}, \tag{B.9}$$

where $\Psi = \pi$ if l and l' are on the same arm, and $\Psi = \Delta$ otherwise. We note that the expression for a linear antenna is recovered by setting $\Psi = \pi$, $l' = z'$ and $x = 0$. The term a^2 comes from the thin-wire approximation. Using this effective distance, we can define a reduced kernel as introduced above: $K_r(x, z, l') = \frac{e^{-jkR_r}}{R_r}$. We consider here that the observation point is in the z-x plane of the antenna. This is justified by the thin-wire approximation for which azimuthal variation of the current on the wire surface is neglected. In other terms, we consider that the current is only a function of the curvilinear coordinate l.

Now that the problem is two dimensional, the vector potential radiated by an element of current at one point of the antenna is not always parallel to the antenna at another point. This represents the main challenge of the calculation presented here. In writing Eq. (B.8), cross derivatives now appear for the term $\nabla(\nabla \cdot \mathbf{A})$:

$$\nabla(\nabla \cdot \mathbf{A}) \cdot \hat{\mathbf{z}} = \left[\frac{\partial}{\partial z}(\frac{\partial}{\partial z} A_z + \frac{\partial}{\partial x} A_x) \right] \tag{B.10}$$

We can directly compute the expression $\frac{\partial}{\partial x} A_x$ from the analytical expression of A_x, written using the reduced kernel introduced above:

$$A_x(x,z) = \frac{\mu_0}{4\pi} \int_{-\frac{h}{2}}^{0} I(l') \frac{e^{-jkR_r(x,z,l',\Delta)}}{R_r(x,z,l',\Delta)} dl' (-\hat{\gamma_2}.\hat{\mathbf{x}}) \tag{B.11}$$

Note that only the current flowing in Γ_2 creates a non-vanishing component of $\mathbf{A}$ along the x-axis, hence the integration is limited to $[-h/2, 0]$. We then obtain:

$$\begin{aligned} \frac{\partial}{\partial x} A_x \big|_{x=0} \qquad & (x,z) = \\ & \frac{\mu_0}{4\pi} \int_{-\frac{h}{2}}^{0} I(l') \frac{e^{-jkR_r}}{R_r^3} (1 + jkR_r) \sin^2(\Delta) l' dl' \end{aligned} \tag{B.12}$$

We now write Eq. (B.8), evaluated in $x = 0$ and $z = l$, for all $l \in \Gamma_1$, using (B.6) and (B.12), and we obtain a Pocklington-type equation generalized to our two dimensional

problem:

$$\begin{aligned}\left[\frac{\partial^2}{\partial l^2}+k^2\right] \quad & \left(\frac{j\eta}{2\pi}\int_{-\frac{h}{2}}^{\frac{h}{2}} I(l')\tilde{K_1}(l,l',\Delta)dl'\right) \\ +\left[\frac{\partial}{\partial l}\right] \quad & \left(\frac{j\eta}{2\pi}\int_{-\frac{h}{2}}^{\frac{h}{2}} I(l')\tilde{K_2}(l,l',\Delta)dl'\right) \\ = \quad & 2kE_{\gamma_1}(l), \quad \forall l \in \Gamma_1 \end{aligned} \tag{B.13}$$

where:

$$\tilde{K_1}(l,l',\Delta) = -\frac{e^{-jkR_r(0,l,l',\Delta)}}{R_r(0,l,l',\Delta)}H(-l')\cos(\Delta) + \frac{e^{-jkR_r(0,l,l',\pi)}}{R_r(0,l,l',\pi)}H(l'),$$

$$\tilde{K_2}(l,l',\Delta) = \sin^2(\Delta)\frac{e^{-jkR_r(0,l,l',\Delta)}}{R_r^3(0,l,l',\Delta)}\left(1+jkR_r(0,l,l',\Delta)\right)l'H(-l')$$

The Heaviside function H (defined as $H(l)=1$, $\forall l \geq 0$ and $H(l)=0$, $\forall l<0$) was used to distinguish contributions to the vector potential $\mathbf{A}$ from Γ_1 ($l'>0$) and Γ_2 ($l'<0$), respectively. We introduced two reduced kernels $\tilde{K_1}$ and $\tilde{K_2}$ containing, respectively, the terms A_z (from both arms) and $\frac{\partial}{\partial x}A_x$ (only from Γ_2). The projection of the incident field $\mathbf{E_{inc}}$ on $\hat{\gamma_1}$ is used: $E_{\gamma_1}(l) = \mathrm{E_{inc}}\cos\left(\frac{\Delta}{2}+\alpha\right)$, where α defines the incident polarization (see Fig. 11.1 (c)). The constant $\eta = \sqrt{\frac{\mu_0}{\epsilon_0\epsilon_r}}$ is introduced.

Eq. (B.13) is valid for all points along Γ_1, i.e. it links the current distribution over

the whole antenna and the vector potential on the surface of Γ_1. We now obtain the second half of the equation ($l \in \Gamma_2$) by symmetry considerations ($\Delta \to -\Delta$, $I \to -I$, $l \to -l$ and $l' \to -l'$) and introducing the projection of the incident field on $\hat{\gamma_2}$, $E_{\gamma_2}(l) = \mathrm{E_{inc}} \cos\left(\frac{\Delta}{2} - \alpha\right)$:

$$\begin{aligned} \left[\frac{\partial^2}{\partial l^2} + k^2\right] \quad & \left(\frac{j\eta}{2\pi} \int_{-\frac{h}{2}}^{\frac{h}{2}} I(l') \tilde{K_1}(-l, l', \Delta) dl'\right) \\ - \left[\frac{\partial}{\partial l}\right] \quad & \left(\frac{j\eta}{2\pi} \int_{-\frac{h}{2}}^{\frac{h}{2}} I(l') \tilde{K_2}(-l, l', \Delta) dl'\right) \\ = \quad & -2kE_{\gamma_2}(l), \quad \forall l \in \Gamma_2 \end{aligned} \tag{B.14}$$

We used here the symmetry of our particular geometry to simplify the derivation. When treating asymmetric geometries, one has to rederive the equation governing the second arm, but the general idea of the derivation remains the same.

We can now gather Eqs. (B.13) and (B.14) into a single equation valid for all l in $\Gamma_1 \cup \Gamma_2$:

$$\begin{aligned} \left[\frac{\partial^2}{\partial l^2} + k^2\right] \quad & V^{(1)}(l) \\ + \left[\frac{\partial}{\partial l}\right] \quad & V^{(2)}(l) = 2kE(l), \quad \forall l \in \Gamma_1 \cup \Gamma 2, \end{aligned} \tag{B.15}$$

where $E(l) = E_{\gamma_1}(l)H(l) + E_{\gamma_2}(l)H(-l)$. We introduced:

$$\begin{aligned} V^{(1)}(l) \equiv \frac{j\eta}{2\pi} \int_{-\frac{h}{2}}^{\frac{h}{2}} I(l') \big[\quad & \tilde{K_1} \quad (l, l', \Delta) H(l) \\ - \quad & \tilde{K_1} \quad (-l, l', \Delta) H(-l) \big] dl' \end{aligned} \tag{B.16}$$

and

$$V^{(2)}(l) \equiv \frac{j\eta}{2\pi}\int_{-\frac{h}{2}}^{\frac{h}{2}} I(l')\big[\quad \tilde{K_2}\quad (l,l',\Delta)H(l) \\ +\quad \tilde{K_2}\quad (-l,l',\Delta)H(-l)\big]dl' \tag{B.17}$$

B.3 Numerical solution

As mentioned above, Pocklington's integral equation cannot be solved analytically. Here we extend the numerical solution presented in [136] to a two-dimensional problem.

The curvilinear coordinate $l \in [-\frac{h}{2}, \frac{h}{2}]$ is discretized into a vector $\mathcal{L} = [l_{-M}, l_{-M+1}, ..., l_M]$ with $N = 2M+1$ points spaced by a constant step D. We also define $\tilde{V}_n^{(i)} = V^{(i)}(l_n), i = 1, 2$ and $\tilde{E}_n = E(l_n)$.

The current $I(l)$ is expanded into a sum of basis functions B_n chosen here to be Dirac functions ($B_n(l) = \delta(l - l_n)$):

$$I(l) = \sum_{j=-M}^{M} \tilde{I}_j B_j(l) \tag{B.18}$$

We note that other basis functions could be chosen, such as triangular or sinusoidal functions. Choosing a basis of Dirac functions greatly simplifies the evaluation of the integral over l' in Eqs. (B.16) and (B.17). We obtain:

$$\tilde{V}_n^{(i)} = \sum_{j=-M}^{M} \kappa_{nj}^{(i)} \tilde{I}_j, \text{ or } \tilde{V}^{(i)} = \kappa^{(i)}\tilde{I}, \quad i = 1, 2 \tag{B.19}$$

where $\kappa^{(i)}$ are the reduced kernel matrices:

$$\kappa_{nj}^{(1)} = \frac{j\eta}{2\pi}\left[\tilde{K_1}(l_n, l_j, \Delta)H(l_n) - \tilde{K_1}(-l_n, l_j, \Delta)H(-l_n)\right]$$
$$\kappa_{nj}^{(2)} = \frac{j\eta}{2\pi}\left[\tilde{K_2}(l_n, l_j, \Delta)H(l_n) + \tilde{K_2}(-l_n, l_j, \Delta)H(-l_n)\right]$$

The thin-wire approximation used when introducing the reduced kernel is valid only as long as the distance between the integration point (l_j) and the observation point (l_n) is large enough compared to the radius a of the antenna. It is thus never valid for the diagonal terms for which $l_j = l_n$. While the exact kernel K diverges for $|\mathbf{r} - \mathbf{r}'| \to 0$, the reduced kernel K_r keeps a finite value. In order to reduce computation time, we set the value of the diagonal terms to $2K_r(0)$, so that the value of the diagonal term is about twice the value of the neighboring non-diagonal terms. This reproduces well the sharp divergence of the exact kernel. Although rather coarse, this approximation gives accurate results, as was confirmed earlier by comparison to FDTD simulations. More refined strategies have been developed to remove the singularity from the kernel in Pocklington's equation and may be of interest for the reader [151, 152]. With our approximation, the diagonal terms of the reduced kernel matrices become:

$$\kappa_{nn}^{(1)} = \frac{j\eta}{\pi}\left[\tilde{K_1}(l_n, l_n, \Delta)H(l_n) - \tilde{K_1}(-l_n, l_n, \Delta)H(-l_n)\right]$$
$$\kappa_{nn}^{(2)} = \frac{j\eta}{\pi}\left[\tilde{K_2}(l_n, l_n, \Delta)H(l_n) + \tilde{K_2}(-l_n, l_n, \Delta)H(-l_n)\right]$$

For all non-diagonal terms in the matrices $\kappa^{(i)}$ we empirically determined that we can safely use the reduced kernel expression, provided $\frac{D}{a} \geq 0.2$. As D is further reduced,

we observed that the solution becomes unstable since the 'discontinuity' we introduced by setting the value of the diagonal terms becomes sharper than the actual divergence of the exact kernel. A finer computation of the kernel for the terms neighboring the diagonal could be used for increased accuracy. However, our main purpose here is to develop a simple and fast modeling tool to probe a large parameter space so we used the approximate evaluation. In our numerical solution, the total length of the antenna is discretized in 90 points, so that the minimum step size D for the smallest antenna calculated is such that $D/a > 0.2$.

The first and second order derivatives in Eq. (B.15) are approximated by the following finite difference schemes (neglecting round-off error):

$$\begin{aligned} \frac{\partial^2}{\partial l^2} V^{(1)}(l)\big|_{l=l_n} &= \frac{\tilde{V}^{(1)}_{n+1} - 2\tilde{V}^{(1)}_{n} + \tilde{V}^{(1)}_{n-1}}{D^2} + \mathcal{O}(D^2) \\ \frac{\partial}{\partial l} V^{(2)}(l)\big|_{l=l_n} &= \frac{\tilde{V}^{(2)}_{n+1} - \tilde{V}^{(2)}_{n-1}}{2D} + \mathcal{O}(D^2) \end{aligned}$$

We can now write the discretized equation corresponding to Eq. (B.15):

$$\left[\mathcal{A}\kappa^{(1)} + \mathcal{C}\kappa^{(2)}\right] \tilde{I} = \mathcal{Q} d \tilde{E}, \tag{B.20}$$

where

$$\mathcal{A} = \frac{1}{D^2}\begin{bmatrix} 0 & 0 & 0 & 0 & 0 & \cdots & & & 0 \\ 1 & -2\alpha & 1 & 0 & 0 & \cdots & & & 0 \\ 0 & 1 & -2\alpha & 1 & 0 & \cdots & & & 0 \\ \vdots & & & \ddots & \ddots & \ddots & & & \vdots \\ 0 & & & \cdots & 0 & 1 & -2\alpha & 1 & 0 \\ 0 & & & \cdots & 0 & 0 & 1 & -2\alpha & 1 \\ 0 & & & \cdots & 0 & 0 & 0 & 0 & 0 \end{bmatrix},$$

with $\alpha = 1 - \frac{k^2 D^2}{2}$,

$$\mathcal{C} = \frac{1}{2D}\begin{bmatrix} 0 & 0 & 0 & 0 & 0 & \cdots & & & 0 \\ -1 & 0 & 1 & 0 & 0 & \cdots & & & 0 \\ 0 & -1 & 0 & 1 & 0 & \cdots & & & 0 \\ \vdots & & & \ddots & \ddots & \ddots & & & \vdots \\ 0 & & & \cdots & 0 & -1 & 0 & 1 & 0 \\ 0 & & & \cdots & 0 & 0 & -1 & 0 & 1 \\ 0 & & & \cdots & 0 & 0 & 0 & 0 & 0 \end{bmatrix},$$

and

$$\mathcal{Q} = \begin{bmatrix} 0 & 0 & 0 & 0 & \cdots & & 0 \\ 0 & 1 & 0 & 0 & \cdots & & 0 \\ 0 & 0 & 1 & 0 & \cdots & & 0 \\ \vdots & & & & \ddots & & \vdots \\ 0 & & \cdots & & 0 & 1 & 0 & 0 \\ 0 & & \cdots & & 0 & 0 & 1 & 0 \\ 0 & & \cdots & & 0 & 0 & 0 & 0 \end{bmatrix},$$

and $d = 2k$.

Matrices $\mathcal{A}$, $\mathcal{C}$ and $\mathcal{Q}$ are square N by N matrices. Note that $\mathcal{Q}$ represents the projection on the interior of the antenna, i.e. excluding the two end-points. We added a first row and a last row of zeros in the matrices $\mathcal{A}$, $\mathcal{C}$ and $\mathcal{Q}$. These rows do not add any equation and ensure that the finite difference schemes are defined for $n = \pm M$. At this point, Eq. (B.20) represents a system of $N-2$ equations for N unknowns (the N components of the vector $\tilde{I}$). It is therefore not invertible. However, two unknowns are given by the boundary conditions: $I(\frac{h}{2}) = I(-\frac{h}{2}) = 0$, or in matrix form: $(\mathbb{I}_N - \mathcal{Q})\,\tilde{I} = 0$, where $\mathbb{I}_N$ is the N by N identity matrix. We can finally write the discretized Pocklington equation as:

$$\left[\mathcal{A}\kappa^{(1)} + \mathcal{C}\kappa^{(2)}\right] \mathcal{Q}\tilde{I} = \mathcal{Q}d\tilde{E}, \tag{B.21}$$

Introducing $\bar{\bar{\mathcal{Z}}} \equiv \left(\left[\mathcal{A}\kappa^{(1)} + \mathcal{C}\kappa^{(2)}\right]\mathcal{Q}\right)_{\substack{2\leq n\leq N-1 \\ 2\leq j\leq N-1}}$, $\bar{I} = \tilde{I}_{2\leq n\leq N-1}$ and $\bar{E} = \tilde{E}_{2\leq n\leq N-1}$, Eq. (B.21) takes the form:

$$\left[\begin{array}{c|c|c} 0 & 0 & 0 \\ \hline 0 & \bar{\bar{\mathcal{Z}}} & 0 \\ \hline 0 & 0 & 0 \end{array}\right] \left[\begin{array}{c} 0 \\ \hline \bar{I} \\ \hline 0 \end{array}\right] = d \left[\begin{array}{c} 0 \\ \hline \bar{E} \\ \hline 0 \end{array}\right]$$

We can thus reduce the system to $N-2$ equations for $N-2$ remaining unknowns (the $N-2$ components of the vector $\bar{I}$), from which we can calculate the discretized current distribution:

$$\bar{I} = d\bar{\bar{\mathcal{Z}}}^{-1}\bar{E} \tag{B.22}$$

B.4 Modeling real metals

We have so far assumed that the antenna is made of perfect electric conductor. This assumption was only used in order to derive Eq. B.5, i.e. the relation between the incident and the scattered electric field at the surface of the antenna. In the case of real metals, the boundary condition is modified with the introduction of a finite conductivity, and using Ohm's law, we obtain at the surface of the antenna [150]:

$$\begin{aligned} &\mathbf{E}_{\|}(\rho = a) = \\ &\hat{\mathbf{z}} \cdot (\mathbf{E_{scat}}(\rho = a) + \mathbf{E_{inc}}(\rho = a)) = \frac{1-j}{2\pi a}\sqrt{\frac{\mu_0\omega}{2\sigma}}I, \end{aligned}$$

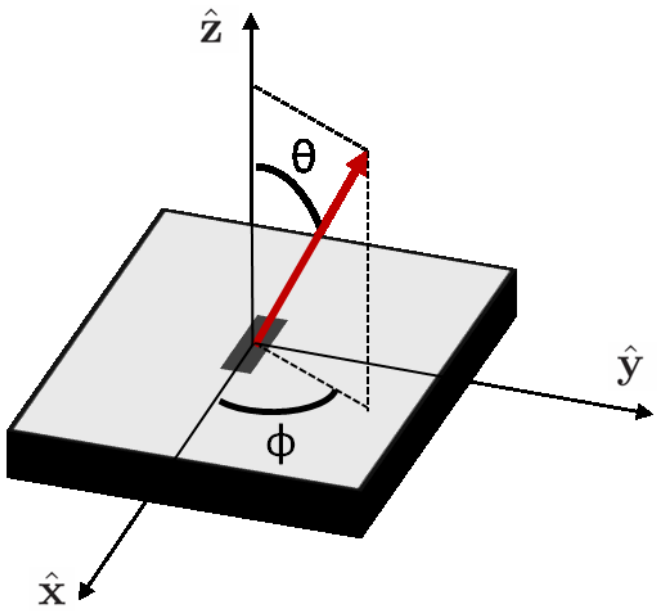

FIGURE B.2: Schematic of an infinitesimal horizontal electric dipole located at an interface between air ($z > 0$) and a dielectric medium ($z < 0$) of refractive index n.

where μ_0 is the magnetic permeability and σ is the AC conductivity of the real metal, derived from the optical constants found in [98]. Equation (B.22) is thus still correct provided the matrix $\bar{\bar{\mathcal{Z}}}$ is changed to $\bar{\bar{\mathcal{Z}}} + dz_{\text{int}}\mathbb{I}_{N-2}$, with $z_{\text{int}} = \frac{1-j}{2\pi a}\sqrt{\frac{\mu_0\omega}{2\sigma}}$.

B.5 Far-field calculation

Once the axial current distribution along the antenna is known, we can calculate the scattered far-field. We approximate the far-field radiated by the antenna as the coherent sum of the fields radiated by a series of infinitesimal current elements distributed along the antenna and having amplitude and phase given by the current distribution solved for. We use an analytical expression for the radiation pattern of an infinitesimal electric

dipole located on the plane interface between two dielectric half spaces (air and a medium of refractive index n) [148]. For the case of a dipole lying horizontally along the interface, the radiated field components in air are [148]:

$$\begin{aligned} E_\theta = \quad & \kappa\Big[\frac{\cos^2\theta}{\cos\theta+(n^2-\sin^2\theta)^{1/2}} - \sin^2\theta\cos\theta \\ & \cdot\frac{\cos\theta-(n^2-\sin^2\theta)^{1/2}}{n^2\cos\theta+(n^2-\sin^2\theta)^{1/2}}\Big]\cos\phi\frac{e^{ik_0r}}{r}, \\ E_\phi = \quad & -\kappa\frac{cos\theta sin\phi}{cos\theta+(n^2-\sin^2\theta)^{1/2}}\frac{e^{ik_0r}}{r}, \end{aligned}$$

where the angles θ and ϕ are defined in Fig. B.2.

B.6 FDTD simulation details

FDTD simulations realized using a commercial software (Lumerical FDTD) are used to validate our numerical solution. A realistic geometry is simulated, corresponding to fabricated V-shaped antennas [132]. Both arms have a rectangular cross-section, 200 nm wide and 100 nm thick. The antennas are defined on a silicon substrate. The interface between silicon and air lies at the center of the simulation area, which spans 4.5 μm x 4.5 μm x 6 μm (width x depth x height). Perfectly Matched Layers (PML) enclose the simulation area. The mesh cells are 30 nm x 30 nm x 15 nm in size in the plane of the antenna and within a 300 nm-thick layer encompassing the silicon-air interface (and the 100 nm-thick antenna itself). Beyond this layer, the vertical dimension of the mesh cells (height) is gradually increased to about 280 nm in air and 90 nm in silicon (or about $1/25^{th}$ of the wavelength in the medium). The simulation is stopped when

an auto shutoff condition is reached corresponding to the fields in all cells being smaller than $10^{-5}E_0$, where E_0 is the incident electric field amplitude. The time step is smaller than 0.037 fs. The optical constants are obtained by fitting the values found in Palik [98] to a multi-coefficient model.

We use a Total-Field Scattered-Field (TFSF) plane wave source encompassing the antenna. The dimensions of the total field region are 4.2 μm x 4.2 μm x 4 μm. The plane wave is launched in the direction perpendicular to the antenna, from the silicon side. A monitor is placed outside this region to isolate the scattered fields. A near- to far-field transform is then used to calculate the scattered field radiated in the direction perpendicular to the plane of the antenna.

Published work

- N. Yu, **R. Blanchard**, J. Fan, F. Capasso, T. Edamura, M. Yamanishi, H. Kan, "Small divergence edge-emitting semiconductor lasers with two-dimensional plasmonic collimators", Applied Physics Letters **93**, 181101 (2008).

- N. Yu, **R. Blanchard**, J. Fan, Q. J. Wang, C. Pflügl, L. Diehl, T. Edamura, M. Yamanishi, H. Kan, F. Capasso, "Quantum cascade lasers with integrated plasmonic antenna-array collimators", Optics Express **16**, 19447 (2008).

- N. Yu, **R. Blanchard**, J. Fan, Q. J. Wang, C. Pflügl, L. Diehl, T. Edamura, S. Furuta, M. Yamanishi, H. Kan, F. Capasso, "Plasmonics for laser beam shaping", IEEE Transactions on Nanotechnology **9**, 11 (2010).

- P. Genevet, J.-P. Tetienne, E. Gatzogiannis, **R. Blanchard**, M. A. Kats, M. O. Scully, F. Capasso, "Large enhancement of nonlinear Optical phenomena by plasmonic nanocavity gratings", Nano Letters **10**, 4880 (2010).

- J.-P. Tetienne, **R. Blanchard**, N. Yu, P. Genevet, M. A. Kats, J. A. Fan, T. Edamura, S. Furuta, M. Yamanishi, F. Capasso, "Dipolar modeling and experimental demonstration of multi-beam plasmonic collimators", New Journal of Physics **13**, 53057 (2011).

- M. A. Kats, D. Woolf, **R. Blanchard**, N. Yu, F. Capasso, "Spoof plasmon analogue of metal-insulator-metal waveguides", Optics Express **19**, 14860 (2011).

- P. Genevet, J.-P. Tetienne, **R. Blanchard**, M. A. Kats, J. P. B. Muller, M. O. Scully, F. Capasso, "Enhancement of optical processes in coupled plasmonic nanocavities", Applied Optics **50**, 56 (2011).

- **R. Blanchard**, S. V. Boriskina, P. Genevet, M. A. Kats, J.-P. Tetienne, N. Yu, M. O. Scully, L. Dal Negro, F. Capasso, "Multi-wavelength mid-infrared plasmonic antennas with single nanoscale focal point", Optics Express **19**, 22113 (2011).

- **R. Blanchard**, S. Menzel, C. Pflügl, L. Diehl, C. Wang, Y. Huang, J.-H. Ryou, R. D. Dupuis, L. Dal Negro, F. Capasso, "Gratings with an aperiodic basis: single-mode emission in multi-wavelength lasers", New Journal of Physics **13**, 113023 (2011).

- P. Genevet, N. Yu, F. Aieta, J. Lin, M. A. Kats, **R. Blanchard**, M. O. Scully, Z. Gaburro, F. Capasso, "Ultra-thin plasmonic optical vortex plate based on phase discontinuities", Applied Physics Letters **100**, 13101 (2012).

- **R. Blanchard**, C. Grezes, S. Menzel, C. Pflügl, L. Diehl, Y. Huang, J.-H. Ryou, R. D. Dupuis, F. Capasso, "Double-waveguide quantum cascade laser", Applied Physics Letters **100**, 33502 (2012).

- **R. Blanchard**, G. Aoust, P. Genevet, N. Yu, M. A. Kats, Z. Gaburro, F. Capasso, "Modeling nanoscale V-shaped antennas for the design of optical phased arrays", Physical Review B **85**, 155457 (2012).

- M. A. Kats, P. Genevet, G. Aoust, N. Yu, **R. Blanchard**, F. Aieta, Z. Gaburro, and F. Capasso, "Giant birefringence in optical antenna arrays with widely tailorable optical anisotropy", PNAS **109**, 12364 (2012).

- F. Aieta, P. Genevet, M. A. Kats, N. Yu, **R. Blanchard**, Z. Gaburro, F. Capasso, "Aberration-Free Ultrathin Flat Lenses and Axicons at Telecom Wavelengths Based on Plasmonic Metasurfaces", Nano Letters **12**, 4932 (2012).

- T. Mansuripur, S. Menzel, **R. Blanchard**, L. Diehl, C. Pflügl, Y. Huang, J.H. Ryou, R.D. Dupuis, M. Loncar, and F. Capasso, "Widely tunable mid-infrared quantum cascade lasers using sampled grating reflectors", Optics Express **20**, 23339 (2012).

- M. A. Kats, **R. Blanchard**, P. Genevet and F. Capasso, "Nanometre optical coatings based on strong interference effects in highly absorbing media", Nature Materials **12**, 20 (2012).

- M. A. Kats, D. Sharma, J. Lin, P. Genevet, **R. Blanchard**, Z. Yang, M. M. Qazilbash, D. N. Basov, S. Ramanathan, and F. Capasso, "Ultra-thin perfect absorber employing a tunable phase change material", Applied Physics Letters **101**, 221101 (2012).

- M. A. Kats, **R. Blanchard**, P. Genevet, Z. Yang, M. M. Qazilbash, D. N. Basov, S. Ramanathan, and F. Capasso, "Thermal tuning of mid-infrared plasmonic antenna arrays using a phase change material", Optics Letters **38**, 368 (2013).

- B. Gokden, T. S. Mansuripur, **R. Blanchard**, C. Wang, A. Goyal, A. Sanchez-Rubio, G. Turner and F. Capasso, "High-brightness tapered quantum cascade lasers", Applied Physics Letters **102**, 53503 (2013).

- N. Yu, P. Genevet, F. Aieta, M. A. Kats, **R. Blanchard**, G. Aoust, J.-P. Tetienne, Z. Gaburro, and F. Capasso, "Flat Optics: Controlling Wavefronts with Optical Antenna Metasurfaces", IEEE Journal of selected topics in quantum electronics, **19**, 4700423 (2013).

- P. Malara, **R. Blanchard**, T. S. Mansuripur, A. K. Wojcik, A. Belyanin, K. Fujita, T. Edamura, S. Furuta, M. Yamanishi, P. de Natale, and F. Capasso, "External ring-cavity quantum cascade lasers", Applied Physics Letters **102**, 141105 (2013).

- P. Genevet, J. Dellinger, **R. Blanchard**, A. She, M. Petit, B. Cluzel, M. A. Kats, F. de Fornel, and F. Capasso, "Generation of two-dimensional plasmonic bottle beams", Optics Express **21**, 10295 (2013).

- **R. Blanchard**, T. S. Mansuripur, B. Gokden, N. Yu, M. Kats, P. Genevet, K. Fujita, T. Edamura, M. Yamanishi, and F. Capasso, "High-power low-divergence tapered quantum cascade lasers with plasmonic collimators", Applied Physics Letters **102**, 191114 (2013).

- M. A. Kats, S. J. Byrnes, **R. Blanchard**, M. Kolle, P. Genevet, J. Aizenberg, and F. Capasso, "Enhancement of absorption and color contrast in ultra-thin highly absorbing optical coatings", Applied Physics Letters **103**, 101104 (2013).

- M. A. Kats, **R. Blanchard**, S. Zhang, P. Genevet, C. Ko, S. Ramanathan, and F. Capasso, "Vanadium Dioxide as a Natural Disordered Metamaterial: Perfect Thermal Emission and Large Broadband Negative Differential Thermal Emittance", Physical Review X **3**, 041004 (2013).

- M. Sidler, P. Rauter, **R. Blanchard**, P. Métivier, C. Wang, R. Dupuis, J. Faist and F. Capasso, "Mode switching in a multi-wavelength distributed feedback quantum cascade laser using an external micro-cavity ", Applied Physics Letters (2013 - submitted).

Book chapter

- N. Yu, M. A. Kats, P. Genevet, F. Aieta, **R. Blanchard**, G. Aoust, Z. Gaburro and F. Capasso, "Controlling light propagation with interfacial phase discontinuities", in *Active Plasmonics and Tuneable Plasmonic Metamaterials*, edited by A. V. Zayats and S. Maier (John Wiley & Sons, 2013).

Bibliography

[1] Jérôme Faist, Federico Capasso, Deborah L Sivco, Carlo Sirtori, Albert L Hutchinson, and Alfred Y Cho. Quantum Cascade Laser. *Science (New York, N.Y.)*, 264 (5158):553–556, April 1994.

[2] Jérôme Faist, Claire Gmachl, Federico Capasso, Carlo Sirtori, Deborah L. Sivco, James N. Baillargeon, and Alfred Y. Cho. Distributed feedback quantum cascade lasers. *Applied Physics Letters*, 70(20):2670, May 1997.

[3] Mattias Beck, Daniel Hofstetter, Thierry Aellen, Jérôme Faist, Ursula Oesterle, Marc Ilegems, Emilio Gini, and Hans Melchior. Continuous wave operation of a mid-infrared semiconductor laser at room temperature. *Science (New York, N.Y.)*, 295(5553):301–5, January 2002.

[4] Robert F. Curl, Federico Capasso, Claire Gmachl, Anatoliy A. Kosterev, Barry McManus, Rafa Lewicki, Michael Pusharsky, Gerard Wysocki, and Frank K. Tittel. Quantum cascade lasers in chemical physics. *Chemical Physics Letters*, 487 (1):1–18, 2010.

[5] Richard Maulini. *Broadly tunable mid-infrared quantum cascade lasers for spectroscopic applications*. PhD thesis, 2006.

[6] Jérôme Faist. *Quantum Cascade Lasers*. Oxford University Press, USA, 2013. ISBN 0198528248.

[7] R Blanchard, S Menzel, C Pflügl, L Diehl, C Wang, Y Huang, J-H Ryou, R D Dupuis, L Dal Negro, and F Capasso. Gratings with an aperiodic basis: single-mode emission in multi-wavelength lasers. *New Journal of Physics*, 13(11):113023, November 2011.

[8] Tobias S Mansuripur, Stefan Menzel, Romain Blanchard, Laurent Diehl, Christian Pflügl, Yong Huang, Jae-Hyun Ryou, Russell D Dupuis, Marko Loncar, and Federico Capasso. Widely tunable mid-infrared quantum cascade lasers using sampled grating reflectors. *Optics Express*, 20(21):23339–48, October 2012.

[9] Romain Blanchard, Cecile Grezes, Stefan Menzel, Christian Pflügl, Laurent Diehl, Yong Huang, Jae-Hyun Ryou, Russell D. Dupuis, and Federico Capasso. Double-waveguide quantum cascade laser. *Applied Physics Letters*, 100(3):033502, January 2012.

[10] N. Yu, R. Blanchard, J. Fan, C. Pfl̈ugl, L. Diehl, T. Edamura, S. Furuta, M. Yamanishi, H. Kan, and F. Capasso. Plasmonics for Laser Beam Shaping. *IEEE Transactions on Nanotechnology*, 9(1):11–29, January 2010.

[11] J-P Tetienne, R Blanchard, N Yu, P Genevet, M A Kats, J A Fan, T Edamura, S Furuta, M Yamanishi, and F Capasso. Dipolar modeling and experimental

demonstration of multi-beam plasmonic collimators. *New Journal of Physics*, 13 (5):053057, May 2011.

[12] Romain Blanchard, Tobias S. Mansuripur, Burc Gokden, Nanfang Yu, Mikhail Kats, Patrice Genevet, Kazuue Fujita, Tadataka Edamura, Masamichi Yamanishi, and Federico Capasso. High-power low-divergence tapered quantum cascade lasers with plasmonic collimators. *Applied Physics Letters*, 102(19):191114, May 2013.

[13] Romain Blanchard, Svetlana V Boriskina, Patrice Genevet, Mikhail A Kats, Jean-Philippe Tetienne, Nanfang Yu, Marlan O Scully, Luca Dal Negro, and Federico Capasso. Multi-wavelength mid-infrared plasmonic antennas with single nanoscale focal point. *Optics Express*, 19(22):22113–24, October 2011.

[14] Romain Blanchard, Guillaume Aoust, Patrice Genevet, Nanfang Yu, Mikhail A. Kats, Zeno Gaburro, and Federico Capasso. Modeling nanoscale V-shaped antennas for the design of optical phased arrays. *Physical Review B*, 85(15):155457, April 2012.

[15] F. Capasso, C. Gmachl, R. Paiella, A. Tredicucci, A.L. Hutchinson, D.L. Sivco, J.N. Baillargeon, A.Y. Cho, and H.C. Liu. New frontiers in quantum cascade lasers and applications. *IEEE Journal of Selected Topics in Quantum Electronics*, 6(6): 931–947, November 2000.

[16] A. Lyakh, R. Maulini, A. Tsekoun, R. Go, S. Von der Porten, C. Pflügl, L. Diehl, F. Capasso, and C. K. N. Patel. High-performance continuous-wave room temperature quantum cascade lasers with single-facet optical emission exceeding 2 W.

Proceedings of the National Academy of Sciences, 107(44):18799–18802, October 2010.

[17] Claire Gmachl, Deborah L Sivco, Raffaele Colombelli, Federico Capasso, and Alfred Y Cho. Ultra-broadband semiconductor laser. *Nature*, 415(6874):883–7, February 2002.

[18] Jérôme Faist, Mattias Beck, Thierry Aellen, and Emilio Gini. Quantum-cascade lasers based on a bound-to-continuum transition. *Applied Physics Letters*, 78(2): 147, January 2001.

[19] Kazuue Fujita, Shinich Furuta, Atsushi Sugiyama, Takahide Ochiai, Tadataka Edamura, Naota Akikusa, Masamichi Yamanishi, and Hirofumi Kan. High-Performance Quantum Cascade Lasers With Single Phonon-Continuum Depopulation Structures. *IEEE Journal of Quantum Electronics*, 46(5):683–688, May 2010.

[20] Yu Yao, Xiaojun Wang, Jen-Yu Fan, and Claire F. Gmachl. High performance continuum-to-continuum quantum cascade lasers with a broad gain bandwidth of over 400cm-1. *Applied Physics Letters*, 97(8):081115, August 2010.

[21] Peter Fuchs, Jochen Friedl, Sven Höfling, Johannes Koeth, Alfred Forchel, Lukas Worschech, and Martin Kamp. Single mode quantum cascade lasers with shallow-etched distributed Bragg reflector. *Optics Express*, 20(4):3890–7, February 2012.

[22] C. Gmachl, A. Straub, R. Colombelli, F. Capasso, D.L. Sivco, A.M. Sergent, and A.Y. Cho. Single-mode, tunable distributed-feedback and multiple-wavelength

quantum cascade lasers. *IEEE Journal of Quantum Electronics*, 38(6):569–581, June 2002.

[23] B.G. Lee, M.A. Belkin, C. Pflügl, L. Diehl, H.A. Zhang, R.M. Audet, J. MacArthur, D.P. Bour, S.W. Corzine, G.E. Hufler, and F. Capasso. DFB Quantum Cascade Laser Arrays. *IEEE Journal of Quantum Electronics*, 45(5): 554–565, May 2009.

[24] Benjamin G. Lee, Haifei A. Zhang, Christian Pflügl, Laurent Diehl, Mikhail A. Belkin, Milan Fischer, Andreas Wittmann, Jérôme Faist, and Federico Capasso. Broadband Distributed-Feedback Quantum Cascade Laser Array Operating From 8.0 to 9.8 um. *IEEE Photonics Technology Letters*, 21(13):914–916, July 2009.

[25] P. Rauter, S. Menzel, a. K. Goyal, B. Gokden, C. a. Wang, a. Sanchez, G. W. Turner, and F. Capasso. Master-oscillator power-amplifier quantum cascade laser array. *Applied Physics Letters*, 101(26):261117, 2012.

[26] Patrick Rauter, Stefan Menzel, Anish K Goyal, Christine A Wang, Antonio Sanchez, George Turner, and Federico Capasso. High-power arrays of quantum cascade laser master-oscillator power-amplifiers. *Optics Express*, 21(4):4518–30, February 2013.

[27] Benjamin G Lee, Jan Kansky, Anish K Goyal, Christian Pflügl, Laurent Diehl, Mikhail A Belkin, Antonio Sanchez, and Federico A Capasso. Beam combining of quantum cascade laser arrays. *Optics Express*, 17(18):16216–24, August 2009.

[28] Anish K Goyal, Melissa Spencer, Oleg Shatrovoy, Benjamin G Lee, Laurent Diehl, Christian Pflügl, Antonio Sanchez, and Federico Capasso. Dispersion-compensated wavelength beam combining of quantum-cascade-laser arrays. *Optics Express*, 19 (27):26725–32, December 2011.

[29] Andreas Hugi, Romain Terazzi, Yargo Bonetti, Andreas Wittmann, Milan Fischer, Mattias Beck, Jérôme Faist, and Emilio Gini. External cavity quantum cascade laser tunable from 7.6 to 11.4 μm. *Applied Physics Letters*, 95(6):061103, August 2009.

[30] V. Jayaraman, Z.-M. Chuang, and L.A. Coldren. Theory, design, and performance of extended tuning range semiconductor lasers with sampled gratings. *IEEE Journal of Quantum Electronics*, 29(6):1824–1834, June 1993.

[31] Markus W. Sigrist. *Air Monitoring by Spectroscopic Techniques*. John Wiley & Sons, 1994. ISBN 0471558753.

[32] Mikhail A. Belkin, Federico Capasso, Alexey Belyanin, Deborah L. Sivco, Alfred Y. Cho, Douglas C. Oakley, Christopher J. Vineis, and George W. Turner. Terahertz quantum-cascade-laser source based on intracavity difference-frequency generation. *Nature Photonics*, 1(5):288–292, May 2007.

[33] M. Sidler, P. Rauter, R. Blanchard, P. Metivier, C. Wang, R. Dupuis, J. Faist, and F. Capasso. Mode switching in a multi wavelength distributed feedback quantum cascade laser using an external micro-cavity. *Applied Physics Letters*, (submitted, 2013.

[34] Christopher S Colley, Jeremy C Hebden, David T Delpy, Alison D Cambrey, Robert A Brown, Evgeny A Zibik, Wing H Ng, Luke R Wilson, and John W Cockburn. Mid-infrared optical coherence tomography. *The Review of scientific instruments*, 78(12):123108, December 2007.

[35] Albert Schliesser, Nathalie Picqué, and Theodor W. Hänsch. Mid-infrared frequency combs. *Nature Photonics*, 6(7):440–449, June 2012.

[36] Ariel Gordon, Christine Wang, L. Diehl, F. Kärtner, A. Belyanin, D. Bour, S. Corzine, G. Höfler, H. Liu, H. Schneider, T. Maier, M. Troccoli, J. Faist, and Federico Capasso. Multimode regimes in quantum cascade lasers: From coherent instabilities to spatial hole burning. *Physical Review A*, 77(5):053804, May 2008.

[37] H. Kogelnik. Coupled-Wave Theory of Distributed Feedback Lasers. *Journal of Applied Physics*, 43(5):2327, May 1972.

[38] Neil W. Ashcroft and N. David Mermin. *Solid State Physics*. Holt, Rinehart and Winston, New York, 1976. ISBN 8131500527.

[39] S. Slivken, N. Bandyopadhyay, S. Tsao, S. Nida, Y. Bai, Q. Y. Lu, and M. Razeghi. Sampled grating, distributed feedback quantum cascade lasers with broad tunability and continuous operation at room temperature. *Applied Physics Letters*, 100 (26):261112, June 2012.

[40] K. Boylan, V. Weldon, D. McDonald, J. Hegarty, and J. O'Gorman. Sampled grating DBR laser as a spectroscopic source in multigas detection at 1.521.57 um. *IEE Proceedings - Optoelectronics*, 148(1):19–24, February 2001.

[41] Y. Tohmori, Y. Yoshikuni, H. Ishii, F. Kano, T. Tamamura, Y. Kondo, and M. Yamamoto. Broad-range wavelength-tunable superstructure grating (SSG) DBR lasers. *IEEE Journal of Quantum Electronics*, 29(6):1817–1823, June 1993.

[42] Manfred Schroeder. *Number Theory in Science and Communication: With Applications in Cryptography, Physics, Digital Information, Computing, and Self-Similarity*. Springer, 2009. ISBN 3540852972.

[43] I.A. Avrutsky, D.S. Ellis, A. Tager, H. Anis, and J.M. Xu. Design of widely tunable semiconductor lasers and the concept of binary superimposed gratings (BSG's). *IEEE Journal of Quantum Electronics*, 34(4):729–741, April 1998.

[44] Lukas Mahler, Alessandro Tredicucci, Fabio Beltram, Christoph Walther, Jérôme Faist, Harvey E. Beere, David A. Ritchie, and Diederik S. Wiersma. Quasi-periodic distributed feedback laser. *Nature Photonics*, 4(3):165–169, January 2010.

[45] Enrique Macia Barber. *Aperiodic Structures in Condensed Matter: Fundamentals and Applications (Condensed Matter Physics)*. Taylor & Francis, 2008. ISBN 142006827X.

[46] Daniel Hofstetter, Jerome Faist, Mattias Beck, and Ursula Oesterle. Surface-emitting 10.1 μm quantum-cascade distributed feedback lasers. *Applied Physics Letters*, 75(24):3769, December 1999.

[47] C. Pflügl, M. Austerer, W. Schrenk, S. Golka, G. Strasser, R. P. Green, L. R. Wilson, J. W. Cockburn, A. B. Krysa, and J. S. Roberts. Single-mode surface-emitting quantum-cascade lasers. *Applied Physics Letters*, 86(21):211102, May

2005.

[48] L. Dal Negro and S.V. Boriskina. Deterministic aperiodic nanostructures for photonics and plasmonics applications. *Laser & Photonics Reviews*, 6(2):178–218, April 2012.

[49] Mihnea Dulea, Magnus Johansson, and Rolf Riklund. Localization of electrons and electromagnetic waves in a deterministic aperiodic system. *Physical Review B*, 45(1):105–114, January 1992.

[50] Lars Kroon, Erik Lennholm, and Rolf Riklund. Localization-delocalization in aperiodic systems. *Physical Review B*, 66(9):094204, September 2002.

[51] Ashwin Gopinath, Svetlana V Boriskina, Ning-Ning Feng, Björn M Reinhard, and Luca Dal Negro. Photonic-plasmonic scattering resonances in deterministic aperiodic structures. *Nano letters*, 8(8):2423–31, August 2008.

[52] Jin-Kyu Yang, Svetlana V. Boriskina, Heeso Noh, Michael J. Rooks, Glenn S. Solomon, Luca Dal Negro, and Hui Cao. Demonstration of laser action in a pseudorandom medium. *Applied Physics Letters*, 97(22):223101, November 2010.

[53] Yong Huang, Jae-Hyun Ryou, Russell D. Dupuis, Christian Pflügl, Federico Capasso, Kewei Sun, Alec M. Fischer, and Fernando A. Ponce. Optimization of growth conditions for InGaAs/InAlAs/InP quantum cascade lasers by metalorganic chemical vapor deposition. *Journal of Crystal Growth*, 316(1):75–80, 2011.

[54] Andreas Wittmann, Tobias Gresch, Emilio Gini, Lubos Hvozdara, Nicolas Hoyler, Marcella Giovannini, and Jérôme Faist. High-Performance Bound-to-Continuum

Quantum-Cascade Lasers for Broad-Gain Applications. *IEEE Journal of Quantum Electronics*, 44(1):36–40, January 2008.

[55] Geert Morthier and Patrick Vankwikelberge. *Handbook of distributed feedback laser diodes*. Artech House, 1997. ISBN 0890066078.

[56] R. P. Green, L. R. Wilson, E. A. Zibik, D. G. Revin, J. W. Cockburn, C. Pflügl, W. Schrenk, G. Strasser, A. B. Krysa, J. S. Roberts, C. M. Tey, and A. G. Cullis. High-performance distributed feedback quantum cascade lasers grown by metalorganic vapor phase epitaxy. *Applied Physics Letters*, 85(23):5529, December 2004.

[57] K. J. Ebeling and L. A. Coldren. Analysis of multielement semiconductor lasers. *Journal of Applied Physics*, 54(6):2962, June 1983.

[58] A. Bismuto, T. Gresch, A. Bachle, and Jérôme Faist. Large cavity quantum cascade lasers with InP interstacks. *Applied Physics Letters*, 93(23):231104, December 2008.

[59] Junqi Liu, Fengqi Liu, Lu Li, Lijun Wang, and Zhanguo Wang. A mini-staged multi-stacked quantum cascade laser for improved optical and thermal performance. *Semiconductor Science and Technology*, 24(7):075023, July 2009.

[60] Markus Geiser, Christian Pflügl, Alexey Belyanin, Qi Jie Wang, Nanfang Yu, Tadanaka Edamura, Masamichi Yamanishi, Hirofumi Kan, Milan Fischer, Andreas Wittmann, Jérôme Faist, and Federico Capasso. Gain competition in dual wavelength quantum cascade lasers. *Optics Express*, 18(10):9900–8, May 2010.

[61] A. E. Siegman. *Lasers*. University Science Books, 1986. ISBN 0935702113.

[62] Amnon Yariv and Pochi Yeh. *Photonics: Optical Electronics in Modern Communications*. Oxford University Press, Incorporated, 2007. ISBN 0195179463.

[63] Nanfang Yu, Jonathan Fan, Qi Jie Wang, Christian Pflügl, Laurent Diehl, Tadataka Edamura, Masamichi Yamanishi, Hirofumi Kan, and Federico Capasso. Small-divergence semiconductor lasers by plasmonic collimation. *Nature Photonics*, 2(9):564–570, July 2008.

[64] Nanfang Yu, Romain Blanchard, Jonathan Fan, Qi Jie Wang, Christian Pflügl, Laurent Diehl, Tadataka Edamura, Masamichi Yamanishi, Hirofumi Kan, and Federico Capasso. Quantum cascade lasers with integrated plasmonic antenna-array collimators. *Optics Express*, 16(24):19447, November 2008.

[65] Nanfang Yu, Romain Blanchard, Jonathan Fan, Federico Capasso, Tadataka Edamura, Masamichi Yamanishi, and Hirofumi Kan. Small divergence edge-emitting semiconductor lasers with two-dimensional plasmonic collimators. *Applied Physics Letters*, 93(18):181101, November 2008.

[66] Stefan Alexander Maier. *Plasmonics: Fundamentals and Applications*. Springer, 2007. ISBN 0387331506.

[67] William L. Barnes, Alain Dereux, and Thomas W. Ebbesen. Surface plasmon subwavelength optics. *Nature*, 424(6950):824–830, August 2003.

[68] Jon A Schuller, Edward S Barnard, Wenshan Cai, Young Chul Jun, Justin S White, and Mark L Brongersma. Plasmonics for extreme light concentration and manipulation. *Nature materials*, 9(3):193–204, March 2010.

[69] L. Martín-Moreno, F. García-Vidal, H. Lezec, A. Degiron, and T. Ebbesen. Theory of Highly Directional Emission from a Single Subwavelength Aperture Surrounded by Surface Corrugations. *Physical Review Letters*, 90(16):167401, April 2003.

[70] Liang-Bin Yu, Ding-Zheng Lin, Yi-Chun Chen, You-Chia Chang, Kuo-Tung Huang, Jiunn-Woei Liaw, Jyi-Tyan Yeh, Jonq-Min Liu, Chau-Shioung Yeh, and Chih-Kung Lee. Physical origin of directional beaming emitted from a subwavelength slit. *Physical Review B*, 71(4):041405, January 2005.

[71] F. J. Garca-Vidal, L. Martn-Moreno, H. J. Lezec, and T. W. Ebbesen. Focusing light with a single subwavelength aperture flanked by surface corrugations. *Applied Physics Letters*, 83(22):4500, December 2003.

[72] Seyoon Kim, Hwi Kim, Yongjun Lim, and Byoungho Lee. Off-axis directional beaming of optical field diffracted by a single subwavelength metal slit with asymmetric dielectric surface gratings. *Applied Physics Letters*, 90(5):051113, February 2007.

[73] H J Lezec, A Degiron, E Devaux, R A Linke, L Martin-Moreno, F J Garcia-Vidal, and T W Ebbesen. Beaming light from a subwavelength aperture. *Science (New York, N.Y.)*, 297(5582):820–2, August 2002.

[74] Tsutomu Ishi, Junichi Fujikata, Kikuo Makita, Toshio Baba, and Keishi Ohashi. Si Nano-Photodiode with a Surface Plasmon Antenna. *Japanese Journal of Applied Physics*, 44(No. 12):L364–L366, March 2005.

[75] Zhaowei Liu, Jennifer M Steele, Werayut Srituravanich, Yuri Pikus, Cheng Sun, and Xiang Zhang. Focusing surface plasmons with a plasmonic lens. *Nano letters*, 5(9):1726–9, September 2005.

[76] Byoungho Lee, Seyoon Kim, Hwi Kim, and Yongjun Lim. The use of plasmonics in light beaming and focusing. *Progress in Quantum Electronics*, 34(2):47–87, 2010.

[77] Nanfang Yu, Qi Jie Wang, Mikhail A Kats, Jonathan A Fan, Suraj P Khanna, Lianhe Li, A Giles Davies, Edmund H Linfield, and Federico Capasso. Designer spoof surface plasmon structures collimate terahertz laser beams. *Nature materials*, 9(9):730–5, September 2010.

[78] D. Heitmann and C. Ortiz. Calculation and experimental verification of two-dimensional focusing grating couplers. *IEEE Journal of Quantum Electronics*, 17 (7):1257–1263, July 1981.

[79] W. Schrenk, N. Finger, S. Gianordoli, L. Hvozdara, G. Strasser, and E. Gornik. Surface-emitting distributed feedback quantum-cascade lasers. *Applied Physics Letters*, 77(14):2086, October 2000.

[80] E. Mujagic, L. K. Hoffmann, S. Schartner, M. Nobile, W. Schrenk, M. P. Semtsiv, M. Wienold, W. T. Masselink, and G. Strasser. Low divergence single-mode surface

emitting quantum cascade ring lasers. *Applied Physics Letters*, 93(16):161101, October 2008.

[81] Lukas Mahler, Alessandro Tredicucci, Fabio Beltram, Christoph Walther, Jérôme Faist, Bernd Witzigmann, Harvey E. Beere, and David A. Ritchie. Vertically emitting microdisk lasers. *Nature Photonics*, 3(1):46–49, November 2008.

[82] Nanfang Yu, Mikhail Kats, Christian Pflügl, Markus Geiser, Qi Jie Wang, Mikhail A. Belkin, Federico Capasso, Milan Fischer, Andreas Wittmann, Jérôme Faist, Tadataka Edamura, Shinichi Furuta, Masamichi Yamanishi, and Hirofumi Kan. Multi-beam multi-wavelength semiconductor lasers. *Applied Physics Letters*, 95(16):161108, October 2009.

[83] P. Lalanne, J.P. Hugonin, H.T. Liu, and B. Wang. A microscopic view of the electromagnetic properties of sub-λ metallic surfaces. *Surface Science Reports*, 64 (10):453–469, 2009.

[84] R. Martini, C. Bethea, F. Capasso, C. Gmachl, R. Paiella, E.A. Whittaker, H.Y. Hwang, D.L. Sivco, J.N. Baillargeon, and A.Y. Cho. Free-space optical transmission of multimedia satellite data streams using mid-infrared quantum cascade lasers. *Electronics Letters*, 38(4):181, 2002.

[85] Gen-ichi Hatakoshi. Analysis of Beam Quality Factor for Semiconductor Lasers. *Optical Review*, 10(4):307–314, July 2003.

[86] D. Bisping, D. Pucicki, M. Fischer, J. Koeth, C. Zimmermann, P. Weinmann, S. Hofling, M. Kamp, and A. Forchel. GaInNAs-Based High-Power and Tapered

Laser Diodes for Pumping Applications. *IEEE Journal of Selected Topics in Quantum Electronics*, 15(3):968–972, 2009.

[87] Y. Bai, S. Slivken, Q. Y. Lu, N. Bandyopadhyay, and M. Razeghi. Angled cavity broad area quantum cascade lasers. *Applied Physics Letters*, 101(8):081106, August 2012.

[88] J. N. Walpole, E. S. Kintzer, S. R. Chinn, C. A. Wang, and L. J. Missaggia. High-power strained-layer InGaAs/AlGaAs tapered traveling wave amplifier. *Applied Physics Letters*, 61(7):740, August 1992.

[89] Mariano Troccoli, Claire Gmachl, Federico Capasso, Deborah L. Sivco, and Alfred Y. Cho. Mid-infrared quantum cascade laser amplifier for high power single-mode emission and improved beam quality. *Applied Physics Letters*, 80(22):4103, June 2002.

[90] Stefan Menzel, Laurent Diehl, Christian Pflügl, Anish Goyal, Christine Wang, Antonio Sanchez, George Turner, and Federico Capasso. Quantum cascade laser master-oscillator power-amplifier with 1.5 W output power at 300 K. *Optics Express*, 19(17):16229–35, August 2011.

[91] Mikhail A. Belkin, Federico Capasso, Feng Xie, Alexey Belyanin, Milan Fischer, Andreas Wittmann, and Jérôme Faist. Room temperature terahertz quantum cascade laser source based on intracavity difference-frequency generation. *Applied Physics Letters*, 92(20):201101, May 2008.

[92] Q. Y. Lu, N. Bandyopadhyay, S. Slivken, Y. Bai, and M. Razeghi. Room temperature single-mode terahertz sources based on intracavity difference-frequency generation in quantum cascade lasers. *Applied Physics Letters*, 99(13):131106, September 2011.

[93] Lars Nahle, Julia Semmel, Wolfgang Kaiser, Sven Hofling, and Alfred Forchel. Tapered quantum cascade lasers. *Applied Physics Letters*, 91(18):181122, November 2007.

[94] Xue Huang, Yenting Chiu, William O Charles, and Claire Gmachl. Ridge-width dependence of the threshold of long wavelength Quantum Cascade lasers with sloped and vertical sidewalls. *Optics Express*, 20(3):2539–47, January 2012.

[95] Burc Gokden, Tobias S. Mansuripur, Romain Blanchard, Christine Wang, Anish Goyal, Antonio Sanchez-Rubio, George Turner, and Federico Capasso. High-brightness tapered quantum cascade lasers. *Applied Physics Letters*, 102(5): 053503, February 2013.

[96] Richard Maulini, Arkadiy Lyakh, Alexei Tsekoun, Rowel Go, Christian Pflügl, Laurent Diehl, Federico Capasso, and C. Kumar N. Patel. High power thermoelectrically cooled and uncooled quantum cascade lasers with optimized reflectivity facet coatings. *Applied Physics Letters*, 95(15):151112, October 2009.

[97] Y. Bai, N. Bandyopadhyay, S. Tsao, S. Slivken, and M. Razeghi. Room temperature quantum cascade lasers with 27% wall plug efficiency. *Applied Physics Letters*, 98(18):181102, May 2011.

[98] Edward D. Palik. *Handbook of Optical Constants of Solids*. Academic Press, 1991. ISBN 0125444222.

[99] J. N. Walpole. Semiconductor amplifiers and lasers with tapered gain regions. *Optical and Quantum Electronics*, 28(6):623–645, June 1996.

[100] A J Huber, A Ziegler, T Köck, and R Hillenbrand. Infrared nanoscopy of strained semiconductors. *Nature nanotechnology*, 4(3):153–7, March 2009.

[101] J M Stiegler, A J Huber, S L Diedenhofen, J Gómez Rivas, R E Algra, E P A M Bakkers, and R Hillenbrand. Nanoscale free-carrier profiling of individual semiconductor nanowires by infrared near-field nanoscopy. *Nano letters*, 10(4): 1387–92, April 2010.

[102] F Huth, M Schnell, J Wittborn, N Ocelic, and R Hillenbrand. Infrared-spectroscopic nanoimaging with a thermal source. *Nature materials*, 10(5):352–6, May 2011.

[103] S. Kawata and Y. Inouye. Scanning probe optical microscopy using a metallic probe tip. *Ultramicroscopy*, 57(2):313–317, 1995.

[104] B. Knoll and F. Keilmann. Near-field probing of vibrational absorption for chemical microscopy. 399(6732):134–137, May 1999.

[105] F Zenhausern, Y Martin, and H K Wickramasinghe. Scanning interferometric apertureless microscopy: optical imaging at 10 angstrom resolution. *Science (New York, N.Y.)*, 269(5227):1083–5, August 1995.

[106] Davis Richards and Anatoly Zayats. *Nano-Optics and Near-Field Optical Microscopy*. Artech House, 2008. ISBN 159693283X.

[107] Nenad Ocelic, Andreas Huber, and Rainer Hillenbrand. Pseudoheterodyne detection for background-free near-field spectroscopy. *Applied Physics Letters*, 89(10): 101124, September 2006.

[108] M. Schnell, P. Alonso-González, L. Arzubiaga, F. Casanova, L. E. Hueso, A. Chuvilin, and R. Hillenbrand. Nanofocusing of mid-infrared energy with tapered transmission lines. *Nature Photonics*, 5(5):283–287, April 2011.

[109] Francesco De Angelis, Gobind Das, Patrizio Candeloro, Maddalena Patrini, Matteo Galli, Alpan Bek, Marco Lazzarino, Ivan Maksymov, Carlo Liberale, Lucio Claudio Andreani, and Enzo Di Fabrizio. Nanoscale chemical mapping using three-dimensional adiabatic compression of surface plasmon polaritons. *Nature nanotechnology*, 5(1):67–72, January 2010.

[110] Svetlana V. Boriskina and Luca Dal Negro. Multiple-wavelength plasmonic nanoantennas. *Optics Letters*, 35(4):538, February 2010.

[111] D.T Schaafsma, R Mossadegh, J.S Sanghera, I.D Aggarwal, J.M Gilligan, N.H Tolk, M Luce, R Generosi, P Perfetti, A Cricenti, and G Margaritondo. Singlemode chalcogenide fiber infrared SNOM probes. *Ultramicroscopy*, 77(1):77–81, 1999.

[112] Shengli Zou and George C. Schatz. Silver nanoparticle array structures that produce giant enhancements in electromagnetic fields. *Chemical Physics Letters*, 403 (1):62–67, 2005.

[113] G. Vecchi, V. Giannini, and J. Gómez Rivas. Shaping the Fluorescent Emission by Lattice Resonances in Plasmonic Crystals of Nanoantennas. *Physical Review Letters*, 102(14):146807, April 2009.

[114] Yizhuo Chu, Ethan Schonbrun, Tian Yang, and Kenneth B. Crozier. Experimental observation of narrow surface plasmon resonances in gold nanoparticle arrays. *Applied Physics Letters*, 93(18):181108, November 2008.

[115] Ashwin Gopinath, Svetlana V. Boriskina, Björn M. Reinhard, and Luca Dal Negro. Deterministic aperiodic arrays of metal nanoparticles for surface-enhanced Raman scattering (SERS). *Optics Express*, 17(5):3741, February 2009.

[116] Ronen Adato, Ahmet A Yanik, Jason J Amsden, David L Kaplan, Fiorenzo G Omenetto, Mi K Hong, Shyamsunder Erramilli, and Hatice Altug. Ultra-sensitive vibrational spectroscopy of protein monolayers with plasmonic nanoantenna arrays. *Proceedings of the National Academy of Sciences of the United States of America*, 106(46):19227–32, November 2009.

[117] Katrin Kneipp, Martin Moskovits, and Harald Kneipp. *Surface-Enhanced Raman Scattering: Physics and Applications*. Springer, 2006. ISBN 3540335676.

[118] K. T. Carron, W. Fluhr, M. Meier, A. Wokaun, and H. W. Lehmann. Resonances of two-dimensional particle gratings in surface-enhanced Raman scattering. *Journal of the Optical Society of America B*, 3(3):430, March 1986.

[119] V.A. Markel. Coupled-dipole Approach to Scattering of Light from a One-dimensional Periodic Dipole Structure. *Journal of Modern Optics*, 40(11):2281–2291, November 1993.

[120] Shengli Zou, Nicolas Janel, and George C. Schatz. Silver nanoparticle array structures that produce remarkably narrow plasmon lineshapes. *The Journal of Chemical Physics*, 120(23):10871, June 2004.

[121] F. J. García de Abajo. Colloquium: Light scattering by particle and hole arrays. *Reviews of Modern Physics*, 79(4):1267–1290, October 2007.

[122] Baptiste Auguié and William Barnes. Collective Resonances in Gold Nanoparticle Arrays. *Physical Review Letters*, 101(14):143902, September 2008.

[123] Patrice Genevet, Jean-Philippe Tetienne, Evangelos Gatzogiannis, Romain Blanchard, Mikhail A Kats, Marlan O Scully, and Federico Capasso. Large Enhancement of Nonlinear Optical Phenomena by Plasmonic Nanocavity Gratings. *Nano letters*, 10(12):4880–4883, November 2010.

[124] Allen Taflove and Susan C. Hagness. *Computational Electrodynamics: The Finite-Difference Time-Domain Method*. Artech House, Incorporated, 2005. ISBN 1580538320.

[125] Benjamin M. Ross and Luke P. Lee. Comparison of near- and far-field measures for plasmon resonance of metallic nanoparticles. *Optics Letters*, 34(7):896, March 2009.

[126] M. Schnell, A. García-Etxarri, A. J. Huber, K. Crozier, J. Aizpurua, and R. Hillenbrand. Controlling the near-field oscillations of loaded plasmonic nanoantennas. *Nature Photonics*, 3(5):287–291, April 2009.

[127] Nanfang Yu, Ertugrul Cubukcu, Laurent Diehl, Mikhail A. Belkin, Kenneth B. Crozier, Federico Capasso, David Bour, Scott Corzine, and Gloria Hofler. Plasmonic quantum cascade laser antenna. *Applied Physics Letters*, 91(17):173113, October 2007.

[128] R. HillenbRand, B. Knoll, and F. Keilmann. Pure optical contrast in scattering-type scanning near-field microscopy. *Journal of Microscopy*, 202(1):77–83, April 2001.

[129] Bernhard Knoll and Fritz Keilmann. Enhanced dielectric contrast in scattering-type scanning near-field optical microscopy. *Optics Communications*, 182(4):321–328, 2000.

[130] R. Esteban, R. Vogelgesang, J. Dorfmuller, A. Dmitriev, C. Rockstuhl, C. Etrich, and K. Kern. Direct Near-Field Optical Imaging of Higher Order Plasmonic Resonances. *Nano Letters*, 8(10):3155–3159, October 2008.

[131] Martin Schnell, Aitzol Garcia-Etxarri, Andreas J. Huber, Kenneth B. Crozier, Andrei Borisov, Javier Aizpurua, and Rainer Hillenbrand. Amplitude- and Phase-Resolved Near-Field Mapping of Infrared Antenna Modes by Transmission-Mode Scattering-Type Near-Field Microscopy . *The Journal of Physical Chemistry C*, 114(16):7341–7345, April 2010.

[132] N. Yu, P. Genevet, M. A. Kats, F. Aieta, J.-P. Tetienne, F. Capasso, and Z. Gaburro. Light Propagation with Phase Discontinuities: Generalized Laws of Reflection and Refraction. *Science*, 334(6054):333–337, September 2011.

[133] Patrice Genevet, Nanfang Yu, Francesco Aieta, Jiao Lin, Mikhail A. Kats, Romain Blanchard, Marlan O. Scully, Zeno Gaburro, and Federico Capasso. Ultra-thin plasmonic optical vortex plate based on phase discontinuities. *Applied Physics Letters*, 100(1):013101, January 2012.

[134] Yang Zhao and Andrea Alù. Manipulating light polarization with ultrathin plasmonic metasurfaces. *Physical Review B*, 84(20):205428, November 2011.

[135] Ronold W. P. King. *The Theory of Linear Antennas... Ronold W. P. King,...* Mass., Harvard University Press, 1956.

[136] Sophocles J. Orfanidis. *Electromagnetic Waves and Antennas*. URL `http://www.ece.rutgers.edu/~orfanidi/ewa/`.

[137] Constantine A. Balanis. *Antenna Theory: Analysis and Design*. John Wiley & Sons, 2005. ISBN 1118585739.

[138] Warren L. Stutzman and Gary A. Thiele. *Antenna theory and design*. J. Wiley, 2012. ISBN 0471025909.

[139] R. Harrington. Origin and development of the method of moments for field computation. *IEEE Antennas and Propagation Magazine*, 32(3):31–35, June 1990.

[140] R. F. Harrington. *Field Computation by Moment Methods*. Macmillan, New York, 1968.

[141] J. J H Wang. Generalised moment methods in electromagnetics, 1990. ISSN 0950-107X.

[142] H. C. Pocklington. Electrical Oscillations in Wires. *Cambridge Phil. Soc. Proc.*, 9:324, 1897.

[143] Nader Engheta, Alessandro Salandrino, and Andrea Alù. Circuit Elements at Optical Frequencies: Nanoinductors, Nanocapacitors, and Nanoresistors. *Physical Review Letters*, 95(9):095504, August 2005.

[144] Andrea Alù and Nader Engheta. Tuning the scattering response of optical nanoantennas with nanocircuit loads. *Nature Photonics*, 2(5):307–310, April 2008.

[145] M. Staffaroni, J. Conway, S. Vedantam, J. Tang, and E. Yablonovitch. Circuit analysis in metal-optics. *Photonics and Nanostructures - Fundamentals and Applications*, 10(1):166–176, 2012.

[146] Hisamatsu Nakano. A numerical approach to line antennas printed on dielectric materials. *Computer Physics Communications*, 68(1):441–450, 1991.

[147] I. Rana and N. Alexopoulos. Current distribution and input impedance of printed dipoles. *IEEE Transactions on Antennas and Propagation*, 29(1):99–105, January 1981.

[148] N. Engheta, C. H. Papas, and C. Elachi. Radiation patterns of interfacial dipole antennas. *Radio Science*, 17(6):1557–1566, November 1982.

[149] Lukas Novotny and Niek van Hulst. Antennas for light. *Nature Photonics*, 5(2): 83–90, February 2011.

[150] John David Jackson. *Classical Electrodynamics Third Edition*. Wiley, 1998. ISBN 047130932X.

[151] J.H. Richmond. Digital computer solutions of the rigorous equations for scattering problems. *Proceedings of the IEEE*, 53(8):796–804, 1965.

[152] D.H. Werner, P.L. Werner, and J.K. Breakall. Some computational aspects of Pocklington's electric field integral equation for thin wires. *IEEE Transactions on Antennas and Propagation*, 42(4):561–563, April 1994.